POLITECNICO DI TORINO

Corso di Laurea in Ingegneria Elettronica

Tesi di Laurea Magistrale

Definition of compact models for the simulation of spin qubits in semiconductor quantum dots

Politecnico di Torino

Relatori
Prof. Mariagrazia Graziano
Prof. Maurizio Zamboni
Prof. Giovanna Turvani

Candidato
Davide Costa

April 2022

To my beloved parents, Susanna and Massimo, and to the memory of my dearest grandparents, Maria Luisa, Maria, Giovanni and Raffaele.

Summary

The rise in interest concealing quantum computing (QC) and the constant improvements in the quantum information field have led the research towards finding better ways of physically implementing a quantum processor. The most promising idea from the integration point of view is to realize qubits, the building blocks of quantum information, in semiconductors, looking forward to a possible future combination of these structures with the classical CMOS architectures. Therefore, being integration the ultimate goal, the choice between semiconductors falls on silicon, for which the technological processes have been studied for decades and are now very advanced; for this reason, the prospect of employing the spin of an electron in a silicon quantum dot as a qubit might be ideal.

The use of electron spin as qubit has been theorized by Daniel Loss and David DiVincenzo in 1998 [1], but it has only recently begun to spread as suitable option for quantum computing implementation. Although the feasibility of qubits through holes spin [2], donors spin [3] and point defects spin [4] in different semiconductors, such as germanium [5], gallium arsenide [6] and silicon carbide [7], has been demonstrated too, this thesis work will be focused on the use of the spin of electrons trapped in silicon gate-defined quantum dots.

This thesis tries to fulfil the need for a compact model that efficiently describes an electron spin qubits system, looking for a compromise between high accuracy in the description of noise sources and computational complexity. This would help quantum circuit designers and algorithms developers to estimate the performance of a circuit on a quantum computer. However, a canonical simulation of a quantum structure requires the solution of a complex system of differential equations. Quantum systems are usually analyzed through the Schrödinger equation, which, unfortunately, can only describe pure quantum states. Incoherent processes, such as relaxation and decoherence, are taken into account by the Lindblad master equation, which deals with density matrices. Anyway, the solution of the latter proves to be very long and computationally expensive and thus it is not realistically employable in a quantum simulator. This encourages the research towards a compact model granting a good simulating accuracy with a low computational cost.

Indeed, after a brief introduction of the fundamental concepts regarding solid-state quantum computing, the first chapter introduces the final objective of this work: developing a compact Matlab model able to describe, given the structure, the main features of the device, such as single-qubit manipulation and two-qubit gates implementation, taking into account the most relevant quantum noise factors. The goal is to obtain a fast but reliable way to realistically simulate a quantum device, in order to create a very useful tool for QC device engineering, giving the opportunity to evaluate the effects of physical characteristics on the execution of practical quantum circuits and algorithms.

The quantum confinement effect is studied in the second chapter, where the fundamental properties of semiconductor heterostructures are introduced. This serves to the purpose of explaining the physical concepts used in the realization of the quantum device. The silicon Double Quantum Dot (DQD) structure is indeed presented and defined at the end of the chapter.

The third chapter is devoted to an in-depth description of the DQD device, with a particular focus on the various possibilities of qubit encoding, such as spin-1/2, singlet-triplet and charge qubits, discussing their characteristics and listing pros and cons of each implementation. Having addressed the theoretical features of semiconductor qubits, the focus shifts on a particular type of structure, the SiMOS gate-defined DQD (Figure 1 and Figure 2). The device read-out and initialization methods are explored, as well as device control procedures, in order to familiarize with the technology relevant parameters.

The mathematical tools needed to understand the theory behind the manipulation of a single qubit in this type of structure are analyzed in the fourth chapter. In particular, a time-independent expression for the single-qubit spin Hamiltonian is derived for the purpose of compact modelling. Finally, a first implementation of the model is developed and tested through a Rabi flopping experiment.

The fifth chapter extends the theory elaborated in the previous chapter to the two-qubit case. The chapter describes the theoretical derivation of the DQD spin Hamiltonian through the Hubbard model and the Schrieffer-Wolff (SW) transformation, with particular attention on the approximations used to derive a time-independent matrix. The native gate duality is then explored, focusing on how to implement the two different gates. A second version of the compact model is developed and validated comparing its results with those obtained with the Quantum Toolbox in Python (QuTiP), a numerical solver of the Schrödinger and Lindblad equations, which permit to study the time evolution of quantum systems.

The sixth chapter is devoted to the analysis of the noise algorithm implemented in the compact model to take into account relaxation and decoherence effects. The fidelity of the noisy model is computed on QuTiP through the simulation of a sequence of $R_X(\frac{\pi}{2})$ gates on each qubit varying the duration of the gate. The MATLAB model and the QuTiP results are finally compared when relevant quantum circuits and algorithms are simulated.

The last chapter comprises the conclusions of this thesis work, giving a general look to the results obtained and to the advantages and disadvantages of the developed compact model. Furthermore, several possible ideas for future enhancements of the compact model are presented.

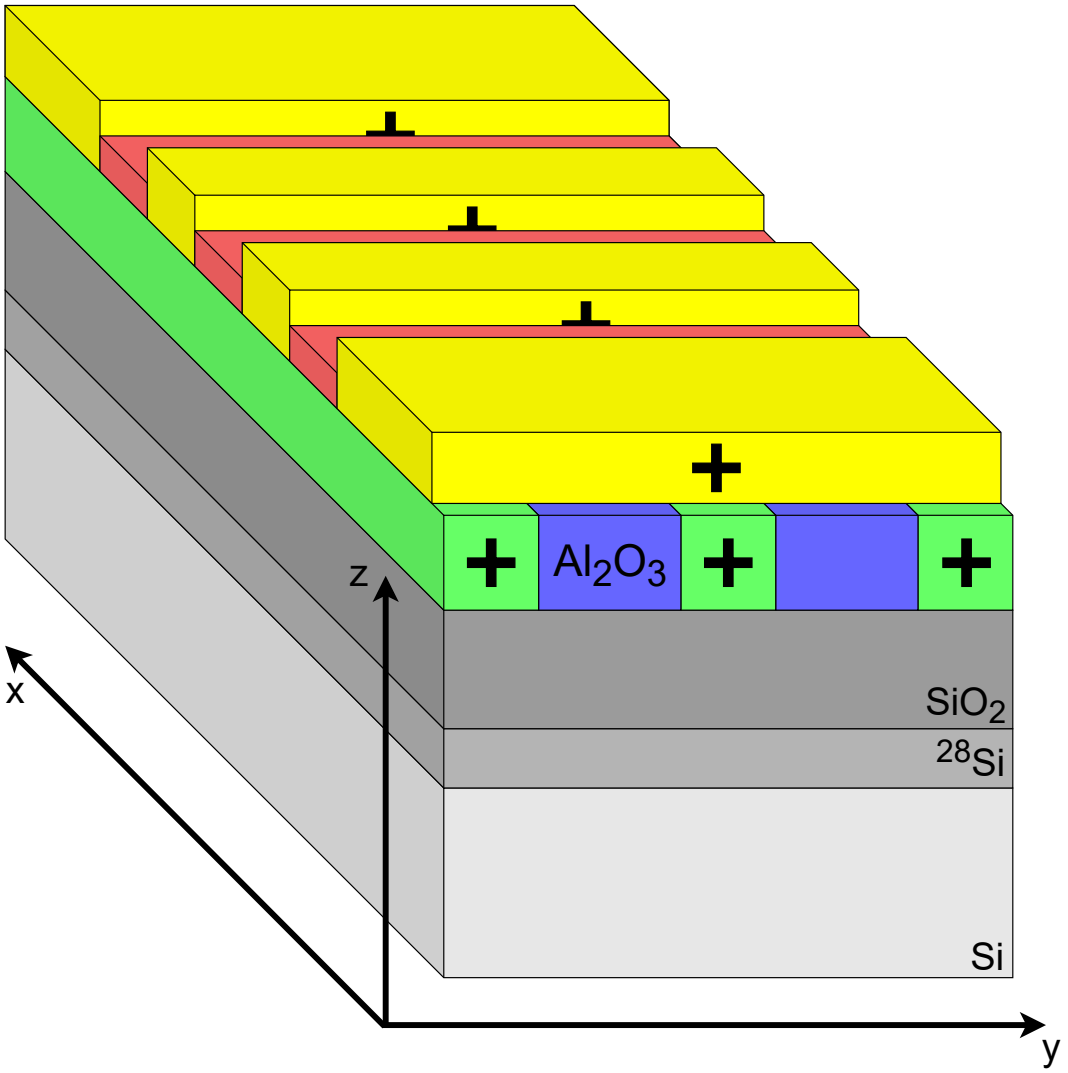

Figure 1: 3D view of the SiMOS DQD structure.

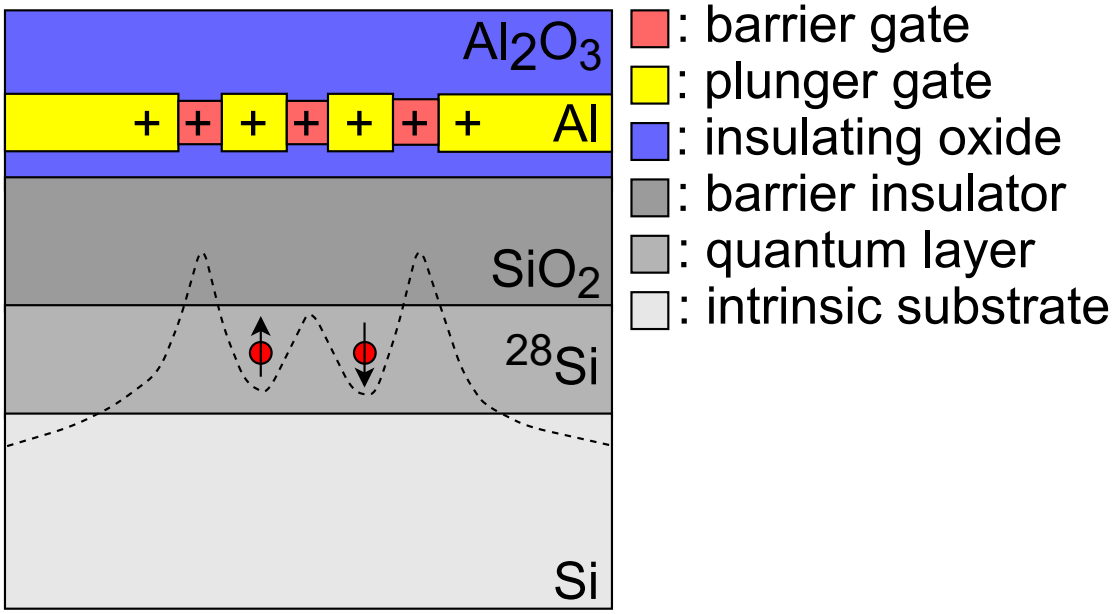

Figure 2: QDs created by electric fields from the gates.

Contents

Part I

General concepts introduction

Chapter 1

Thesis work outline

The purpose of the first chapter is to give an introduction on semiconductor quantum computing technology, explaining its strengths and the possible implementations. The reasons for the realization of a compact model able to simulate semiconductor quantum devices are then analyzed, with particular attention on the advantages offered by a fast quantum simulation.

1.1 Semiconductor quantum computation

1.1.1 Technology advantages

In the past decade, semiconductors have become a more and more prominent option for the realization of quantum computing devices. The research toward this type of implementation has grown significantly, since semiconductors might be the key to innovating progresses in quantum electronics. In fact, they are uniquely positioned to exploit the technology already existing for classical electronic devices, as share practically the same technological process steps with them. Therefore, semiconductor quantum computing has a huge potential for its massive scaling and miniaturization.
Another advantage of semiconductors is the possibility of an electrical device control. Indeed, semiconductor quantum devices can be manipulated with electric and magnetic fields generated through the use of metal gates and integrated micromagnets. Some advanced qubit encodings, such as the *exchange-only* qubit in quantum dots (QDs) [8], even remove the need of the micromagnets and allow a pure electrical control of the quantum structure, which is expected to be easier to implement and more accurate on a miniaturized chip involving hundreds of thousands of qubits [9].
Moreover, semiconductors grant optimal physical properties for the creation of qubits with long coherence times. The coherence time of a qubit is a measure

of how long the qubit can keep its phase information before losing it [10]. Therefore, it is a critical parameter for the performance of the quantum device. The long coherence times in semiconductors allowed the conduction of experiments on qubits with fidelities above 99%.
Recently, the feasibility of reliable *hot* semiconductor qubits has been demonstrated [11]. The hot qubits operate at higher temperature (1-4 K) than other quantum computing devices, e.g. base on superconductors ($\sim$ mK). This reduces the cooling power needed for the device functioning, favouring the prospect of practical quantum computation.
Nowadays, the main goal is to demonstrate the feasibility of fault-tolerant quantum computers with few qubits in semiconductors, so that research can focus on the device scaling and integration, possibly realizing integrated chips with quantum core and classical electronics together to exploit the advantages of both. A possible approach for a hybrid quantum computer might be to separate the classical electronics from the quantum core and to keep them at different temperatures (Figure 1.1).

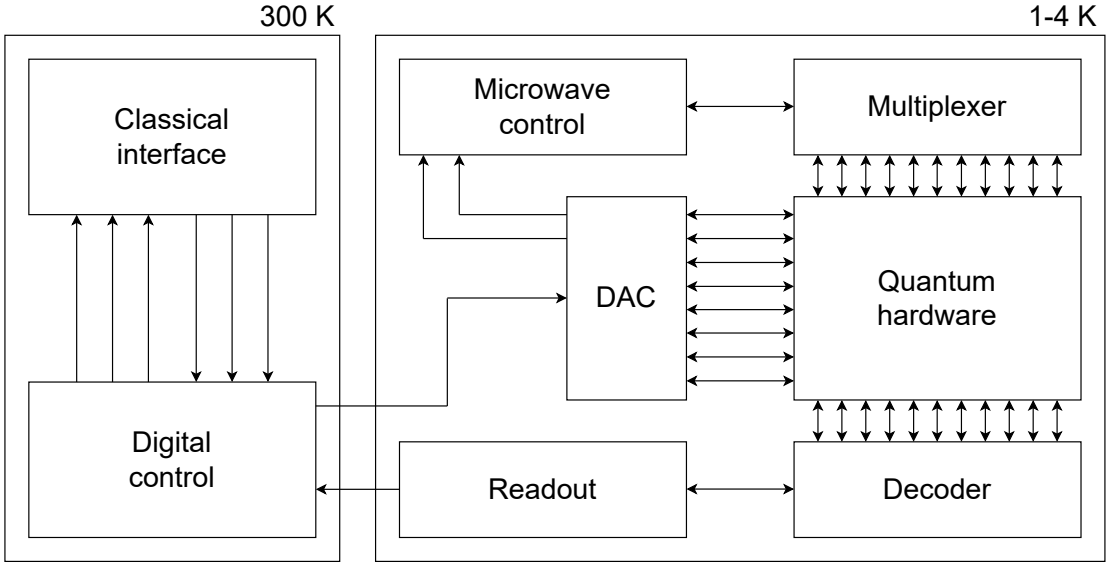

Figure 1.1: Possible scheme of a hybrid quantum computer.

1.1.2 Available implementations

The feasibility of qubits has been demonstrated in different material, such as silicon, which will be explored in this thesis, germanium [5], gallium arsenide [6] and silicon carbide [7]. Among these, silicon is the most relevant one, since the technology employed for the creation of silicon qubits notably resembles present-day complementary metal-oxide semiconductor (CMOS) manufacturing. The possible

qubit implementations in silicon span an enormous ecosystem and are extremely versatile in terms of their applications, which go from quantum simulation and computation to sensing or communication. The most diffused technologies are:

- Gate defined quantum dots (Figure 1.2a);
- Dopant atoms (Figure 1.2b);
- Optically addressable quantum defects (Figure 1.2c).

Quantum dots, which are the technology studied in this thesis, have a relatively small qubit footprint ($\sim$ nm), very fast single and two-qubit gates and fault-tolerant operation, making them a promising candidate for quantum computation. Dopant atoms [3] have shown the longest coherence times in solid-state quantum computing and a high sensitivity to magnetic fields, and thus they are the most suitable option for quantum memories and sensing. Instead, optically addressable quantum defects [4], such as nitrogen-vacancy (NV) centers in diamond or silicon carbide, can be employed for long-distance quantum communication, as they naturally serve as spin–photon interfaces [12].

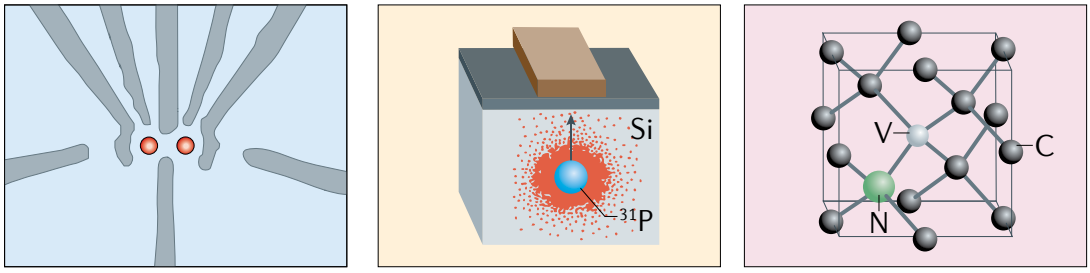

(a) Gate defined QDs. (b) Phosphorus dopant atom. (c) NV defect.

Figure 1.2: Different implementations of semiconductor quantum computing. Adapted from [12].

A comparison between the technologies is reported in the following table; the values are extracted from [12]. Some relevant parameters are shown, indicating that gated spins the general performance of each implementation.

Technology	Coherence time	Single-qubit gate time	Fidelity
Gated spin	28 ms	25 ns	99.96%
Dopant atoms	35.6 s	$\sim$20 µs	99.98%
NV centers	1 s	20 ns	99.995%

1.2 Quantum device simulation issues

The simulation of a quantum device is a crucial tool needed by quantum circuit designers and algorithms developers to estimate the performance of a given circuit on a silicon quantum computer. This gives the possibility of device optimization, making quantum device simulation a necessary step towards quantum computing implementation. The modelled structure must be realistically close to the physical hardware to be simulated as reliably as possible. Therefore, the model should also include noise sources, such as relaxation and decoherence [13], since they play a relevant role in the device performance. If the model simulation is accurate, the behaviour of the device can be predicted and the execution of the quantum circuits can be optimized, varying the system physical constants, such as the quantum dot g-factor or the valley splitting, and control parameters, such as the electric and magnetic fields applied.

1.2.1 The compact model idea and the Lindblad equation

Realistic quantum simulation proves to be not so simple to perform. In fact, in quantum physics, the time-evolution of the quantum system state is described by the Schrödinger equation:

$$j\hbar\frac{d}{dt}\left|\psi(t)\right\rangle = H(t)\left|\psi(t)\right\rangle, \tag{1.1}$$

where t is the time, $|\psi(t)\rangle$ is the state vector of the system and $H(t)$ is the time-dependent Hamiltonian operator. The problem of this approach is that this equation only deals with state vectors, which in turn can only describe pure quantum states. However, a realistic simulation must take into account incoherent phenomena, such as relaxation and decoherence, to consider quantum noise. Therefore, the *Lindblad master equation* [14] should be used. Indeed, it is an extension of Equation (1.1) and works with the system density matrix:

$$\frac{d\rho}{dt} = -\frac{j}{\hbar}[H(t),\rho] + \sum_j [2L_j\rho L_j^\dagger - \{L_j L^\dagger, \rho\}], \tag{1.2}$$

where ρ is the system density matrix, L_j is the Lindblad operator, $[x, y] = xy - yx$ is the commutator operator and $\{x, y\} = xy + yx$ is the anticommutator one.
Unfortunately, solving this equation means that one has to find the solution of a complex system of differential equations. This dramatically increases the simulation time and the computational cost of a quantum simulation. Hence, the idea of realizing a compact model (Figure 1.3): the goal to find a way to efficiently describe a quantum device, looking for a compromise between high accuracy in the description of qubits noise sources and low computational complexity, which would allow fast simulations. A good compact model can thus reliably simulate a

quantum hardware in a more effective and faster way with respect to a canonical quantum simulator. In order to achieve this, the simulation must include a certain number of approximations, which serves to speed up the simulation. However, these approximations inevitably introduce an error in the model; indeed, a compact model has always an amount of error with respect to the realistic simulation. It is important to estimate this error comparing the results of both simulations, possibly varying some input parameters to analyze the error behaviour with respect to them and apply possible improvements to the compact model to enhance its performance.

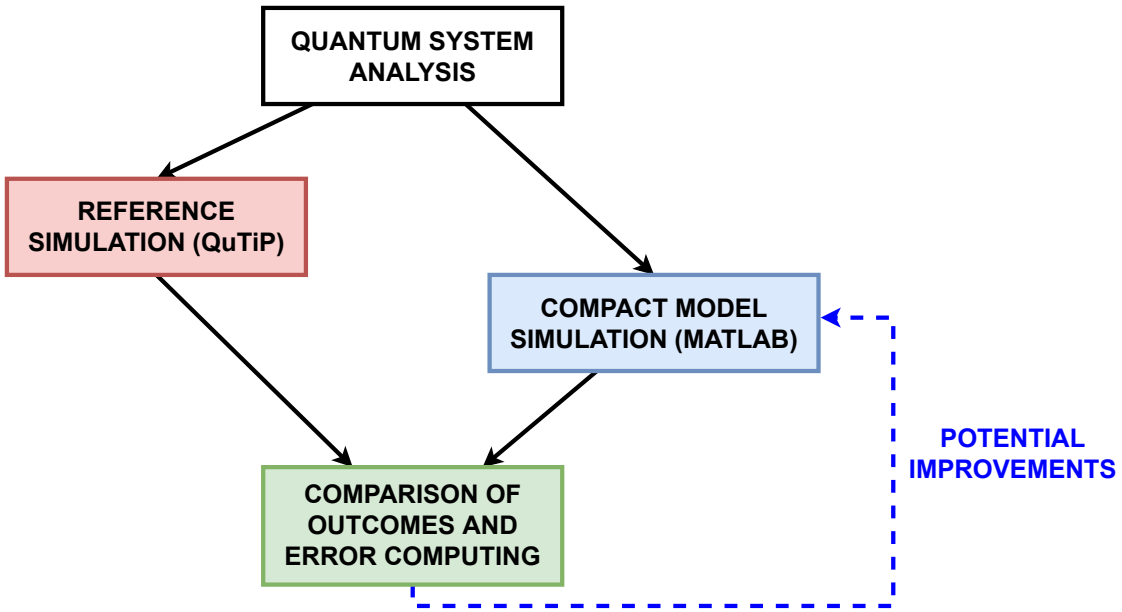

Figure 1.3: Methodology of a compact model.

1.2.2 Model realization

The workflow for the realization of the compact model has several steps (Figure 1.4). The first, described in Section 5.1.1 and in Section 5.1.2, is the theoretical definition of the system: this part comprises the assembling of the spin Hamiltonian for the description of quantum gates, which depends on the device manipulation techniques. Then, an approach for neglecting time-dependent terms of the Hamiltonian is exploited to find a time-independent expression, which in turn can be used to easily derive the system unitary evolution and speed up the simulation. This step is explored in Section 5.1.3 and in Section 5.1.4. However, the Hamiltonian undergoes an approximation, hence a certain amount of error is introduced into the model. The unitary evolution associated with the obtained Hamiltonian is used by

the model to calculate the system noiseless time-evolution. The non-ideal effects, i.e. relaxation and decoherence, are taken into account through a quantum noise algorithm, developed in [15] and implemented according to the methodology described in Section 6.1.1. The model is then validated through a comparison with a "reference" realistic quantum simulator to explore the limits of the simulation approximations. Section 6.2.2 is devoted to the analysis of the model validation.

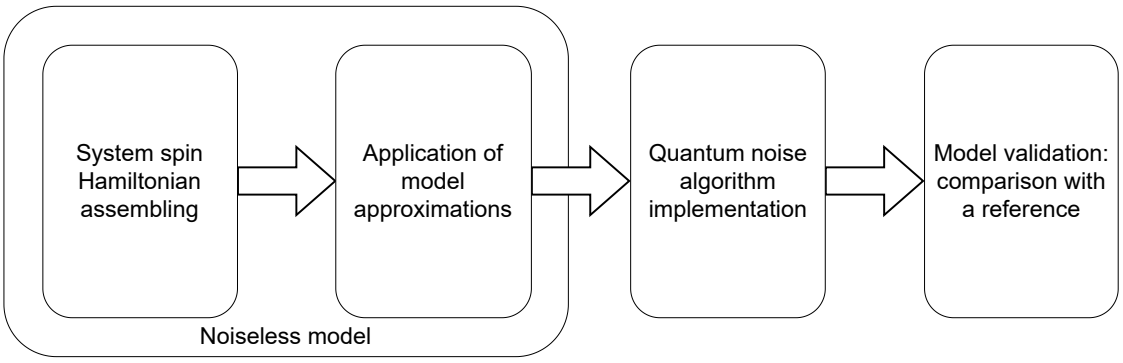

Figure 1.4: Compact model workflow.

The compact model has been developed on MATLAB and it takes as input the parameters that characterize the physical system, such as the g-factors of the dots and the amplitudes of the magnetic fields. The simulation take two separate paths: one computes an ideal evolution, applying the formal unitary matrices of the gates to the system state vector $|\psi\rangle$; the other path calculates the unitary evolutions of the applied gates through the formulas derived from the theoretical work and it also uses a quantum noise algorithm to consider relaxation and decoherence. This non-ideal path is applied to the density matrix ρ, so that the output of the model gives a reference ideal $|\psi\rangle$ and a ρ that takes into account the device realistic processes. The discrepancy between the two simulations is measured through the use of the *fidelity* concept [16].
The whole compact model has been finally compared with a numerical quantum simulator in Python, QuTiP, able to solve the Lindblad master equation. The error between the two approaches has been analyzed for the application of single and two-qubit gates and for the simulation of relevant quantum circuits, such as the realization of a Bell state and the SWAP gate, and two algorithms: the Deutsch's algorithm and the Grover's algorithm.

Chapter 2

Quantum confinement in semiconductors

One of the key building blocks of semiconductor quantum computing is the ability to dimensionally confine particles by means of heterostructures or electrically applied potential wells. Being able to fully comprehend the theory behind these two methods and the physical effects they have on the structure means having good basis for the understanding of the more complex mechanisms that rule solid-state quantum world. This chapters is thus devoted to a brief but clear theoretical introduction to these subjects.

2.1 Semiconductors and heterostructures

2.1.1 Semiconductors electronic properties

Semiconductors are crystals, i.e. periodic dispositions of atoms, in which electrons behave following quantum mechanics rules, being described by proper *wavefunctions*, related to the allowed electron states. These states correspond to the allowed energy bands, which are notoriously relevant for determining the electronic behaviour of the material. In particular, the meaningful bands are the lowest energy band that lets electrons move freely in the semiconductor, the *conduction band*, and the highest energy band hosting electrons chemically bonded to the material nuclei, the *valence band*. These two bands are separated by a forbidden energy gap, called *bandgap* (Figure 2.1) [17].

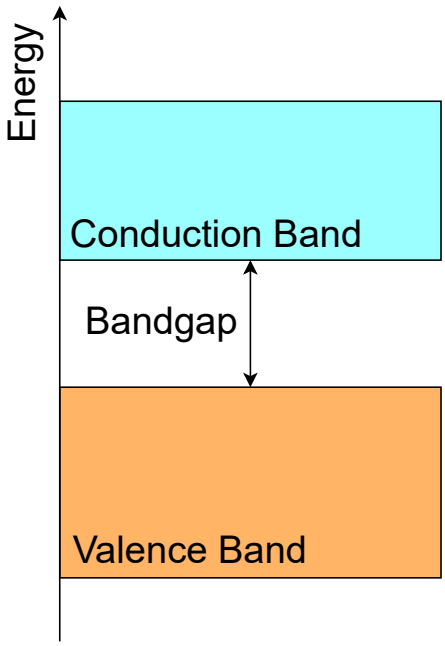

Figure 2.1: Semiconductor band diagram.

In this scenario, one can assume that, in the energy range of interest, electrons are described by a parabolic energy-momentum relation, also called *dispersion relation*:

$$E(\underline{k}) = E_C + \frac{\hbar^2|\underline{k}^2|}{2m} = E_C + \frac{\hbar^2\left(k_x^2 + k_y^2 + k_z^2\right)}{2m}, \tag{2.1}$$

where E is the energy of the electron and $\underline{k}$ its wavevector, associated with the particle momentum $\underline{p}$ through the *de Broglie* relation [17]

$$\underline{p} = \hbar\underline{k}, \tag{2.2}$$

k_x, k_y and k_z are the wavevector spatial components, E_C is the minimum of the conduction band and m is the electron mass.
This energy-momentum relation is defined in the reciprocal space, also called momentum space, i.e. the vector space containing all possible values of momentum for a particle, and it is a periodic function in it. The fundamental period of this function is called *Brillouin First Zone* (BFZ), which, technically, is the set of points in the momentum space closer to $|\underline{k}| = 0$ than to any other reciprocal lattice point [18].

2.1.2 Silicon energy-momentum relation

These general concepts can be applied to silicon, which is a key material for this thesis work, in order to visualize its main electronic features; in fact, silicon has a

diamond lattice, made of two interpenetrated face-centered cubic lattices, and its BFZ is a solid with eight hexagonal faces and six square faces (Figure 2.2). The main momentum points in the BFZ are its center (the Γ point), which is also the point where $|\underline{k}| = 0$, the center of the hexagonal face (the L point), and the center of the square face (the X point) [17].

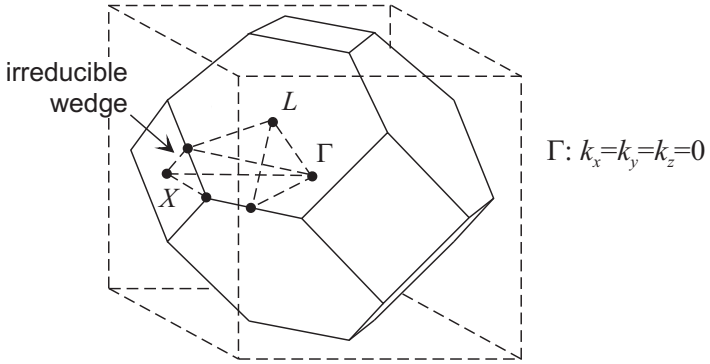

Figure 2.2: Brillouin First Zone of a diamond lattice. Adapted from [17].

The silicon energy-momentum relation (Figure 2.3) shows the material's main electronic characteristics:

- Indirect bandgap: the maximum of the valence band and the minimum of the conduction band correspond to different momentum points;
- Conduction band degeneracy: the conduction band has six degenerate minima (see Section 2.2.2).

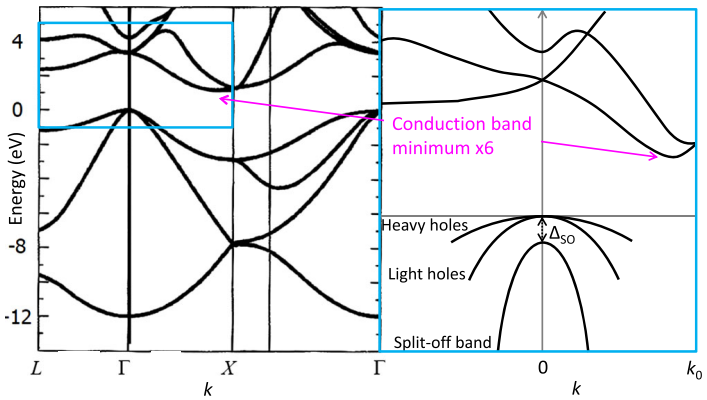

Figure 2.3: Silicon energy-momentum relation. Adapted from [19].

2.1.3 Heterojunctions and heterostructures

Epitaxial techniques can be employed to grow different materials on top of each other, creating a mixed structure. However, generally, each material has a different lattice constant a, which is the spatial distance between two atoms in the crystal lattice; this structural mismatch creates impurities and defects at the interface between the two materials, thus making the resulting mixed system unsuited for electronic applications. Nevertheless, if the lattice mismatch is very small (1% utmost), the crystal lattice is almost unaffected at the interface between the two materials and a practically ideal crystal is created: such structure is called *heterojunction* [20].
The electronic properties of the whole crystal now face an abrupt discontinuity, and this is particularly useful since it allows bandstructure engineering: a heterojunction between two materials with different bandgaps results in a discontinuity of the conduction and valence bands (Figure 2.4).

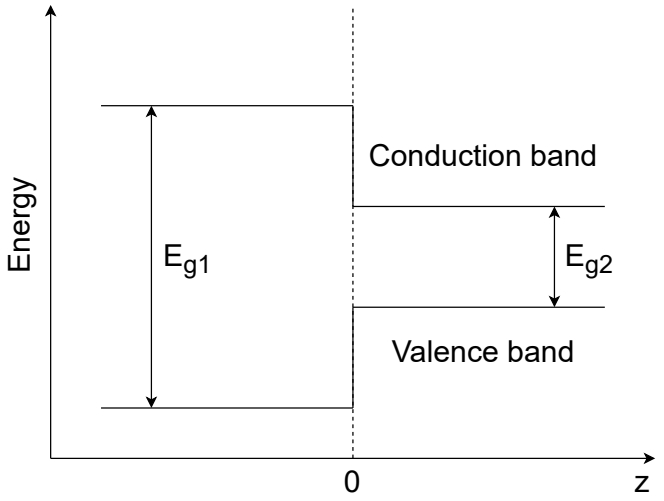

Figure 2.4: Bandstructure of a heterojunction between two materials with different bandgaps.

Combining different materials with different bandgaps gives rise to arbitrarily defined potential shapes; such architectures are called *heterostructures* [21]. For the purposes of this thesis, the focus will only be on a particular potential configuration, the *square well* potential (Figure 2.5).

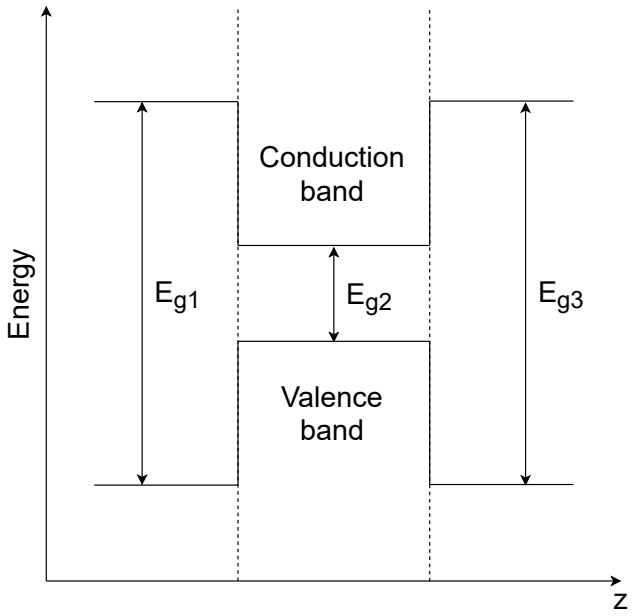

Figure 2.5: Square well potential obtained through a heterostructure made of three materials.

2.2 Quantum confinement in potential wells

2.2.1 Particle in a one-dimensional square well

The problem of a particle in a "box" is commonly used to explain the differences between classical and quantum physics: in classical mechanics, a particle trapped in a box can have any energy (meaning it can move at any speed), and could also stay "still", namely the ground state of the system is at zero energy (Figure 2.6a). However, when quantum effects become relevant, i.e. when the box width is comparable with the wavelength of the particle, quantum mechanics must be employed to analyze the system; this carries out that the energy states of the particle are actually quantized and the ground state is always at energies different from zero (Figure 2.6b).
In particular, supposing that a potential well is applied along the z direction and if it is considered infinitely "tall", i.e. the barrier potential is infinite, the analytical formula of the quantized energy states, also called *bound states*, is

$$E_{z_{n_z}} = \frac{n_z^2 \pi^2 \hbar^2}{2mL_z^2}, \tag{2.3}$$

while the related wavefunctions along the z direction (Figure 2.7) are expressed as

$$\psi_{n_z}(z) = \sqrt{\frac{2}{L_z}} \sin\left(n_z \frac{\pi}{L_z} z\right), \tag{2.4}$$

where $n_z = 1, 2, ..., N$ indicates the energy level position ($n_z = 1$ is the *ground state*, while $n_z = N$ is the highest energy state in the quantum well), m is the particle mass and L_z is the well width. For finite values of the barrier potential, numerical or graphical methods must be used; if applied in this case, the analytical formula of Equation (2.3) gives more bound states than there actually are, since it is only valid for the infinite well case. Subbands are thus created: the energy is quantized along the z direction, so the energy-momentum relation in a quantum well is

$$E_{n_z} = E_C + E_{z_{n_z}} + \frac{\hbar^2 \left(k_x^2 + k_y^2\right)}{2m}, \tag{2.5}$$

where E_C is the minimum of the conduction band, while $k_x = \sqrt{\frac{2m}{\hbar^2} E_x}$ and $k_y = \sqrt{\frac{2m}{\hbar^2} E_y}$ are the x and y wavenumbers, with E_x and E_y kinetic energies of the particle in the respective directions. This relation means that there are n_z 1D subbands, each having a 2D dispersion relation $E(k_x, k_y)$ [22]. In addition, owing to the separation of the spatial variables - only allowed when the potential profile can be separated as well ($U(x, y, z) = U_x(x) + U_y(y) + U_z(z)$) - the total spatial wavefunction can be written as

$$\psi_{n_z}(x, y, z) = \sqrt{\frac{2}{L_z}} e^{jk_x x} e^{jk_y y} \sin\left(n_z \frac{\pi}{L_z} z\right). \tag{2.6}$$

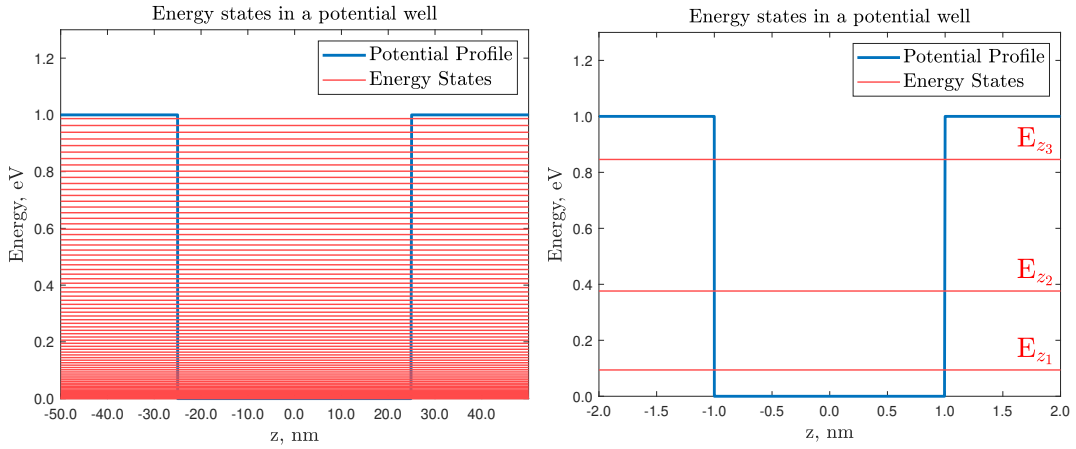

(a) Potential well of 50 nm.

(b) Potential well of 2 nm.

Figure 2.6: The well (a) is not narrow enough to show quantum behaviours while, in (b), energy states are clearly quantized because of quantum effects.

Furthermore, quantum effects also affect the *density of states* N(E), which is the number of different states per energy per unit volume that electrons are allowed to occupy. The bulk 3D-DOS is computed as

$$N_{3D}(E) = \frac{1}{2\pi^2} \left(\frac{2m}{\hbar^2}\right)^{\frac{3}{2}} \sqrt{E}, \tag{2.7}$$

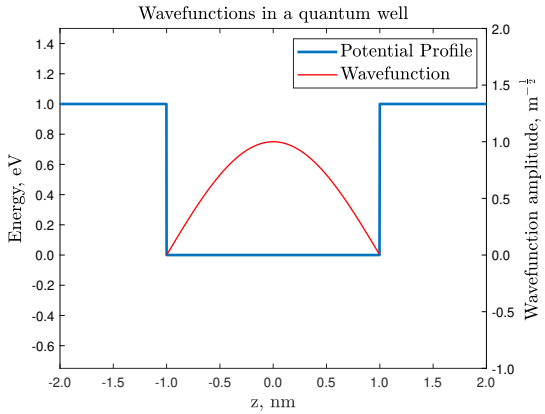

(a) Wavefunction of the first energy state.

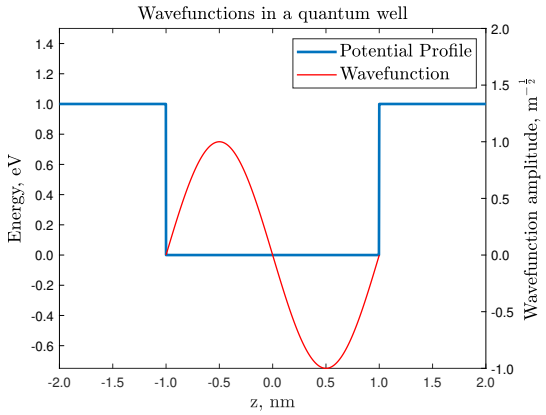

(b) Wavefunction of the second energy state.

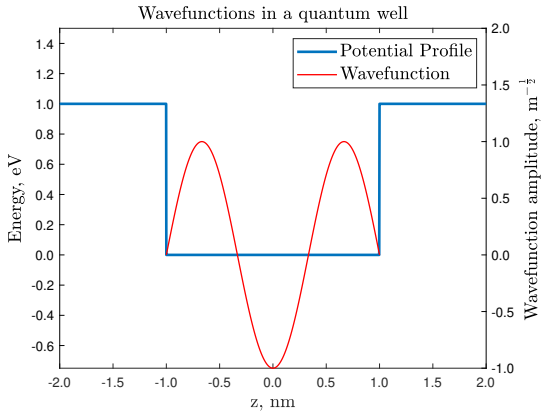

(c) Wavefunction of the third energy state.

Figure 2.7: Wavefunctions associated with the bound states of a 2 nm quantum well.

showing its well known square root behaviour. On the other hand, in quantum wells, the quantization of the energy levels in the confinement direction causes the DOS to lose the energy dependence, making it a constant function in each subband (Figure 2.8):

$$N_{2D}(E) = \frac{m}{L_z \pi \hbar^2} \sum_{n_z} \theta(E - E_{n_z}), \tag{2.8}$$

where $\theta(E - E_{n_z})$ is the Heaviside step function centered in $E - E_{n_z}$ [22].

2.2.2 Quantum Wires and Quantum Dots

Although until now the potential confinement has been applied only in one direction, the analytical results obtained can be used to examine the two-dimensional potential confinement too, also called *quantum wire*.

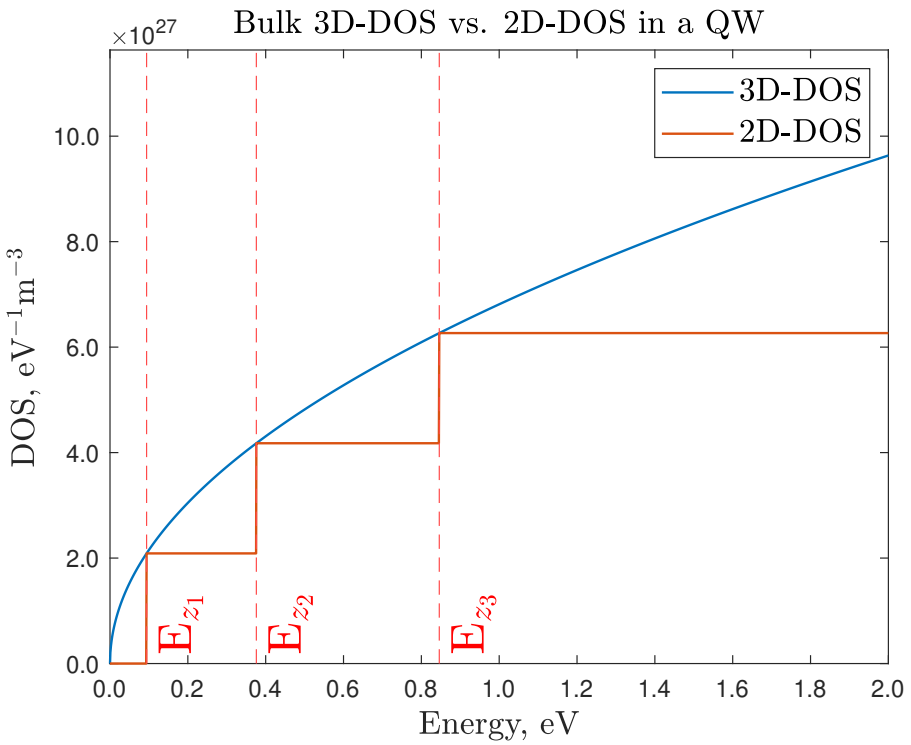

Figure 2.8: Comparison between bulk 3D-DOS and quantum well 2D-DOS.

Assuming confinement along x and y directions, energy levels are quantized and their formulas are

$$E_{x_{nx}} = \frac{n_x^2 \pi^2 \hbar^2}{2mL_x^2}, \tag{2.9}$$

$$E_{y_{ny}} = \frac{n_y^2 \pi^2 \hbar^2}{2mL_y^2}. \tag{2.10}$$

If $L_x = L_y = L$, the dispersion relation becomes

$$E_{n_x,n_y} = E_C + E_{x_{nx}} + E_{y_{ny}} + E_z = E_C + \frac{\pi^2 \hbar^2}{2mL^2}\left(n_x^2 + n_y^2\right) + \frac{\hbar^2 k_z^2}{2m}, \tag{2.11}$$

and therefore it depends on both n_x and n_y: subbands are now expressed as E_{n_x,n_y}, meaning that the particles transverse energy is quantized and that now there are 2D subbands, each having a 1D dispersion relation $E(k_z)$.
Again, due to the separation of spatial variables, the total spatial wavefunction is

$$\psi_{n_x,n_y}(x,y,z) = \sqrt{\frac{2}{L}} \sin\left(n_x \frac{\pi}{L} x\right) \sqrt{\frac{2}{L}} \sin\left(n_y \frac{\pi}{L} y\right) e^{jk_z z}. \tag{2.12}$$

The most powerful derivation from transverse energy quantization in quantum wires is that the wire resistance does not depend on its length and section (as in classical

wires) but it has a constant value $R_Q = M\frac{h}{2q^2} \approx M \cdot 12.9\ \text{k}\Omega$, where M is the number of subbands contributing to conduction.
Finally, the 1D-DOS shows infinite maxima around subband minima, i.e. where the charge is expected to accumulate (Figure 2.9) [23].

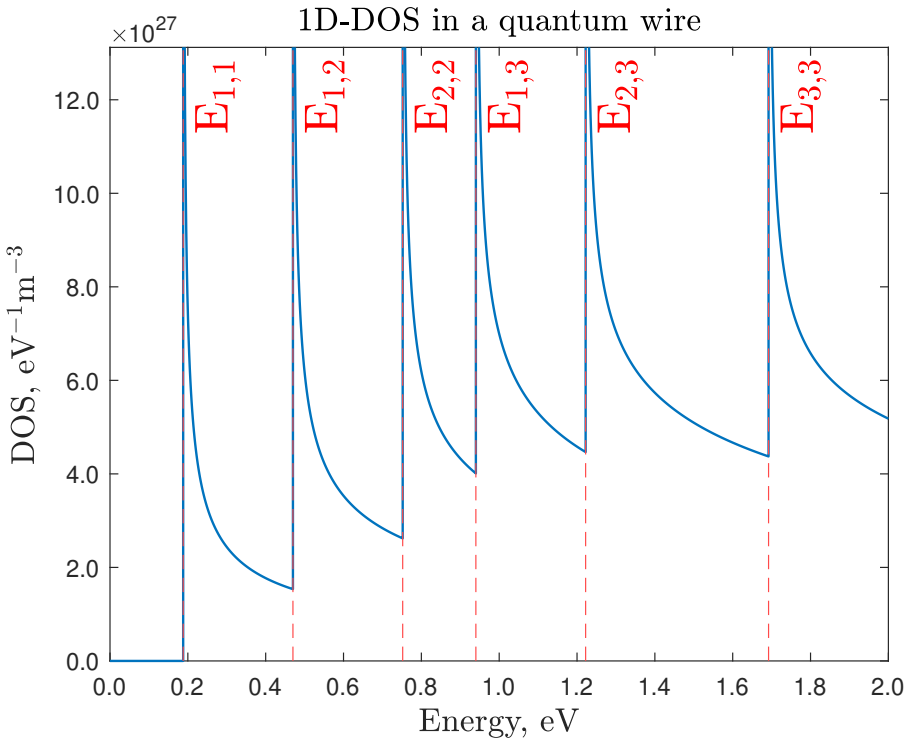

Figure 2.9: 1D-DOS in a quantum wire.

The last step towards complete particle confinement is to add the last potential constraint (in the z direction) to the quantum wire structure; the resulting system is called *quantum dot*. The particle is now locked in space and can only occupy discrete energy levels inside the dot: this means that there are no dispersion curves (E does not depend on any spatial component of $\underline{k}$), since the dispersion relation in a quantum dot, assuming $L_x = L_y = L_z = L$, is

$$E_{n_x,n_y,n_z} = E_C + E_{x_{n_x}} + E_{y_{n_y}} + E_{z_{n_z}} = E_C + \frac{\pi^2\hbar^2}{2mL^2}\left(n_x^2 + n_y^2 + n_z^2\right), \qquad (2.13)$$

and therefore the DOS only depends on the number of confined states. An isolated quantum dot offers two spin-degenerate states for each confined energy level, so the DOS plot is a series of δ-functions centered at each energy level, which, since energies are quantized in every direction, is addressed as E_{n_x,n_y,n_z} (Figure 2.10) [24].

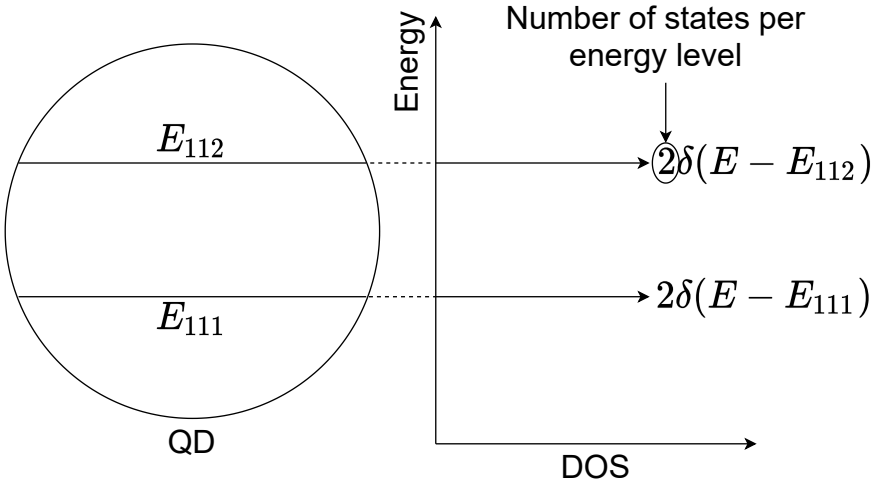

Figure 2.10: Energy levels and DOS in a quantum dot.

As already mentioned in Section 2.1.2, bulk silicon has a sixfold degenerate conduction band minimum. In addition to the particle spatial confinement, quantum dots lift this degeneracy: the large in-plane tensile strain in the dot breaks the conduction band minimum into two levels: a higher fourfold degenerate level and a lower twofold degenerate one. These levels are broken once more by the confinement and the electric fields in the dot [19]; the relevant effect is the lower energy level splitting δ_{VS}, called *valley splitting*, the energy difference between the system ground state E_{S-V} and the first excited state $E_{S-V'}$ (Figure 2.11). The valley splitting value varies depending on the structure: since the potential step at the Si/SiO_2 interface is very sharp, values of the order of 0.2 - 0.8 meV are reached in SiMOS structures [25, 26, 27], while Si/SiGe devices provide valley splittings between 0.01 and 0.2 meV [28, 29, 30, 31].

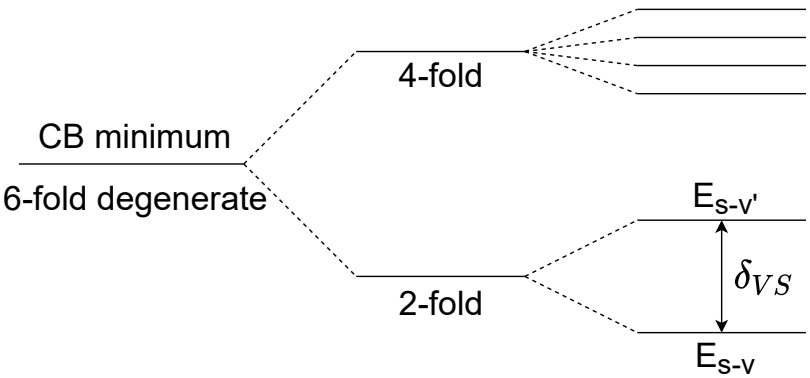

Figure 2.11: Valley splitting in a quantum dot.

2.3 Structure definition

2.3.1 2-Dimensional Electron Gas and gate-defined Quantum Dots

The analyses carried out in the previous paragraphs about quantum confinement show that when a quantum well is created in a three-dimensional system, the particles of such system, usually electrons, get "trapped" in the quantized energy levels and cannot move along the well direction: this is called *2-Dimensional Electron Gas* (2DEG) [32]. Such behaviour is employed in the creation of the Double Quantum Dot (DQD) structure analyzed in this thesis: a thin layer (∼10 nm) of enriched ^{28}Si is grown between a SiO_2 barrier insulator and the intrinsic Si substrate, and the 2DEG is formed due to the triangular quantum well (which has almost the same behaviour of the square quantum well) in the conduction band (Figure 2.12).

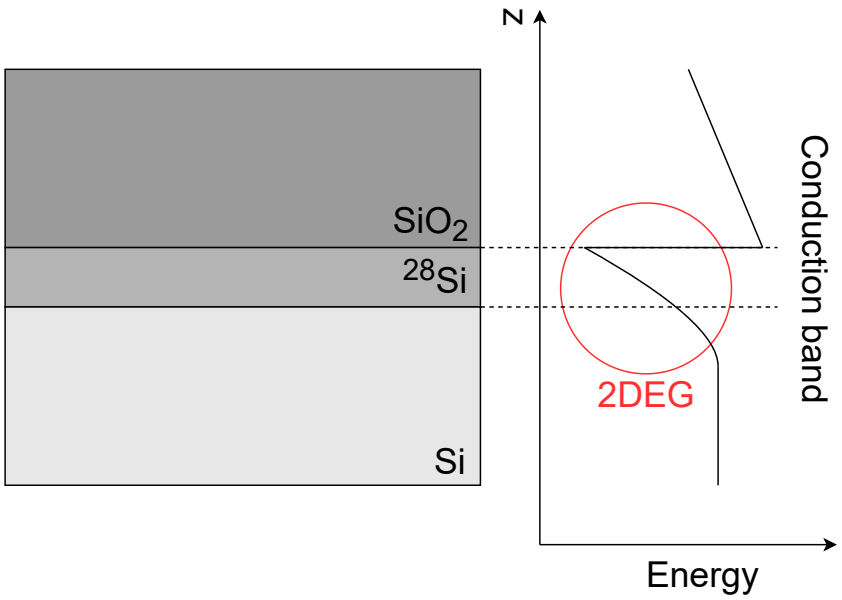

Figure 2.12: 2DEG is created in the thin enriched ^{28}Si layer.

1D confinement along the z direction is thus obtained through a heterostructure, while, for the other two directions, the confining potential is applied through electrical metallic gates, placed on top of the barrier insulator: in particular, the light green gates confine the electrons in the y direction (Figure 2.13), while the actual double quantum dot potential is formed along the x direction through the *plunger* gates, which control the potential wells needed to create the two dots and lateral electron reservoirs, and the *barrier* gates, which tune the barrier potentials between the two dots and between the dots and the reservoirs (Figure 2.14) [33].

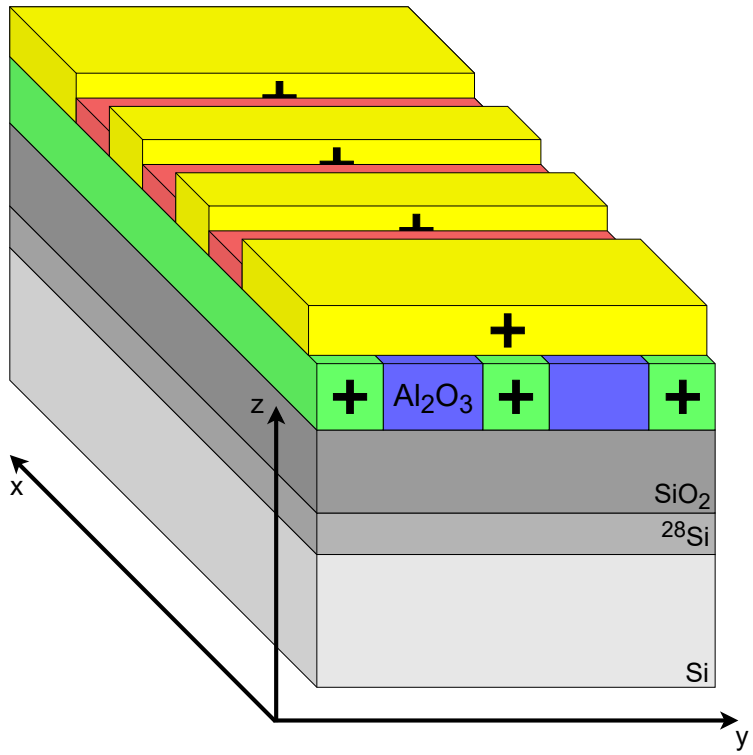

Figure 2.13: 3D view of the gate-defined DQD structure.

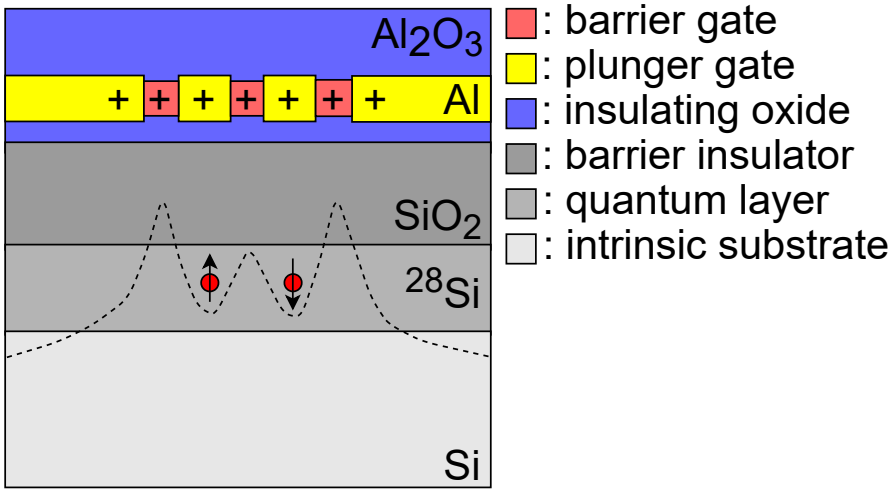

Figure 2.14: XZ cut of the gate-defined DQD structure.

The two quantum dots are formed in the thin layer of enriched ^{28}Si; this material is used since natural Si contains about a 4.7% concentration of ^{29}Si isotopes, which possess a non-zero nuclear spin, and this negatively affects electron spin performance in the quantum dot. In fact, the 29-isotope nuclei interact with each other and couple to the electronic spin through hyperfine interaction, worsening the coherence time of the device. The 28-isotope of Si, instead, has zero net nuclear spin and completely eliminate this issue, making enriched ^{28}Si a very good material for the realization of the quantum layer [34].

2.3.2 Measuring the system: the SET sensor

Creating the two-levels quantum system and being able to manipulate it is just a part of the quantum computing device; in fact, one has to be able to measure it, reading the state of the system in order to analyze the behaviour of the device. Therefore, an appropriate sensor is needed in the vicinity of the double quantum dot zone: the single electron transistor (SET) charge sensor. A SET is formed by a quantum dot with three terminals (the drain, the source and the gate), meaning that it can be realized with the same photolithographic steps of the quantum system, so that the technological complexity is not dramatically increased; in this device, electrons flow between source and drain thanks to tunnelling, and the potential of the dot is tuned by the gate electrode, which is capacitively coupled to the dot (Figure 2.15) [35].

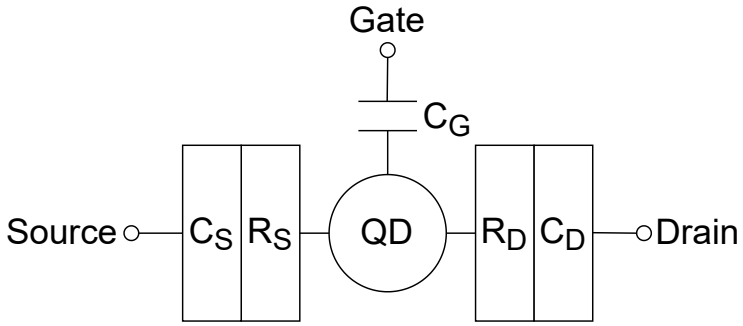

Figure 2.15: Schematics of a SET.

The SET can be used as a sensor [36] if it is created close enough to the double quantum dot region: a capacitive coupling is formed between the SET and the quantum system, making the potential of the sensor dependent on the electrostatic landscape of the quantum dots, i.e. on the presence/absence of electrons in the two quantum dots (Figure 2.16). Thus, the SET current can be used to detect tunneling events in the device; this is a significant tool for the read-out of the system (Figure 2.17) [37].

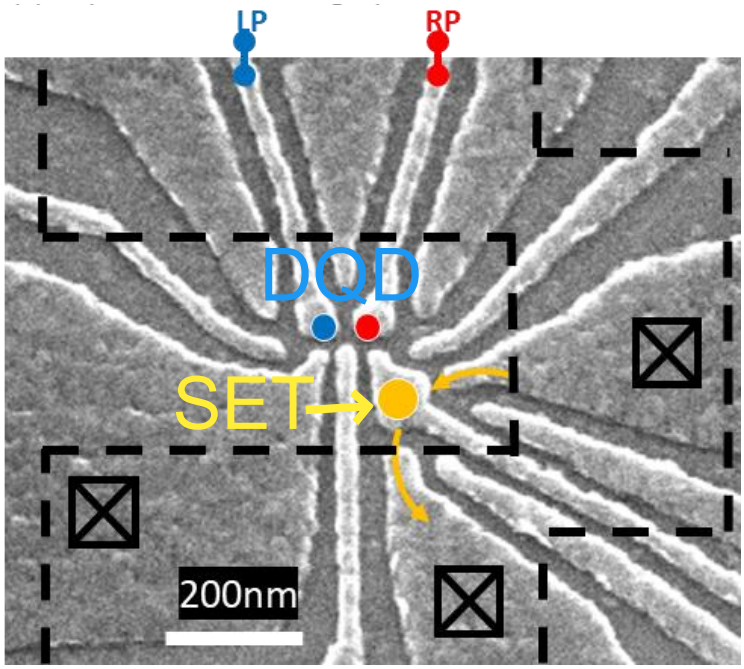

Figure 2.16: Scanning Electron Micrograph (SEM) image of the device; the two quantum dots and the SET are clearly visible. Adapted from [38].

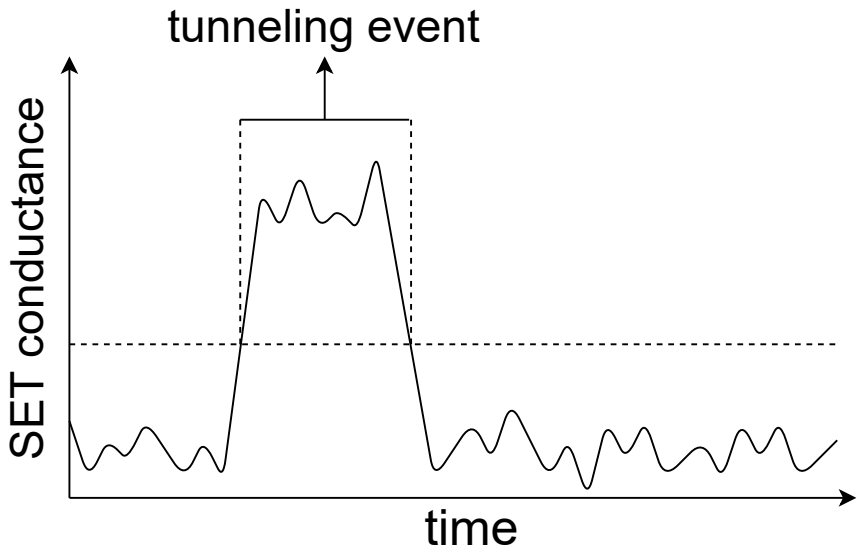

Figure 2.17: The SET conductance sharply increases when there is a tunneling event in the quantum device.

2.3.3 The charge stability diagram

SET measurements offer the possibility of electrically characterizing the structure. One of the most meaningful analysis is to study how the dots occupancy vary when sweeping the plunger gates voltages. Indeed, these electrodes are used to drive the system into a specific electrostatic regime, and this is clearly shown by the *charge stability diagram*. The notation for the dots occupancy, extensively used throughout this work, is (N_L,N_R), where N_L describes how many electrons are in the left dot and N_R indicates how many electron are in the right one. The SET is used to detect tunneling events in order to identify when the system is varying its electrostatic landscape. Precisely knowing which values of the plunger gates voltages apply in order to be in a particular occupancy regime is a precious tool to ensure an accurate device control.

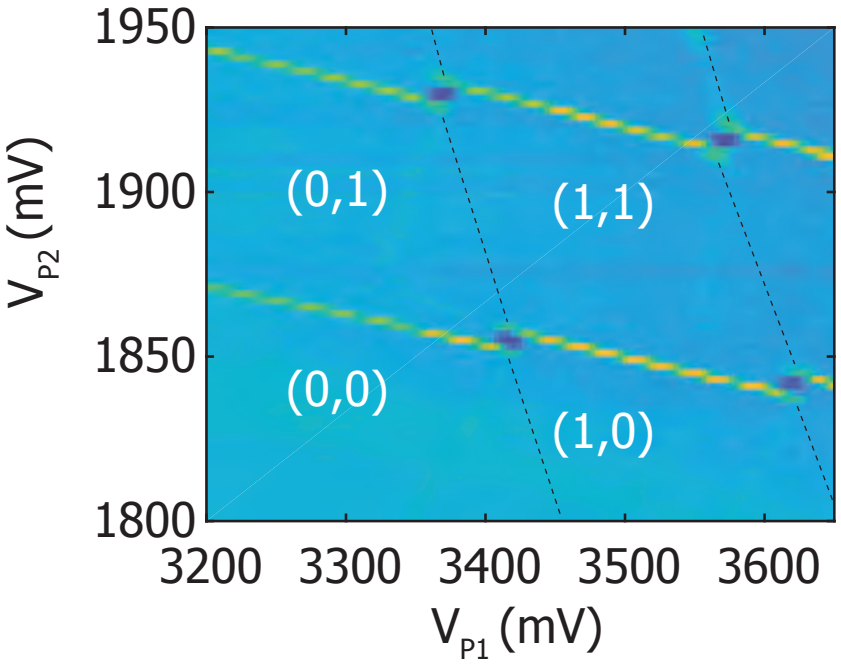

Figure 2.18: Charge stability diagram of a DQD device. P_1 and P_2 are the plunger gates. Adapted from [39].

Part II

Quantum system definition

Chapter 3

Device functioning analysis

This chapter is dedicated to the description of how the device defined in previous chapter works. Different qubit encoding possibilities are inspected, with particular attention to the advantages of each choice. Read-out and initialization methods are explored, as well as device control procedures, in order to familiarize with the technology relevant parameters, extensively used in the next chapters.

3.1 Qubit encoding

3.1.1 Spin-$\frac{1}{2}$ coding: the Loss-DiVincenzo qubit

The easiest way of realizing a qubit is by employing the spin of a single electron [1]. As already mentioned in Section 2.3.1, the confinement and the strain in a quantum dot structure break the conduction band minimum degeneracy, leaving a spin-degenerate ground state. This means that this lower level can be occupied by two electrons with different spins. The two-levels quantum system is thus generated exploiting the *Zeeman* effect: the presence of a static magnetic field $\underline{B}_0$ splits the two spin levels. The energy difference E_Z between these spin states is called *Zeeman* energy (Figure 3.1) [40]. In this analysis, the static magnetic field is applied along the z direction, hence the spin states split by this effect are the $|\downarrow\rangle$ and $|\uparrow\rangle$ states. The lower state (spin-up or spin-down) is determined by the *g-factor* sign; this argument is explored in Section 4.1.1. In silicon devices, the lower state is the spin-down state [41, 8], thus the system spin Hamiltonian, written in the $\{|\uparrow\rangle, |\downarrow\rangle\}$ basis, is [42]

$$H = \begin{bmatrix} \frac{E_Z}{2} & 0 \\ 0 & -\frac{E_Z}{2} \end{bmatrix}, \tag{3.1}$$

and the qubit encoding is

$$\begin{aligned} |0\rangle &= |\downarrow\rangle\,, \\ |1\rangle &= |\uparrow\rangle\,. \end{aligned} \tag{3.2}$$

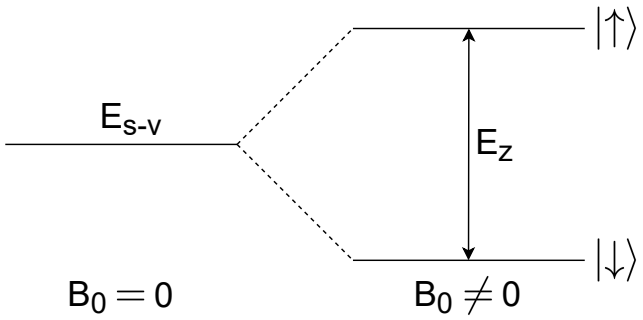

Figure 3.1: The Zeeman effect splits the spin states.

In this type of encoding, each quantum dot corresponds to a qubit and system manipulation is achieved through the use of the electrical gates − the same that form the quantum dots − and integrated micromagnets, needed to create static magnetic field gradients in the device. Since this is the encoding choice of the structure under analysis in this work, these concepts are studied in detail in the next chapters. Since the encoding is based on the electron spin, it is called a *spin encoding*. Spin encodings usually guarantee good coherence times ($\sim$ tens of µs) and acceptable manipulation times ($\sim$ tens of ns) [43].

3.1.2 The charge qubit

On the other hand, the *charge coding* encodes the qubit on the presence of a single electron in one dot or in another. Specifically, the charge qubit is realized through the use of one electron in two dots. The two quantum dots communicate through a non-zero tunnel coupling, that makes the travelling of the electron between the dots possible. The two states of the system are $|R\rangle$, that indicates the presence of the electron in the right dot, and $|L\rangle$, that implies that the electron is in the left dot. The system spin Hamiltonian, expressed in the $\{|L\rangle, |R\rangle\}$ basis, is [42]

$$H = \begin{bmatrix} \frac{\epsilon}{2} & t_0 \\ t_0 & -\frac{\epsilon}{2} \end{bmatrix}, \tag{3.3}$$

where ϵ is the energy difference between the dots, called energy *detuning*, and t_0 is the tunnel coupling, defined in energy units (J or eV). These two parameters can be effectively controlled through the electrical gates: the detuning is modified using the plunger gates above the dots, while the tunnel coupling is changed exploiting the barrier gate between the dots.
In order to understand this Hamiltonian and the whole system, one needs to look at the energy diagram of the structure, namely the plot of the Hamiltonian eigenvalues against the energy detuning between the dots. This diagram shows which energy

levels the system can occupy for each value of detuning; for sake of simplicity, suppose just for now that $t_0 = 0$. The Hamiltonian thus becomes

$$H = \begin{bmatrix} \frac{\epsilon}{2} & 0 \\ 0 & -\frac{\epsilon}{2} \end{bmatrix}, \tag{3.4}$$

and the energy diagram is trivial, since the matrix is already diagonal and the eigenvalues have a clear dependence on the detuning (Figure 3.2).

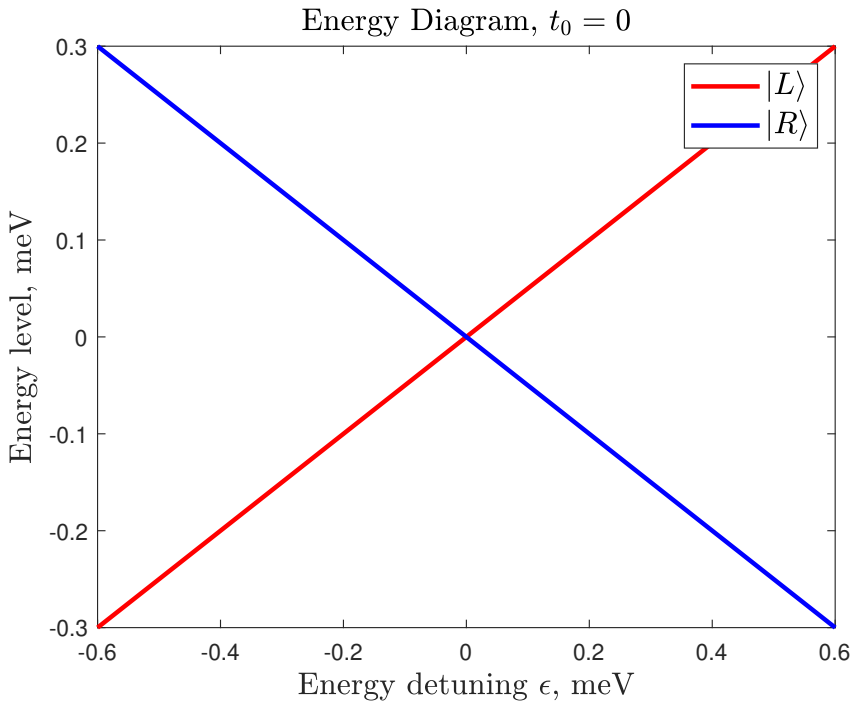

Figure 3.2: Energy diagram of the charge qubit when $t_0 = 0$.

Now, suppose that the electron starts in the left dot with negative detuning. Confronting the energy diagram and the energy detuning between the dots, defined as the difference between the left dot energy and the right dot energy:

- Negative detuning: the electron is in the left dot, which is the lowest energy state in the system (Figure 3.3);
- Zero detuning: the $|L\rangle$ and the $|R\rangle$ states are at the same energy, but the electron cannot tunnel to the other dot, since the tunnel coupling is zero (Figure 3.4);
- Positive detuning: the electron stays in the $|L\rangle$ state even if it is not the lower energy state in the system (Figure 3.5).

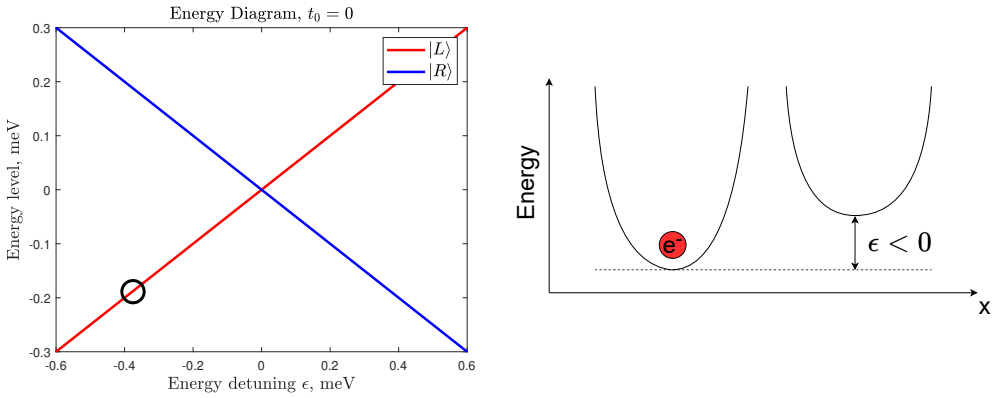

Figure 3.3: The electron starts in the $|L\rangle$ state for negative detuning.

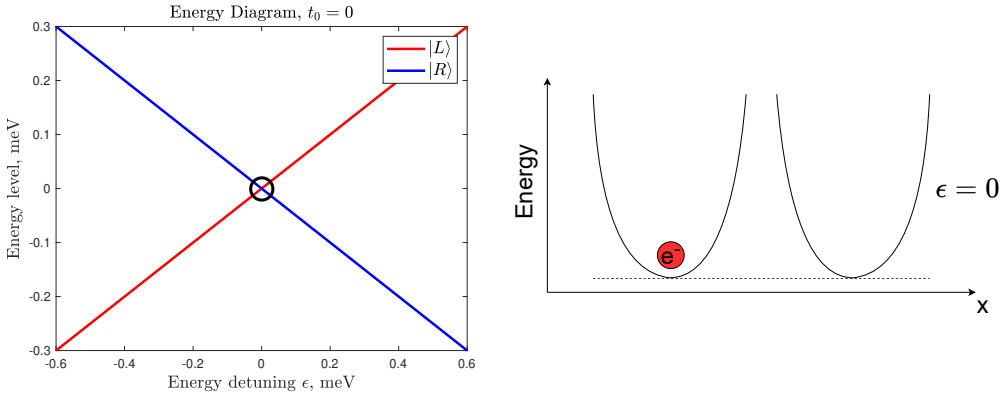

Figure 3.4: The electron cannot tunnel to the right dot when the detuning increases.

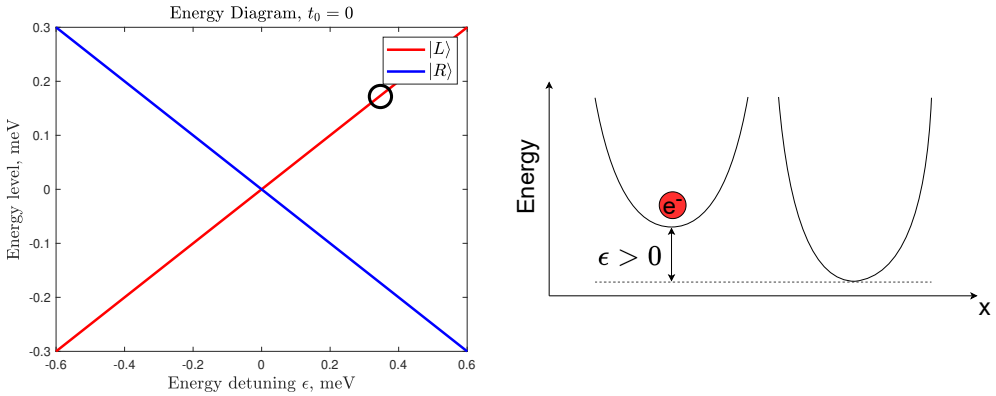

Figure 3.5: The electron is still locked in the $|L\rangle$ state.

On the contrary, when $t_0 \neq 0$, tunneling is allowed and the electron can change position, depending on which is the lowest energy state in the system. Indeed, the energy diagram shows that the $|L\rangle$ and $|R\rangle$ states are connected (Figure 3.6), while in $t_0 = 0$ case the two states did not communicate at all (Figure 3.2).

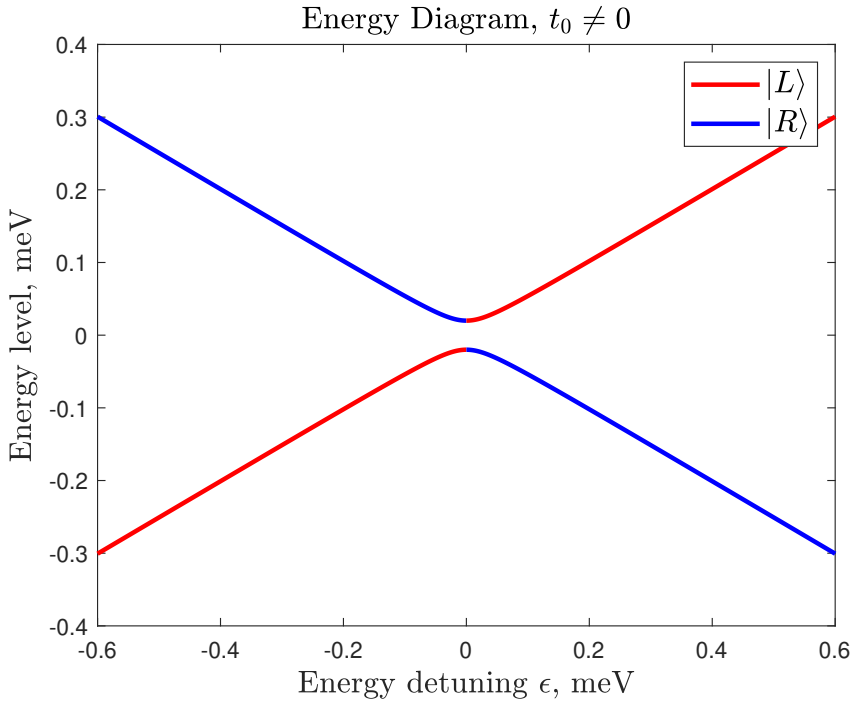

Figure 3.6: Energy diagram of the charge qubit when $t_0 \neq 0$.

Again, supposing that the electron starts in the left dot for negative detuning, the system evolves as follows:

- Negative detuning: the electron starts in the left dot, which is the lowest energy state in the system (Figure 3.7);
- Zero detuning: the $|L\rangle$ and the $|R\rangle$ states are at the same energy, and the electron begins the process of tunneling to the other dot (Figure 3.8);
- Positive detuning: the electron has changed position and the system in now in the $|R\rangle$ state, the lowest energy state (Figure 3.9).

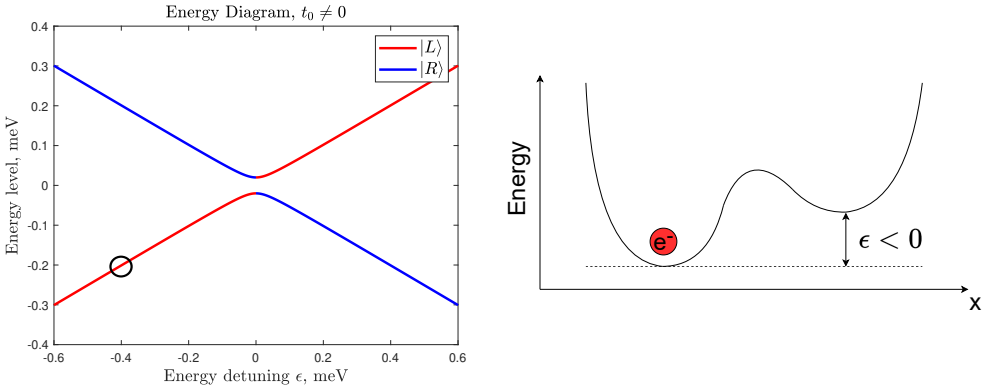

Figure 3.7: The electron starts in the $|L\rangle$ state for negative detuning.

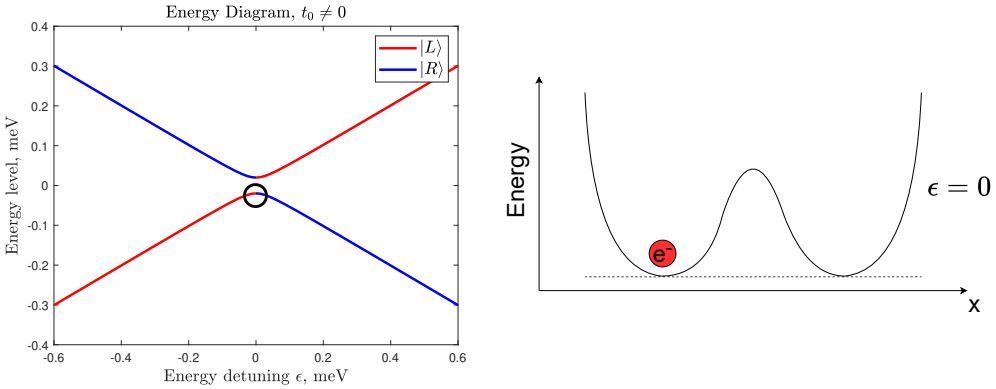

Figure 3.8: The electron starts the tunneling process.

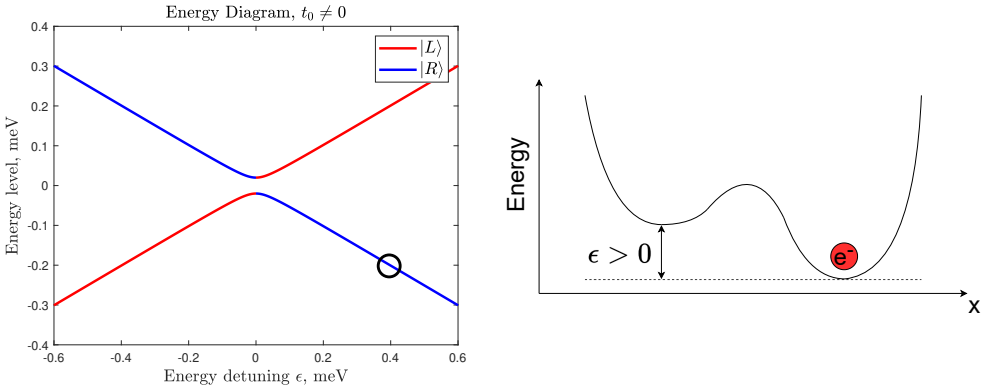

Figure 3.9: The electron is now in the $|R\rangle$ state.

The charge qubit encoding is thus

$$\begin{aligned} |0\rangle &= |L\rangle\,, \\ |1\rangle &= |R\rangle\,. \end{aligned} \tag{3.5}$$

and device manipulation can be achieved with just the control of the tunnel coupling and the detuning. Charge qubits generally show worse performance in terms of coherence times ($\sim$ tens of ns), but they greatly improve manipulation times ($\sim$ tens of ps) [44]. In order to exploit the long coherence of spin qubits and the fast control of the charge qubits, hybrid qubits (coded on both the position and the spin of an electron) have been proposed [45, 46, 47].

3.1.3 Singlet-Triplet coding

As demonstrated in the previous paragraph, the control of the detuning between the dots is easily achievable. This motivates the research towards a spin encoding that can be completely manipulated through the detuning. The Singlet-Triplet (ST) qubit serves this purpose; it is realized with two electrons in two quantum dots and makes use of the singlet and triplet states of this type of system. A singlet is, by definition, a state of a system in which the total spin quantum number s, computed using angular momenta addition formulas, is equal to 0. Conversely, a triplet is a state in which s is equal to 1, and thus there are three allowed eigenvalues m of the spin operator: $+1$, 0 and -1 [48].
The Singlet-Triplet coding is used in the (1,1) regime. This notation, already explained in Section 2.3.3, is not complete, since a state can be a singlet or a triplet: the full notations to uniquely identify a state in such structure are S(N_L,N_R), $\mathrm{T}_+(N_L,N_R)$, $\mathrm{T}_0(N_L,N_R)$ and $\mathrm{T}_-(N_L,N_R)$, where S stands for singlet state, and the three T notations are related to the three possible values of m: $+1$, 0 and -1, respectively. The relevant energy states of the system are thus

$$\begin{aligned} \mathrm{T}_+(1,1) &= |\uparrow\uparrow\rangle\,, \\ \mathrm{T}_0(1,1) &= \frac{1}{\sqrt{2}}\left(|\uparrow\downarrow\rangle + |\downarrow\uparrow\rangle\right), \\ \mathrm{T}_-(1,1) &= |\downarrow\downarrow\rangle\,, \\ \mathrm{S}(1,1) &= \frac{1}{\sqrt{2}}\left(|\uparrow\downarrow\rangle - |\downarrow\uparrow\rangle\right); \end{aligned} \tag{3.6}$$

S(2,0) and S(0,2) states need to be considered too, since they strongly couple to the S(1,1) energy state. However, the T(2,0) and T(0,2) states are at much higher energies and can be neglected. In fact, due to the Pauli exclusion principle, a triplet state with two electrons in a single dot means that one of the electrons must occupy the $E_{s-v'}$ dot level, which is sufficiently far away from the ground state E_{s-v} thanks to valley splitting.

In order to achieve single-qubit control of a Singlet-Triplet qubit - and this will be justified by Equation (3.8) - the difference between the Zeeman splittings of the two dots $\Delta E_Z = E_{Z_1} - E_{Z_2}$ must be different from zero. This is usually achieved through g-factor tuning [49] or the presence of a static magnetic field gradient along the dots direction, which makes each dot perceive a different effective B_0 [50].
In the $t_0 \gg \Delta E_Z$ limit, the $|\uparrow\downarrow\rangle$ and the $|\downarrow\uparrow\rangle$ states gets very close and become degenerate into the $T_0(1,1)$ and $S(1,1)$ states; this statement will be further developed in Section 5.1.1. The resulting energy diagram thus describes the interaction between the singlet states, while showing that triplet states cannot interact with singlets due to the Pauli Spin Blockade [51] (Figure 3.10). Furthermore, as expected, the Zeeman effect only applies to the triplet energy state, splitting the $T_+(1,1)$, $T_0(1,1)$ and $T_-(1,1)$ states, whereas it does not affect the singlets [52].

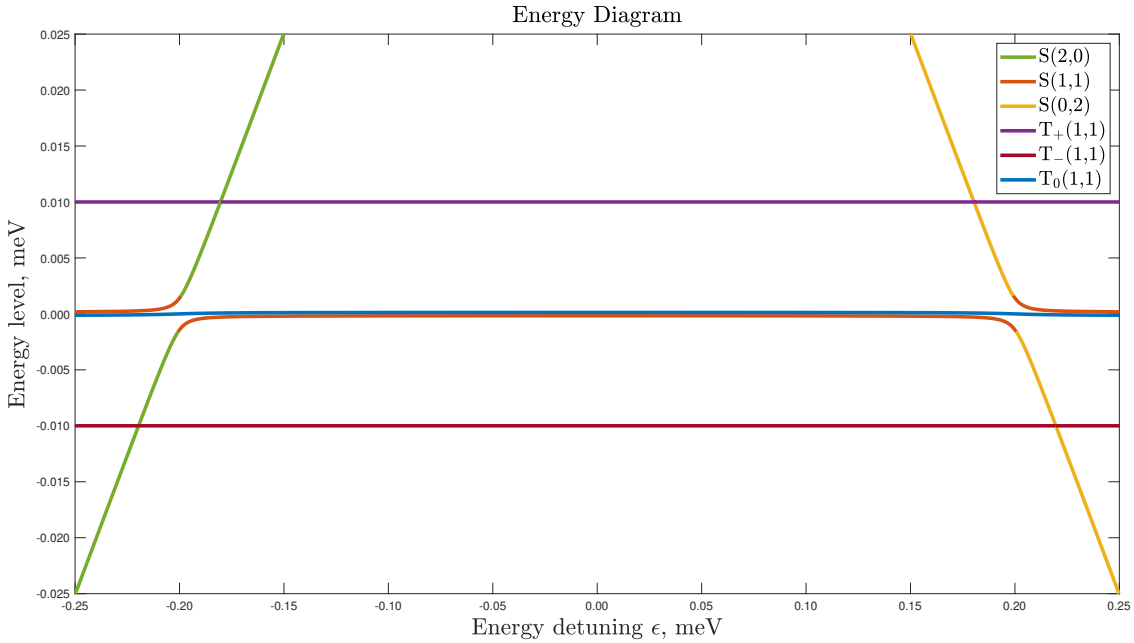

Figure 3.10: Energy diagram of a Singlet-Triplet qubit.

Since the qubit is encoded as

$$\begin{aligned} |0\rangle &= S(1,1), \\ |1\rangle &= T_0(1,1), \end{aligned} \tag{3.7}$$

one can conveniently reduce the Hamiltonian to the $\{T_0(1,1), S(1,1)\}$ basis, where it becomes [53, 54]

$$H = \begin{bmatrix} -hJ(\epsilon) & \frac{\Delta E_Z}{2} \\ \frac{\Delta E_Z}{2} & 0 \end{bmatrix}, \tag{3.8}$$

where $J(\epsilon)$ is the *singlet-triplet splitting*, also called *exchange interaction*, i.e. the energy difference between the $T_0(1,1)$ and the $S(1,1)$ states, defined in frequency

units (Hz). Since this parameter depends on the detuning ϵ, it can be turned off or on at will just by controlling the detuning value. This means that rotations around the z axis can be obtained setting the detuning near the S(1,1)-S(0,2) (or S(1,1)-S(2,0)) region, where $J \gg \Delta E_Z$, while rotations around the x direction are achieved extinguishing J ($\epsilon = 0$). Single-qubit control is thus accomplished just through detuning control (Figure 3.11).
ST qubit's performance is slightly better than the spin-$\frac{1}{2}$ one, with coherence times of the order of hundreds of µs and manipulation times of some ns [55].

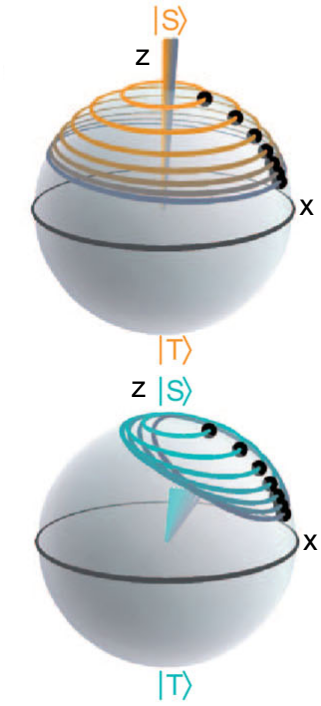

Figure 3.11: Singlet-Triplet qubit control. The upper Bloch sphere depicts single-qubit z rotations in the $J \gg \Delta E_Z$ regime, while the one below shows x rotations appearing as the J is turned off. Adapted from [42].

3.2 Read-out techniques

3.2.1 Elzerman method

As already mentioned in Section 2.3.2, the read-out of quantum dots devices is based on spin-charge conversion through the use of a nearby SET. The SET detects tunneling events thanks to the electrostatic coupling to the quantum dots, thus reading methods must be based on spin-selective tunneling, in order to be able

to derive the state of the dot from the presence (or absence) of this event. The first method was proposed by J. M. Elzerman in 2004 and therefore it carries his name [56]. The Elzerman readout consists in realizing electron reservoirs near the quantum dots and setting their Fermi levels between the spin-up and spin-down states of the dot to be read; this can be easily achieved through the plunger gate of the QD. The system can then act in two ways:

- The electron in the dot is in spin-down state: nothing happens, since the electron is already at the lowest energy state it can find;
- The electron in the dot is in spin-up state: there is a tunneling event between the dot and the neighbouring reservoir.

This means that, when this type of reading is performed, if the SET reveals a tunneling event, then the qubit was in spin-up state, otherwise it was in the spin-down one. Furthermore, if there is a tunneling event, the empty dot will be automatically filled by another electron, tunneling from the reservoir, in spin-down state (Figure 3.12). The Elzerman readout is thus also an initialization, since, after performing it, the qubit will surely be in spin-down state.

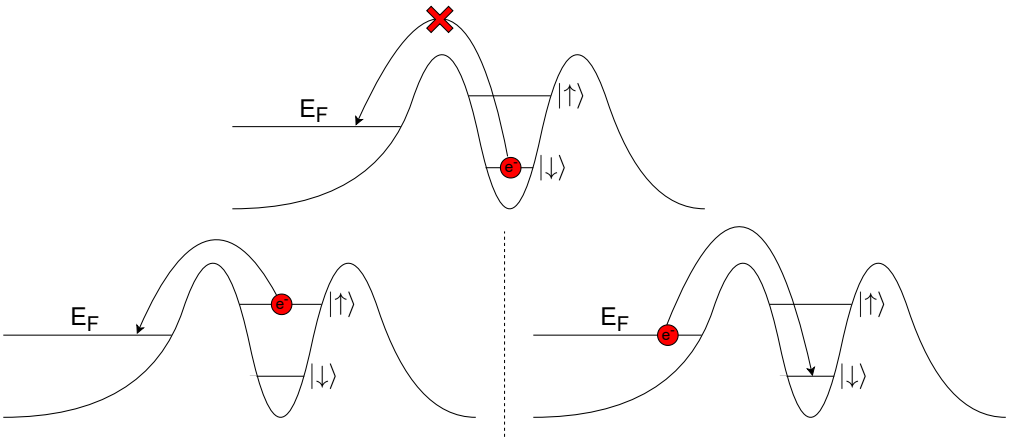

Figure 3.12: The two cases of Elzerman readout.

3.2.2 Pauli Spin Blockade method

The Elzerman technique is the easiest way to perform a read-out, but it poses a relevant issue: electron reservoirs must be available near every quantum dot in order to read them. This matter is solved through the Pauli Spin Blockade read-out, which indeed removes the need of reservoirs and instead makes use of *ancilla* qubits to create a double quantum dot systems with the target qubits to extract their state. The spin-selective tunneling is achieved through the Pauli Spin Blockade principle,

which forbids a system from passing from a triplet state to a singlet one [57].
Before performing the reading operation, the system is prepared in the (1,1) regime, and the reference ancilla qubit is intialized in a know state. Supposing that this state is $|\downarrow\rangle$, pulsing the detuning between the dots towards the (0,2) region (Figure 3.10 can be still used as a reference since it describes a DQD system) results in two scenarios:

- The electron in the target dot is in spin-down state: the system is thus in the $T_-(1,1)$ state and cannot transition to the S(0,2) due to Pauli Spin Blockade;
- The electron in the target dot is in spin-up state: the system can go into S(0,2) and a tunneling event is registered by the SET.

This means that, knowing a priori the state of the reference dot, detecting a tunneling event means that the target qubit was in the opposite state with respect to the ancilla one (Figure 3.13).
The Pauli Spin Blockade principle can be used also to initialize the system. As already stated in Section 3.1.3, qubits can have different Zeeman splittings, which correspond to their resonance frequencies; this is usually exploited to ensure single-qubit addressability. Therefore, after preparing the system at large detuning in the S(0,2) state, the initialization is achieved turning off the detuning, meaning that the dots become energetically aligned. In this regime, the system will go into the S(1,1), with the spin-down electron in the dot with larger E_Z and the spin-up one in the other (Figure 3.14) [39].

3.3 Driving mechanisms

3.3.1 Single-qubit control

The first step towards universal qubit control is the capability of implementing single-qubit gates. In spin-$\frac{1}{2}$ qubits, electron's spin can be manipulated through resonant microwave (MW) magnetic fields; each qubit has in fact a resonance frequency that depends on the Zeeman splitting, computed as

$$|\omega_0| = \frac{E_Z}{\hbar}. \tag{3.9}$$

Since ω_0 is also the angular frequency at which the electron rotates around the perpendicular static magnetic field B_0, this formula only computes its absolute value. The sign of the rotation is derived through the curl right hand rule; this argument will be explored in Section 4.1.1.
Single-qubit control methods thus focus on how to create a MW magnetic field with frequency ω_0. The first idea is to directly generate the magnetic field through a MW antenna near the device. This is called Electron Spin Resonance (ESR), and it is an easy and swift way to achieve spin manipulation [58]. The main issue with

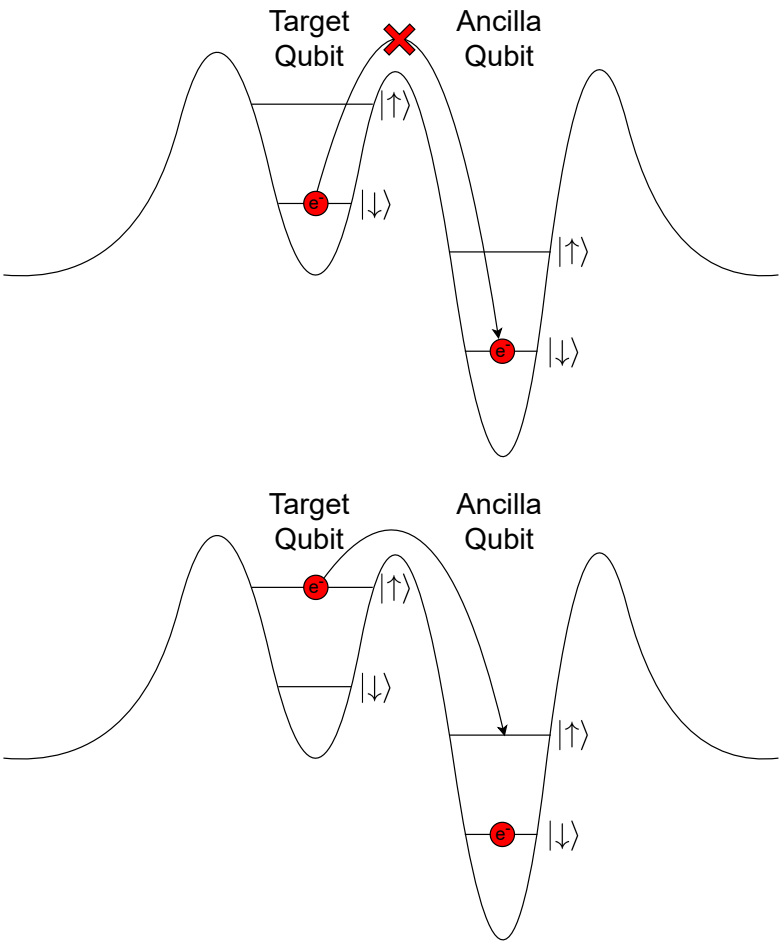

Figure 3.13: The two cases of Pauli Spin Blockade readout.

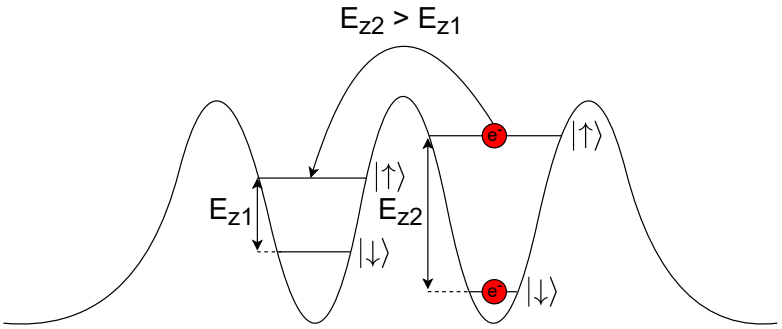

Figure 3.14: Initialization through the Pauli Spin Blockade principle.

this technique is that this type of field, since it is generated by an antenna near the device, affects all the qubits, provoking off-resonance effects in non-target qubits, which will be studied in detail in Section 4.2.3. The most immediate solution is to make the qubits' resonance frequencies very far from each other, but this cannot be obtained just by g-factor tuning. Thus this solution needs the presence of a micromagnet inside the structure in order to create a static magnetic field gradient. The Zeeman splitting indeed directly depends on the g-factor value and the local static magnetic field perceived by the spin, which, in turn, is determined by the longitudinal uniform field $\underline{B}_0$ and the transverse stray one (Figure 3.15) [50]. To make single-qubit control possible even for small values of ΔE_Z, the Electron Dipole Spin Resonance (EDSR) comes into play. This technique involves exploiting the Spin-Orbit Interaction (SOI) to couple electric field pulses to electron spins [59]. This allows one to apply MW electric fields directly through the plunger gates above the dots, avoiding interference with other qubits.

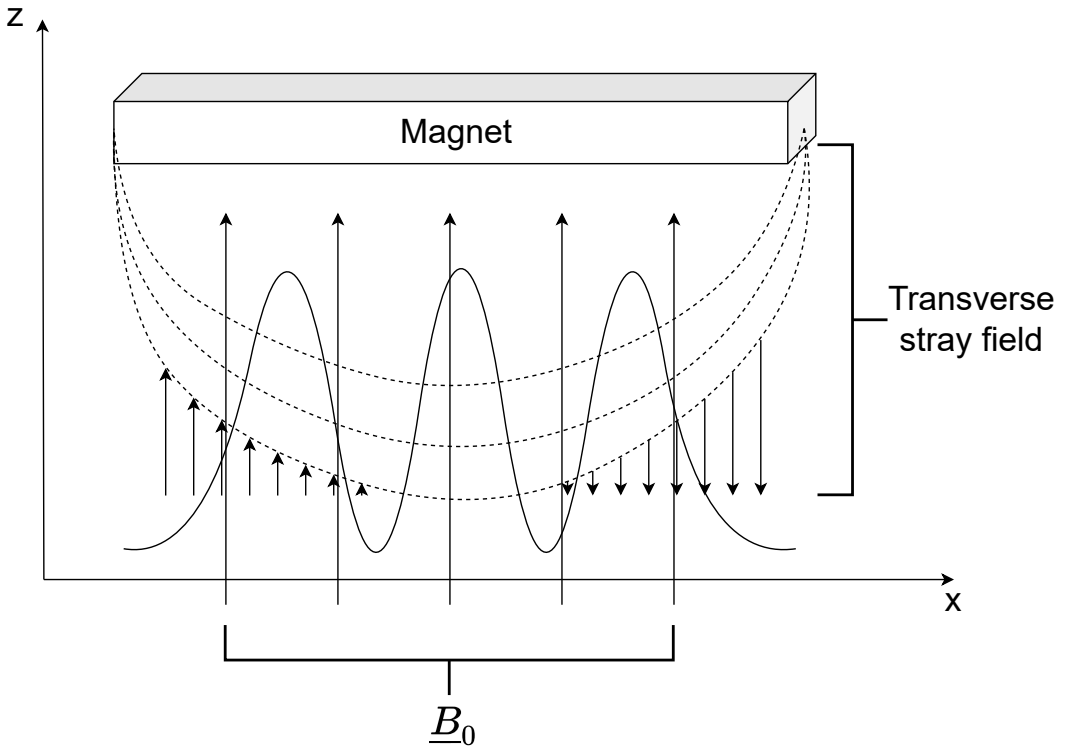

Figure 3.15: The integrated magnet creates a transverse magnetic field gradient in the DQD structure, indicated by the curved line. The solid arrows along z indicate the static magnetic field $\underline{B}_0$, while the dashed lines show the transverse stray field generated by the micromagnet. The solid arrows coming out of this field denote the magnetic field gradient along the x direction.

3.3.2 Two-qubit control

Two-qubit gates in silicon quantum dots are realized thanks to the spin-spin coupling, called *exchange interaction* J [60]. Physically, this parameter indicates how much overlap there is between the wavefunctions of electrons in different dots, and it has been demonstrated that it can be tuned through barrier gates and t_0 control [61]. Turning on this interaction between two qubits causes conditional shifts of their resonance frequencies, meaning that each qubit state depends on the other one [11]. This mechanism enables the feasibility of two-qubit gates; moreover, in this particular technology, there are two possible native gates, the $CPHASE$ and the $\sqrt{SWAP}$. This duality is ruled by the values of ΔE_Z and t_0 and will be thoroughly explored in Section 5.1.3.

Chapter 4

Single-qubit manipulation

The fourth chapter is centered on the theory behind single-qubit control of spin-$\frac{1}{2}$ qubits. The system spin Hamiltonian is defined and explained in order to carry out the time-dependent unitary evolution of the density matrix. This result is implemented in Matlab and some simulations are run to check the correctness of the device behaviour. Off-resonance effects are also explored to define the bounds in which they can be neglected.

4.1 Hamiltonian assembling

4.1.1 Computational basis definition

The first part of this analysis is the definition of the system: the encoding under study is the spin-$\frac{1}{2}$ qubit, therefore a single qubit is realized with one electron in one quantum dot. As already explained in Section 3.1.1, a static magnetic field is applied along the z direction in order to split the spin-up and spin-down states through the Zeeman effect.
The spin angular momentum operator of an electron is defined as $\underline{S}$, and its component along the z direction is [62]

$$S_z = \begin{bmatrix} \frac{\hbar}{2} & 0 \\ 0 & -\frac{\hbar}{2} \end{bmatrix} = \frac{\hbar}{2}\sigma_z \tag{4.1}$$

where σ_z is the Pauli z matrix. The matrix is diagonal, so its eigenvalues are $+\frac{\hbar}{2}$ (positive eigenvalue) and $-\frac{\hbar}{2}$ (negative eigenvalue). The associated eigenvectors are:

$$\begin{aligned} |\uparrow\rangle &= \begin{bmatrix} 1 \\ 0 \end{bmatrix} \longleftrightarrow +\frac{\hbar}{2}; \\ |\downarrow\rangle &= \begin{bmatrix} 0 \\ 1 \end{bmatrix} \longleftrightarrow -\frac{\hbar}{2}. \end{aligned} \tag{4.2}$$

These are the state vectors describing the spin-up and spin-down states, respectively.
Supposing the static magnetic field is applied along the positive z direction, it is defined as

$$\underline{B}_0 = B_0 \underline{\hat{z}}, \tag{4.3}$$

where B_0 is the magnitude of the field and $\underline{\hat{z}}$ is the versor of the z direction. The Hamiltonian for the interaction between the spin of an electron and a magnetic field is [63]

$$H_0' = -\underline{\mu} \cdot \underline{B}_0, \tag{4.4}$$

where $\underline{\mu}$ is the spin magnetic dipole moment, that can be rewritten as

$$\underline{\mu} = \gamma \underline{S} = -\frac{g\mu_B}{\hbar}\frac{\hbar}{2}\underline{\sigma}, \tag{4.5}$$

where $\gamma = -\frac{g\mu_B}{\hbar}$ is the electron gyromagnetic ratio ($[\frac{rad}{s \cdot T}]$), with g being its spin g-factor and μ_B the Bohr magneton, and $\underline{\sigma} = [\sigma_x \; \sigma_y \; \sigma_z]^t$. The Hamiltonian thus becomes

$$H_0' = -\underline{\mu} \cdot \underline{B}_0 = -\gamma \underline{S} \cdot \underline{B}_0 = -\gamma B_0 S_z = \begin{bmatrix} -\frac{\hbar}{2}\gamma B_0 & 0 \\ 0 & \frac{\hbar}{2}\gamma B_0 \end{bmatrix} = \begin{bmatrix} \frac{E_z}{2} & 0 \\ 0 & -\frac{E_z}{2} \end{bmatrix}, \tag{4.6}$$

where E_z is the Zeeman energy splitting between the spin-up and spin-down states. Therefore, its formula is

$$E_z = -\hbar\gamma B_0, \tag{4.7}$$

meaning that its sign is determined by the sign of γ. The gyromagnetic ratio is in turn equal to $-\frac{g\mu_B}{\hbar}$, hence, since μ_B and $\hbar$ are positive constants, the overall sign of E_z is determined by g. In silicon, the g-factor is almost equal to $+2$; the Zeeman splitting value is thus positive, which means that, in a silicon device, the $|\uparrow\rangle$ state is shifted of $\frac{E_z}{2}$ in the positive direction, while the $|\downarrow\rangle$ state is shifted of $\frac{E_z}{2}$ in the negative direction (Figure 4.1) [8]. In other materials, such as gallium arsenide (GaAs), the g-factor is negative [64], making $|\downarrow\rangle$ the higher energy state.
This analysis can also be seen from another perspective: the Zeeman energy splitting is related to the semi-classical Larmor precession of the electron magnetic moment around the $\underline{B}_0$ field [62]. This precession happens with a precise angular frequency, defined as

$$\underline{\omega}_0 = -\gamma \underline{B}_0, \tag{4.8}$$

which means that the rotation happens around the direction of the field, and its sign is determined by γ. In silicon, γ is negative, therefore the precession is a positive rotation around the field, following the curl right hand rule (Figure 4.2). The magnitude of this angular frequency is

$$|\underline{\omega}_0| = \omega_0 = |\gamma| B_0, \tag{4.9}$$

which, since $\gamma < 0$, becomes

$$\omega_0 = -\gamma B_0 = \frac{E_z}{\hbar}. \tag{4.10}$$

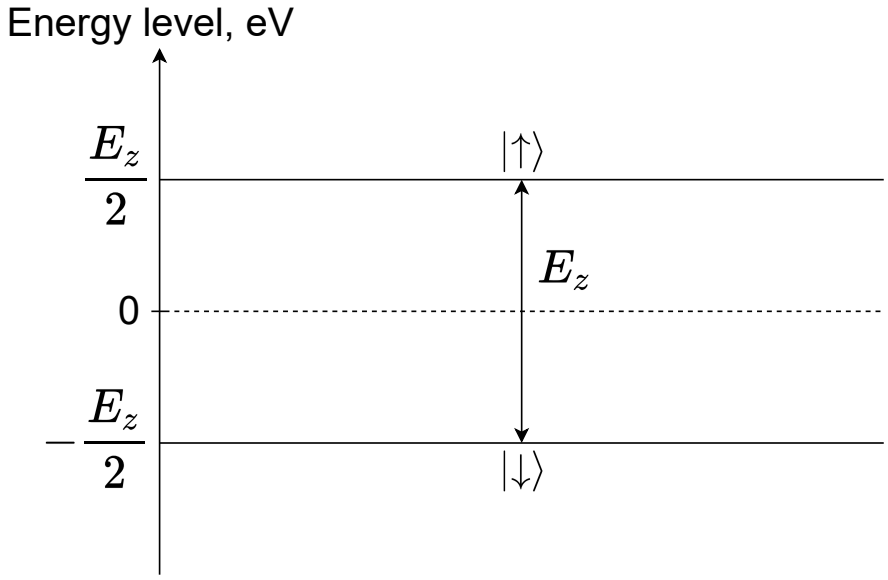

Figure 4.1: Energy diagram of a spin-$\frac{1}{2}$ qubit. The Zeeman effect splits the spin-up and spin-down states.

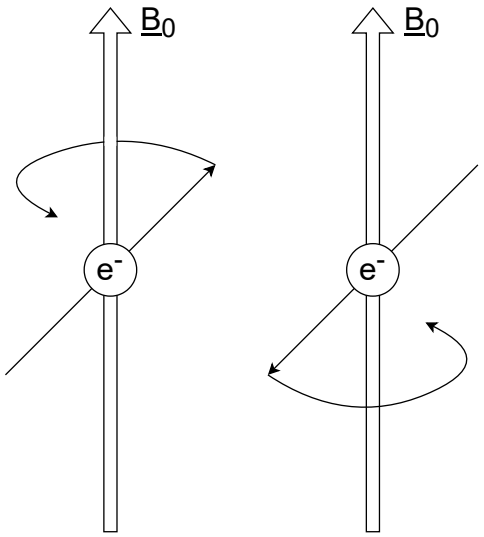

Figure 4.2: Larmor precession of an electron around $\underline{B}_0$.

The computational basis is thus $\{|\uparrow\rangle, |\downarrow\rangle\}$, and, since the $|0\rangle$ state is assigned to the lowest energy level, the Hamiltonian is written in the $\{|1\rangle, |0\rangle\}$ basis, which, unfortunately, is the opposite of the standard quantum computing basis. In fact, for historical reasons, the usual basis is $\{|0\rangle, |1\rangle\}$, which comes from another quantum computing technology, the Nuclear Magnetic Resonance (NMR), whose ground state is $|\uparrow\rangle$ [65]. Therefore, the NMR basis is still $\{|\uparrow\rangle, |\downarrow\rangle\}$, but it is now directly mapped to the $\{|0\rangle, |1\rangle\}$ basis. Hence, in order to make the model compatible to the usual standards, a change of basis through a unitary matrix U_C is needed. The system spin Hamiltonian in the $\{|\downarrow\rangle, |\uparrow\rangle\}$ basis is

$$H_0 = U_C H_0' U_C^\dagger = \sigma_x H_0' \sigma_x^\dagger = \begin{bmatrix} 0 & 1 \\ 1 & 0 \end{bmatrix} \begin{bmatrix} \frac{E_z}{2} & 0 \\ 0 & -\frac{E_z}{2} \end{bmatrix} \begin{bmatrix} 0 & 1 \\ 1 & 0 \end{bmatrix} = \begin{bmatrix} -\frac{E_z}{2} & 0 \\ 0 & \frac{E_z}{2} \end{bmatrix}. \tag{4.11}$$

After this change of basis, the spin rotates around $\underline{B}_0$ in the opposite way with respect to Figure 4.2, i.e the same verse as in NMR.

4.1.2 Applying a MW magnetic field

The single-qubit manipulation is achieved through the application of a microwave (MW) resonant magnetic field [58]. This field can be written as

$$\underline{B}_1 = 2B_1 \cos(\omega_{MW} t - \phi_1)\underline{\hat{x}}, \tag{4.12}$$

where B_1 is the magnitude of the MW field, ω_{MW} is the microwave frequency, ϕ_1 the phase of the field and $\underline{\hat{x}}$ is the versor of the x direction, which indicates that this field is applied along the positive x direction. The overall magnetic field becomes

$$\underline{B} = \underline{B}_0 + \underline{B}_1 = B_0\underline{\hat{z}} + 2B_1 \cos(\omega_{MW} t - \phi_1)\underline{\hat{x}}, \tag{4.13}$$

and the resulting Hamiltonian is

$$H'_{MW} = -\underline{\mu} \cdot \underline{B} = -\underline{\mu} \cdot \underline{B}_0 - \underline{\mu} \cdot \underline{B}_1 = H_0' + H_1', \tag{4.14}$$

where

$$\begin{aligned} H_0' &= \begin{bmatrix} \frac{E_z}{2} & 0 \\ 0 & -\frac{E_z}{2} \end{bmatrix}, \\ H_1' &= \begin{bmatrix} 0 & -\frac{\hbar}{2}\gamma 2B_1 \cos(\omega_{MW} t - \phi_1) \\ -\frac{\hbar}{2}\gamma 2B_1 \cos(\omega_{MW} t - \phi_1) & 0 \end{bmatrix} \end{aligned} \tag{4.15}$$

are the two parts (static and MW) of the system Hamiltonian in the $\{|\uparrow\rangle, |\downarrow\rangle\}$ basis. As explained in Section 4.1.1, one needs to change the Hamiltonian basis through the transformation used in Equation (4.11). The result for H_1 is

$$\begin{aligned} H_1 &= U_C H_1' U_C^\dagger = \sigma_x H_1' \sigma_x^\dagger \\ &= \begin{bmatrix} 0 & 1 \\ 1 & 0 \end{bmatrix} \begin{bmatrix} 0 & -\frac{\hbar}{2}\gamma 2B_1 \cos(\omega_{MW} t - \phi_1) \\ -\frac{\hbar}{2}\gamma 2B_1 \cos(\omega_{MW} t - \phi_1) & 0 \end{bmatrix} \begin{bmatrix} 0 & 1 \\ 1 & 0 \end{bmatrix} \\ &= \begin{bmatrix} 0 & -\frac{\hbar}{2}\gamma 2B_1 \cos(\omega_{MW} t - \phi_1) \\ -\frac{\hbar}{2}\gamma 2B_1 \cos(\omega_{MW} t - \phi_1) & 0 \end{bmatrix}. \end{aligned} \tag{4.16}$$

Note that H_1' is not affected by the transformation as it is already written through σ_x. Therefore, the full MW Hamiltonian in the $\{|\downarrow\rangle, |\uparrow\rangle\}$ basis is

$$H_{MW} = H_0 + H_1 = \begin{bmatrix} -\frac{E_z}{2} & -\frac{\hbar}{2}\gamma 2B_1 \cos(\omega_{MW}t - \phi_1) \\ -\frac{\hbar}{2}\gamma 2B_1 \cos(\omega_{MW}t - \phi_1) & \frac{E_z}{2} \end{bmatrix}. \quad (4.17)$$

Thanks to Euler's formulas, the MW field can be rewritten as

$$2B_1 \cos(\omega_{MW}t - \phi_1)\hat{\underline{x}} = B_1 \left(e^{j\omega_{MW}t}e^{-j\phi_1} + e^{-j\omega_{MW}t}e^{j\phi_1}\right)\hat{\underline{x}}; \quad (4.18)$$

hence, the Hamiltonian becomes

$$H_{MW} = \frac{\hbar}{2}\begin{bmatrix} -\omega_0 & -\gamma B_1 \eta \\ -\gamma B_1 \eta & \omega_0 \end{bmatrix}, \quad (4.19)$$

where $\eta = \left(e^{j\omega_{MW}t}e^{-j\phi_1} + e^{-j\omega_{MW}t}e^{j\phi_1}\right)$.
This arises a serious concern in terms of computing the system's time-dependent unitary evolution from the Hamiltonian, as it now depends on time. Indeed, supposing the initial time instant $t_0 = 0$, the formal general solution of the Schrödinger equation is [62, 15]

$$U(t) = \mathcal{T} \exp\left(-\frac{j}{\hbar}\int_0^t H(t')dt'\right), \quad (4.20)$$

where $\mathcal{T}$ is the time-ordered product. On the other hand, when the Hamiltonian is time independent, the solution reduces to

$$U(t) = \exp\left(-\frac{j}{\hbar}Ht\right). \quad (4.21)$$

The time dependence of the Hamiltonian in Equation (4.19) is solved analysing the system in a *rotating frame*. The action of going into a rotating frame translates to a transformation of the Hamiltonian [66]. The idea behind this transformation is that in the original basis, the *laboratory frame*, the state vector rotates around the z axis with angular frequency ω_0; therefore, if the system rotates in the same direction and at the same angular frequency, the state vector will be stationary. This is intuitively explained using a Bloch sphere representation and supposing a $R_X\left(\frac{\pi}{2}\right)$ is applied to the $|0\rangle$ state: the lab frame shows precessions around the z axis while the vector rotates around the x direction due to the R_X gate, while, in the rotating frame, only the latter is present (Figure 4.3).

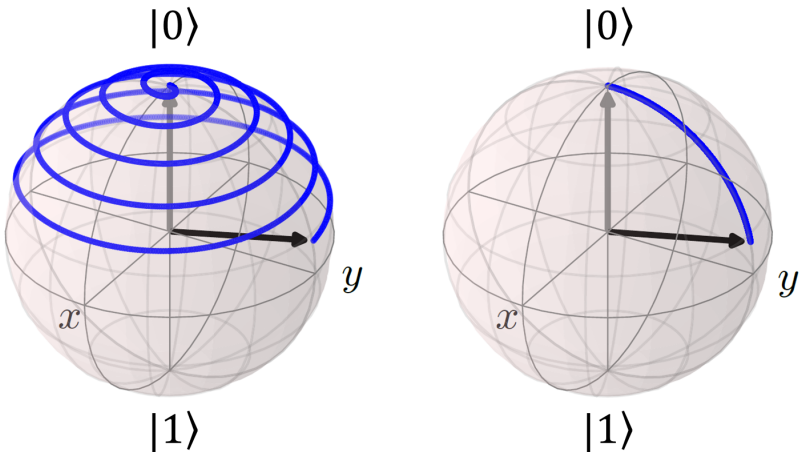

Figure 4.3: The lab frame (on the left) depicts the vector rotating around both x and z axes, while the rotating frame (on the right) illustrates the merit of this transformation. Adapted from [66].

The rotating frame transformation is carried out as [67]

$$\tilde{H}_{MW} = U_{RF} H_{MW} U_{RF}^{\dagger} - j\hbar U_{RF} \frac{dU_{RF}^{\dagger}}{dt}, \tag{4.22}$$

where U_{RF} is the rotating frame unitary matrix, defined as

$$U_{RF} = \begin{bmatrix} e^{-j\frac{\omega_{RF}}{2}t} & 0 \\ 0 & e^{j\frac{\omega_{RF}}{2}t} \end{bmatrix}, \tag{4.23}$$

with ω_{RF} angular frequency of the rotating frame (arbitrary, for now).
For the sake of simplicity, the two terms of Equation (4.22) will be computed separately; the latter yields

$$\begin{aligned} j\hbar U_{RF} \frac{dU_{RF}^{\dagger}}{dt} &= j\hbar \begin{bmatrix} e^{-j\frac{\omega_{RF}}{2}t} & 0 \\ 0 & e^{j\frac{\omega_{RF}}{2}t} \end{bmatrix} \begin{bmatrix} j\frac{\omega_{RF}}{2} e^{j\frac{\omega_{RF}}{2}t} & 0 \\ 0 & -j\frac{\omega_{RF}}{2} e^{-j\frac{\omega_{RF}}{2}t} \end{bmatrix} \\ &= \frac{\hbar}{2} \begin{bmatrix} -\omega_{RF} & 0 \\ 0 & \omega_{RF} \end{bmatrix}, \end{aligned} \tag{4.24}$$

while the first term is computed as

$$\begin{aligned} U_{RF} H_{MW} U_{RF}^{\dagger} &= \begin{bmatrix} e^{-j\frac{\omega_{RF}}{2}t} & 0 \\ 0 & e^{j\frac{\omega_{RF}}{2}t} \end{bmatrix} \frac{\hbar}{2} \begin{bmatrix} -\omega_0 & -\gamma B_1 \eta \\ -\gamma B_1 \eta & \omega_0 \end{bmatrix} \begin{bmatrix} e^{j\frac{\omega_{RF}}{2}t} & 0 \\ 0 & e^{-j\frac{\omega_{RF}}{2}t} \end{bmatrix} \\ &= \begin{bmatrix} e^{-j\frac{\omega_{RF}}{2}t} & 0 \\ 0 & e^{j\frac{\omega_{RF}}{2}t} \end{bmatrix} \frac{\hbar}{2} \begin{bmatrix} -\omega_0 e^{j\frac{\omega_{RF}}{2}t} & -\gamma B_1 \eta e^{-j\frac{\omega_{RF}}{2}t} \\ -\gamma B_1 \eta e^{j\frac{\omega_{RF}}{2}t} & \omega_0 e^{-j\frac{\omega_{RF}}{2}t} \end{bmatrix} \\ &= \frac{\hbar}{2} \begin{bmatrix} -\omega_0 & -\gamma B_1 \eta e^{-j\omega_{RF}t} \\ -\gamma B_1 \eta e^{j\omega_{RF}t} & \omega_0 \end{bmatrix}. \end{aligned} \tag{4.25}$$

The Hamiltonian in the rotating frame is thus

$$\begin{aligned}\tilde{H}_{MW} &= U_{RF} H_{MW} U_{RF}^{\dagger} - j\hbar U_{RF} \frac{dU_{RF}^{\dagger}}{dt} \\ &= \frac{\hbar}{2} \begin{bmatrix} -\omega_0 + \omega_{RF} & -\gamma B_1 \eta e^{-j\omega_{RF} t} \\ -\gamma B_1 \eta e^{j\omega_{RF} t} & \omega_0 - \omega_{RF} \end{bmatrix} \\ &= \frac{\hbar}{2} \begin{bmatrix} -\omega_0 + \omega_{RF} & \\ -\gamma B_1 \left(e^{j(\omega_{MW}+\omega_{RF})t} e^{-j\phi_1} + e^{-j(\omega_{MW}-\omega_{RF})t} e^{j\phi_1} \right) & \\ & -\gamma B_1 \left(e^{j(\omega_{MW}-\omega_{RF})t} e^{-j\phi_1} + e^{-j(\omega_{MW}+\omega_{RF})t} e^{j\phi_1} \right) \\ & \omega_0 - \omega_{RF} \end{bmatrix}.\end{aligned} \tag{4.26}$$

4.1.3 The Rotating Wave Approximation

The next step towards the computation of the time-dependent unitary evolution is the use of the Rotating Wave Approximation (RWA). Equation (4.26) shows the contribution of two exponentials in the (1,2) and (2,1) positions: one has the sum of ω_{MW} and ω_{RF}, while the other has the difference between them. As explained below, gates are implemented enforcing $\omega_{RF} \approx \omega_{MW} \approx \omega_0$, meaning that $\omega_{MW} + \omega_{RF} \approx 2\omega_0$. The theoretical explanation of this behaviour is that the MW field can be divided in two components: one rotating in the same direction of the frame ($\underline{B}_1^+$) and one in the opposite way ($\underline{B}_1^-$):

$$\begin{aligned}\underline{B}_1^+ &= B_1 \left(\cos(\omega_{MW} t - \phi_1) \hat{\underline{x}} - \sin(\omega_{MW} t - \phi_1) \hat{\underline{y}} \right); \\ \underline{B}_1^- &= B_1 \left(\cos(\omega_{MW} t - \phi_1) \hat{\underline{x}} + \sin(\omega_{MW} t - \phi_1) \hat{\underline{y}} \right).\end{aligned} \tag{4.27}$$

Hence, the terms that contain the sum of the two frequencies, i.e. the ones related to the $\underline{B}_1^-$ component that rotates against the frame, where the exponential varies at a much faster rate, can be neglected [68, 69]. Therefore, the spin only rotates around one field component, namely $\underline{B}_1^+$. This precession happens with a precise angular frequency, called *Rabi frequency*, defined as

$$\omega_1 = -\gamma B_1. \tag{4.28}$$

Similarly to ω_0, this frequency depends on the γ sign: supposing $\phi_1 = 0$, i.e. the field is oriented along the x direction, the rotation is positive around it (Figure 4.4). After the RWA, the Hamiltonian becomes

$$\tilde{H}_{MW,RWA} = \frac{\hbar}{2} \begin{bmatrix} -\omega_0 + \omega_{RF} & \omega_1 e^{j(\omega_{MW}-\omega_{RF})t} e^{-j\phi_1} \\ \omega_1 e^{-j(\omega_{MW}-\omega_{RF})t} e^{j\phi_1} & \omega_0 - \omega_{RF} \end{bmatrix}. \tag{4.29}$$

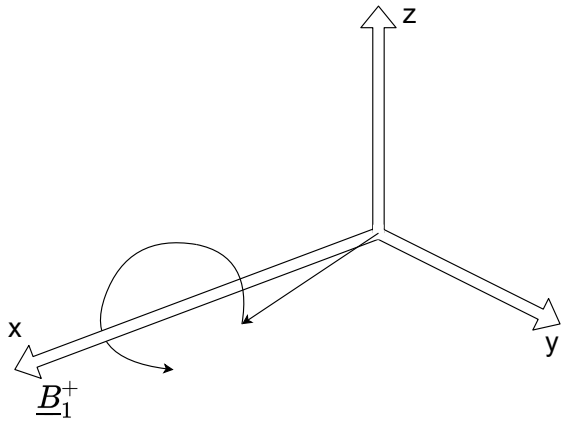

Figure 4.4: Larmor precession around $\underline{B}_1^+$ for $\phi_1 = 0$.

Then, supposing that the rotating frame angular frequency ω_{RF} matches the qubit resonance frequency ω_0, Equation (4.29) yields

$$\tilde{H}_{MW,RWA} = \frac{\hbar}{2}\begin{bmatrix} 0 & \omega_1 e^{j\Delta\omega t} e^{-j\phi_1} \\ \omega_1 e^{-j\Delta\omega t} e^{j\phi_1} & 0 \end{bmatrix}, \tag{4.30}$$

where $\Delta\omega = \omega_{MW} - \omega_0$ is the frequency difference between the MW frequency and the qubit resonance frequency. The last step towards the elimination of time dependencies in the Hamiltonian is to assume that the MW field is in resonance with the qubit, i.e. $\omega_{MW} = \omega_0$. Then,

$$\tilde{H}_{MW,RWA} = \frac{\hbar}{2}\begin{bmatrix} 0 & \omega_1 e^{-j\phi_1} \\ \omega_1 e^{j\phi_1} & 0 \end{bmatrix}, \tag{4.31}$$

which shows that the Hamiltonian is now time-independent and thus the system unitary evolution can be easily computed through Equation (4.21), which yields

$$U(t) = \exp\left(-\frac{j}{\hbar}\tilde{H}_{MW,RWA}t\right), \tag{4.32}$$

where t is the duration of the MW pulse.
Matrix exponentials are usually hard to calculate and computationally heavy, but, in this particular case, the Hamiltonian can be rewritten through decomposition in Pauli matrices, whose general exponential formula is [70]

$$e^{j\alpha\underline{\hat{n}}\cdot\underline{\sigma}} = \cos\alpha \cdot \mathbb{I} + j(\underline{\hat{n}} \cdot \underline{\sigma})\sin\alpha, \tag{4.33}$$

where $\underline{\hat{n}}$ is an arbitrary unit vector in $\mathbb{R}^3$. Therefore, the Hamiltonian needs to be decomposed in Pauli matrices:

$$\tilde{H}_{MW,RWA} = \frac{\hbar}{2}\begin{bmatrix} 0 & \omega_1 e^{-j\phi_1} \\ \omega_1 e^{j\phi_1} & 0 \end{bmatrix} = \frac{\hbar}{2}(\omega_1 \cos\phi_1 \sigma_x + \omega_1 \sin\phi_1 \sigma_y). \tag{4.34}$$

Equation (4.33) is now applicable and the unitary evolution can be computed as

$$U(t) = \exp\left(-j\frac{\omega_1 t}{2}(\cos\phi_1\sigma_x + \sin\phi_1\sigma_y)\right) = \exp\left(-j\frac{\omega_1 t}{2}\hat{\underline{n}}\cdot\underline{\sigma}\right), \tag{4.35}$$

with $\hat{\underline{n}} = \cos\phi_1\,\hat{\underline{x}} + \sin\phi_1\,\hat{\underline{y}}$. Hence,

$$\begin{aligned} U(t) &= \cos\frac{\omega_1 t}{2}\cdot\mathbb{I} - j\sin\frac{\omega_1 t}{2}(\hat{\underline{n}}\cdot\underline{\sigma}) \\ &= \begin{bmatrix}\cos\frac{\omega_1 t}{2} & 0\\ 0 & \cos\frac{\omega_1 t}{2}\end{bmatrix} + \begin{bmatrix}0 & -j\sin\frac{\omega_1 t}{2}\cos\phi_1\\ -j\sin\frac{\omega_1 t}{2}\cos\phi_1 & 0\end{bmatrix} + \\ &\qquad + \begin{bmatrix}0 & -\sin\frac{\omega_1 t}{2}\sin\phi_1\\ \sin\frac{\omega_1 t}{2}\sin\phi_1 & 0\end{bmatrix}, \end{aligned} \tag{4.36}$$

which finally yields

$$U(t) = \begin{bmatrix}\cos\frac{\omega_1 t}{2} & -j\sin\frac{\omega_1 t}{2}e^{-j\phi_1}\\ -j\sin\frac{\omega_1 t}{2}e^{j\phi_1} & \cos\frac{\omega_1 t}{2}\end{bmatrix}, \tag{4.37}$$

that is the final formula for $U(t)$, the unitary matrix that describes the time evolution of a single qubit when it is subjected to a resonant MW magnetic field.

4.2 MATLAB implementation and results

4.2.1 The compact MATLAB model structure

The MATLAB model mainly revolves around the computation of $U(t)$ using Equation (4.37). The first step is the definition of fundamental system parameters, which are set by the user in separate input files. These user-defined inputs can be divided in two classes:

- Physical parameters:
  - *n_qubit*, the number of quantum dots;
  - *gfactor*, the g-factor of each dot;
  - *B_0*, the static magnetic field along z.
- Control parameters:
  - *B_1*, the MW magnetic field amplitude;
  - *phi_1*, the phase of the MW field.

The first implementation of this model, which only carries out a *Rabi flopping* simulation, i.e. a $R_X(\theta)$ gate applied to the $|0\rangle$ state, includes three input files:

- *SetConstants.m*, which provides useful computational constants, such as $\hbar$, m and q;
- *SetParameters.m*, where the physical parameters are stored;
- *SetInput.m*, in which the user can set the control parameters.

The unitary matrix $U(t)$ is computed in the *single_qubit.m* file, while the whole code is run by a main file named *Qubit.m* (Figure 4.5).

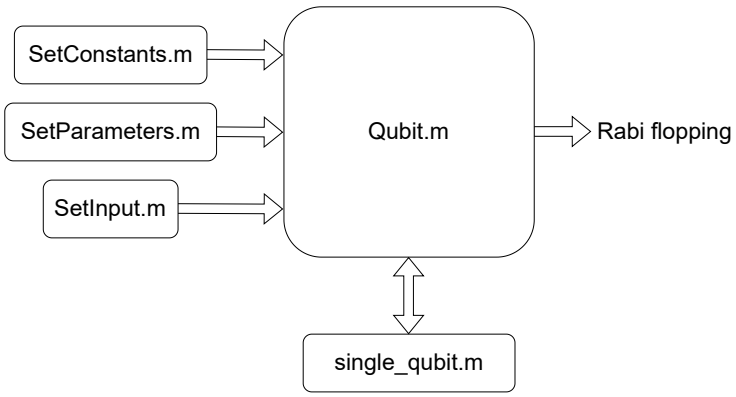

Figure 4.5: MATLAB code structure for the Rabi flopping simulation.

4.2.2 Rabi flopping simulation

As mentioned in the previous section, the Rabi flopping is the simulation of a $R_X(\theta)$ gate applied to the $|0\rangle$ state. All the system and control values are taken from [11]: $g = 1.9860$ and $B_0 = 0.25$ T, which yield $\omega_0 = 43.663$ Grad/s, i.e. $f_0 = 6.9491$ GHz. The angle of rotation θ is equal to $\omega_1 t$, therefore ω_1 is set to be 6.2832 Mrad/s ($f_1 = 1$ MHz), which is achieved through a B_1 of ~ 36 µT, and t is equal to 8 µs to see 8 periods of rotations around the x axis. Since the revolving must be around the x axis, ϕ_1 is set to 0, in order to orientate the $\underline{B}_1$ field in that direction.
The system state is plotted in the Bloch sphere for $t = 0$ (Figure 4.6a) s and $t = 0.5$ µs (Figure 4.6b)- this is half the rotation period, so that the system is in the opposite state - and the probability of the state $|1\rangle$ ($|\downarrow\rangle$) is measured for the whole 8 µs interval (Figure 4.7).

After performing the Rabi flopping experiment, the model is enhanced with some additional files, containing preset values of ϕ_1 and t for the realization of $R_X(\theta)$ (such as in the Rabi flopping), $R_Y(\theta)$, $R_Z(\theta)$ and H (Hadamard) gates. The Rabi frequency ω_1 is always set to 6.2832 Mrad/s ($f_1 = 1$ MHz).

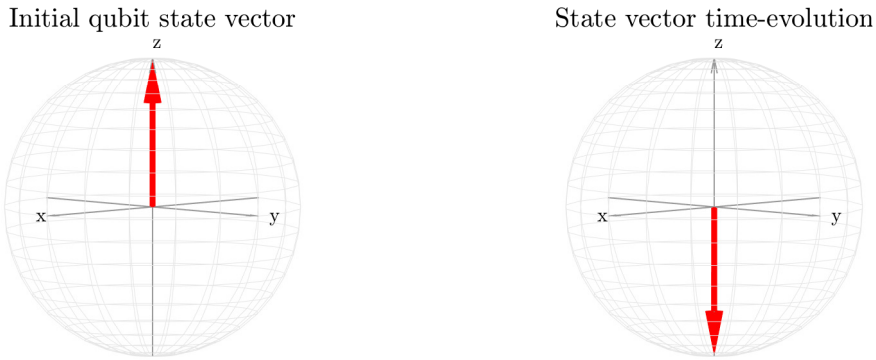

(a) Initial state, $t = 0$ s. (b) Final state after $t = 0.5$ µs.

Figure 4.6: Initial (a) and final state (b) after the Rabi flopping. Since the rotation frequency is set to 1 MHz, the rotation from $|0\rangle$ to $|1\rangle$ happens after 0.5 µs.

The angle of rotation θ is automatically set by the code, which takes θ as an input and computes the time duration of the pulse needed to achieve that angle as $t = \frac{\theta}{\omega_1}$. Instead ϕ_1 is fixed in the *SetInputRX.m* and *SetInputRY.m* files: in the former

$$\phi_1 = \begin{cases} 0 & \text{for} \quad \theta > 0 \\ \pi & \text{for} \quad \theta < 0 \end{cases}, \tag{4.38}$$

while in the latter

$$\phi_1 = \begin{cases} \frac{\pi}{2} & \text{for} \quad \theta > 0 \\ -\frac{\pi}{2} & \text{for} \quad \theta < 0 \end{cases}. \tag{4.39}$$

The $R_Z(\theta)$ gate is implemented in two ways, depending on the possibility of implementing *virtual* Z gates [71, 72]:

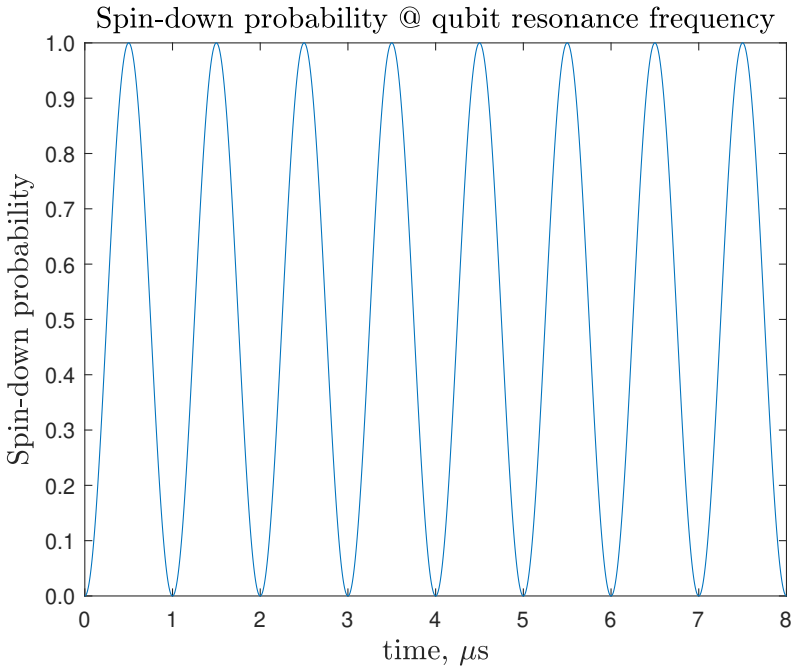

Figure 4.7: Variation of the probability of the state $|1\rangle$ with respect to the duration of the MW pulse. The periodic rotation of the qubit state around the x axis can be observed, effectively realizing a $R_X(\theta)$ gate, where θ can be tuned through the duration of the MW pulse t.

- Virtual Z feasible: the gate can be implemented by taking into account a phase contribution, using its ideal unitary matrix

$$U_{R_Z} = \begin{bmatrix} e^{-j\frac{\theta}{2}} & 0 \\ 0 & e^{j\frac{\theta}{2}} \end{bmatrix}; \tag{4.40}$$

- Virtual Z not feasible: the gate is realized using the R_X and R_Y gates, since

$$R_Z(\theta) = R_X(\frac{\pi}{2})R_Y(\theta)R_X(-\frac{\pi}{2}). \tag{4.41}$$

This choice can be made by the user through a dedicated flag in the code. The H gate follows the same route, since there are two possible decomposition: one involving a R_Z gate and the other using only R_X and R_Y gates. Therefore:

- Virtual Z feasible: since it only adds a phase contribution, the R_Z gate is computationally convenient, so

$$H = R_Z(\pi)R_Y(-\frac{\pi}{2}); \tag{4.42}$$

- Virtual Z not feasible: only R_X and R_Y gates are available:

$$H = R_X(\pi)R_Y(\frac{\pi}{2}). \tag{4.43}$$

4.2.3 Off-resonance effects

In the previous computation and MATLAB simulations, the MW field was assumed to be in resonance with the qubit, i.e. $\omega_{MW} = \omega_0$. This condition is indeed always verified when performing single qubit manipulations, but off-resonance effects may arise due to the fact that there are other qubits with different resonance frequencies in the device. In fact, the MW field generally expands throughout all the structure, therefore every qubit is affected by a certain time-evolution. However, the field is resonant only with the target qubit, while other qubits, that generally have different resonance frequencies, perceive an off-resonance field. This effect is more evident when the resonance frequencies are very close to each other.
In order to study off-resonance behaviours, one needs to start from Equation (4.29) and assume $\omega_{RF} = \omega_{MW}$. This yields

$$\tilde{H}_{MW,RWA} = \frac{\hbar}{2}\begin{bmatrix} -\omega_0 + \omega_{MW} & \omega_1 e^{-j\phi_1} \\ \omega_1 e^{j\phi_1} & \omega_0 - \omega_{MW} \end{bmatrix} = \frac{\hbar}{2}\begin{bmatrix} \Delta\omega & \omega_1 e^{-j\phi_1} \\ \omega_1 e^{j\phi_1} & -\Delta\omega \end{bmatrix}. \tag{4.44}$$

Since the time dependencies have been already eliminated, the next step is the Pauli matrices decomposition:

$$\begin{aligned} \tilde{H}_{MW,RWA} &= \frac{\hbar}{2}\begin{bmatrix} \Delta\omega & \omega_1 e^{-j\phi_1} \\ \omega_1 e^{j\phi_1} & -\Delta\omega \end{bmatrix} \\ &= \frac{\hbar}{2}(\Delta\omega\sigma_z + \omega_1 \cos\phi_1 \sigma_x + \omega_1 \sin\phi_1 \sigma_y) \\ &= \frac{\hbar}{2}\Omega\left(\frac{\Delta\omega}{\Omega}\sigma_z + \frac{\omega_1}{\Omega}\cos\phi_1\sigma_x + \frac{\omega_1}{\Omega}\sin\phi_1\sigma_y\right) \\ &= \frac{\hbar}{2}\Omega\,(\hat{\underline{n}} \cdot \underline{\sigma}), \end{aligned} \tag{4.45}$$

where $\Omega = \sqrt{\Delta\omega^2 + \omega_1^2}$ is the *generalized Rabi frequency*, needed in the computation in order to normalize $\hat{\underline{n}}$, making it a unit vector. However, Ω is indeed a generalization of ω_1 to the off-resonance case: in fact $\Omega = \omega_1$ for $\Delta\omega = 0$.
The unitary evolution is thus

$$\begin{aligned} U(t) &= \exp\left(-j\frac{\Omega t}{2}\left(\frac{\Delta\omega}{\Omega}\sigma_z + \frac{\omega_1}{\Omega}\cos\phi_1\sigma_x + \frac{\omega_1}{\Omega}\sin\phi_1\sigma_y\right)\right) \\ &= \exp\left(-j\frac{\Omega t}{2}\hat{\underline{n}} \cdot \underline{\sigma}\right), \end{aligned} \tag{4.46}$$

with $\hat{\underline{n}} = \frac{\Delta\omega}{\Omega}\hat{\underline{z}} + \frac{\omega_1}{\Omega}\cos\phi_1\hat{\underline{x}} + \frac{\omega_1}{\Omega}\sin\phi_1\hat{\underline{y}}$.
Then, Equation (4.33) yields

$$\begin{aligned} U(t) &= \cos\frac{\Omega t}{2}\cdot\mathbb{I} - j\sin\frac{\Omega t}{2}(\hat{\underline{n}}\cdot\underline{\sigma}) \\ &= \begin{bmatrix}\cos\frac{\Omega t}{2} & 0\\ 0 & \cos\frac{\Omega t}{2}\end{bmatrix} + \begin{bmatrix}-j\frac{\Delta\omega}{\Omega}\sin\frac{\Omega t}{2} & 0\\ 0 & j\frac{\Delta\omega}{\Omega}\sin\frac{\Omega t}{2}\end{bmatrix} + \\ &\quad + \begin{bmatrix}0 & -j\sin\frac{\Omega t}{2}\cdot\frac{\omega_1}{\Omega}\cos\phi_1\\ -j\sin\frac{\Omega t}{2}\cdot\frac{\omega_1}{\Omega}\cos\phi_1 & 0\end{bmatrix} + \\ &\quad + \begin{bmatrix}0 & -\sin\frac{\Omega t}{2}\cdot\frac{\omega_1}{\Omega}\sin\phi_1\\ \sin\frac{\Omega t}{2}\cdot\frac{\omega_1}{\Omega}\sin\phi_1 & 0\end{bmatrix}, \end{aligned} \tag{4.47}$$

which gives

$$U(t) = \begin{bmatrix}\cos\frac{\Omega t}{2} - j\frac{\Delta\omega}{\Omega}\sin\frac{\Omega t}{2} & -j\sin\frac{\Omega t}{2}\cdot\frac{\omega_1}{\Omega}e^{-j\phi_1}\\ -j\sin\frac{\Omega t}{2}\cdot\frac{\omega_1}{\Omega}e^{j\phi_1} & \cos\frac{\Omega t}{2} + j\frac{\Delta\omega}{\Omega}\sin\frac{\Omega t}{2}\end{bmatrix}. \tag{4.48}$$

This is a more general version of Equation (4.37); implementing it in *single_qubit.m* makes the model capable of computing the system evolution in off-resonance conditions. The Rabi flopping simulation is indeed repeated, using the same parameters of the previous analysis, but employing a vector of ω_{MW}. This makes the model repeat the same simulation for different values of ω_{MW}, centered in ω_0 (43.663 Grad/s, as before) with a span of 100 Mrad/s. The result of this simulation is the *Chevron pattern* (Figure 4.8), i.e. the plot of the spin-down probability with respect to the MW pulse duration and to the MW field angular frequency ω_{MW}. It is important to note that if one performs a cut parallel to the time axis at the resonant MW frequency ($\omega_{MW} = \omega_0$), the result is exactly the spin-down probability plot of the previous simulation (Figure 4.7), which, in fact, was a resonant analysis.
If, instead, the cut is made parallel to the ω_{MW} axis, at $t = 0.5$ µs (time for which the system is in the $|\downarrow\rangle$ state), the plot shows the off-resonance effects: the closer the qubit resonance frequency is to ω_0, the stronger are the effects of the MW field on it (Figure 4.9).

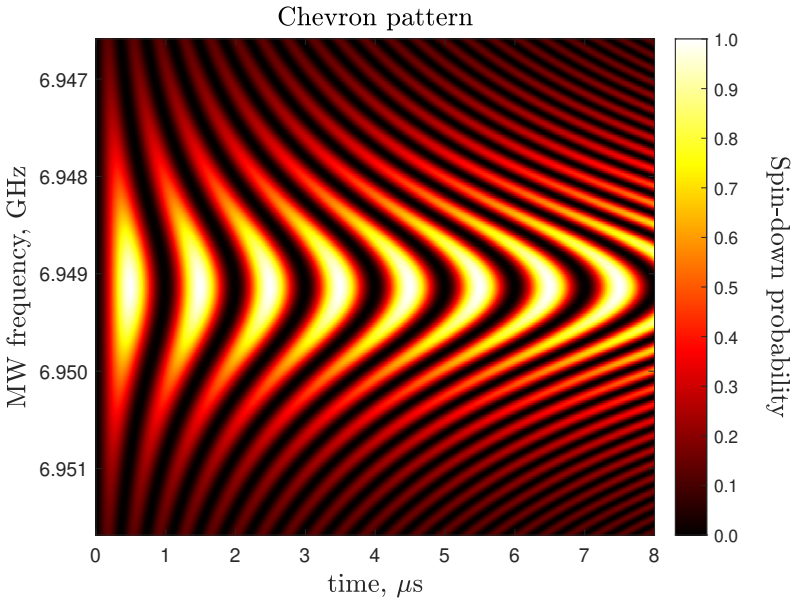

Figure 4.8: Variation of the probability of the state $|1\rangle$ with respect to the duration of the MW pulse and its angular frequency.

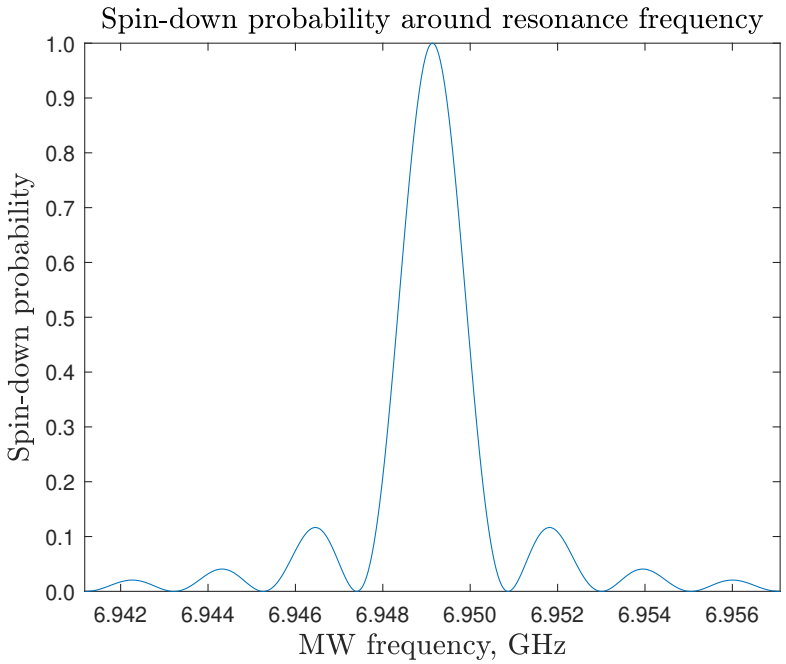

Figure 4.9: Spin-down probability with respect to the MW field angular frequency. Off-resonance effects are stronger in the vicinity of the center of the plot (ω_0), while they get weaker as ω_{MW} becomes different from the qubit resonance frequency.

Chapter 5

Two-qubit manipulation

The next step towards universal qubit manipulation is the two-qubit control. This chapter describes the theoretical derivation of the DQD spin Hamiltonian, with particular attention on the approximations used to derive a time-independent matrix. The native gate duality is then explored, focusing on how to implement the two different gates. Finally, the MATLAB model approximations are verified using QuTiP [73], a numerical simulator for quantum systems on Python.

5.1 Double quantum dot Hamiltonian

5.1.1 The Hubbard model

The two-qubit gates analysis is carried out on a double quantum dot system, which is a many-body system and has a more complex Hamiltonian with respect to the single-qubit case. The operating regime of the structure are the (1,1) states but, as already studied in Section 3.1.3, the S(0,2) and S(2,0) states are strictly coupled and must be included in the spin Hamiltonian. In this study, the notation will be that the left quantum dot is the qubit q_1, while the right one is q_0, following the IBM standard where a ket vector describing a two-qubit state is ordered from the MSB to the LSB, i.e. $|q_1\, q_0\rangle$ [74].
The starting point of this analysis is the *Hubbard model* [75, 76, 77, 78], which describes the interaction between the two quantum dots taking into account tunnel coupling and the Coulomb charging energy of the dots. The natural basis of a single-qubit system, explored in Section 4.1.1, is $\{|\uparrow\rangle, |\downarrow\rangle\}$, therefore, in a two-qubit structure, the basis becomes $\{|\uparrow\rangle, |\downarrow\rangle\} \otimes \{|\uparrow\rangle, |\downarrow\rangle\} = \{|\uparrow\uparrow\rangle, |\uparrow\downarrow\rangle, |\downarrow\uparrow\rangle, |\downarrow\downarrow\rangle\}$. Singlet states with two electrons with one dot must be included too, meaning that the full basis is $\{|\uparrow\uparrow\rangle, |\uparrow\downarrow\rangle, |\downarrow\uparrow\rangle, |\downarrow\downarrow\rangle$, S(0,2), S(2,0)$\}$. The Hubbard Hamiltonian

of a silicon DQD in this basis is [79]

$$H' = \begin{bmatrix} \overline{E}_z & 0 & 0 & 0 & 0 & 0 \\ 0 & \frac{\Delta E_z}{2} & 0 & 0 & ht_0 & ht_0 \\ 0 & 0 & -\frac{\Delta E_z}{2} & 0 & -ht_0 & -ht_0 \\ 0 & 0 & 0 & -\overline{E}_z & 0 & 0 \\ 0 & ht_0 & -ht_0 & 0 & U-\epsilon & 0 \\ 0 & ht_0 & -ht_0 & 0 & 0 & U+\epsilon \end{bmatrix}, \tag{5.1}$$

where U is the Coulomb energy of the quantum dot (assumed equal for the two dots), ϵ is the energy detuning between the dots and t_0 is the tunnel coupling, while $\overline{E}_z = \frac{E_{z_1}+E_{z_0}}{2}$ and $\Delta E_z = E_{z_1} - E_{z_0}$ are the average and the difference of the qubits Zeeman splittings, respectively. In fact, as mentioned in Section 4.2.3, E_z, and thus the resonance frequency, must be different for each qubit for single-qubit addressability purpose. Section 5.1.3 will show that the ΔE_z parameter plays also a crucial role in the definition of the device two-qubit native gate.
The energy diagram derived from this Hamiltonian (Figure 5.1) shows an interesting aspect of the structure when the detuning approaches the U value: due to the Pauli Spin Blockade principle, already introduced in Section 3.2.2, S(2,0) and S(0,2), being singlet states, only interact [57] with the $|\uparrow\downarrow\rangle$ and $|\downarrow\uparrow\rangle$ states, since $|\uparrow\uparrow\rangle$ and $|\downarrow\downarrow\rangle$ are exactly the two triplet states $T_+(1,1)$ and $T_-(1,1)$, respectively. The energy diagram is obtained using $U = 0.2$ meV, $t_0 = 250$ MHz, $\overline{E}_z = 10$ µeV and $\Delta E_z = 3$ µeV, which yield $f_{0_0} \approx 2.8$ GHz and $f_{0_1} \approx 2.1$ GHz as qubits resonance frequencies.

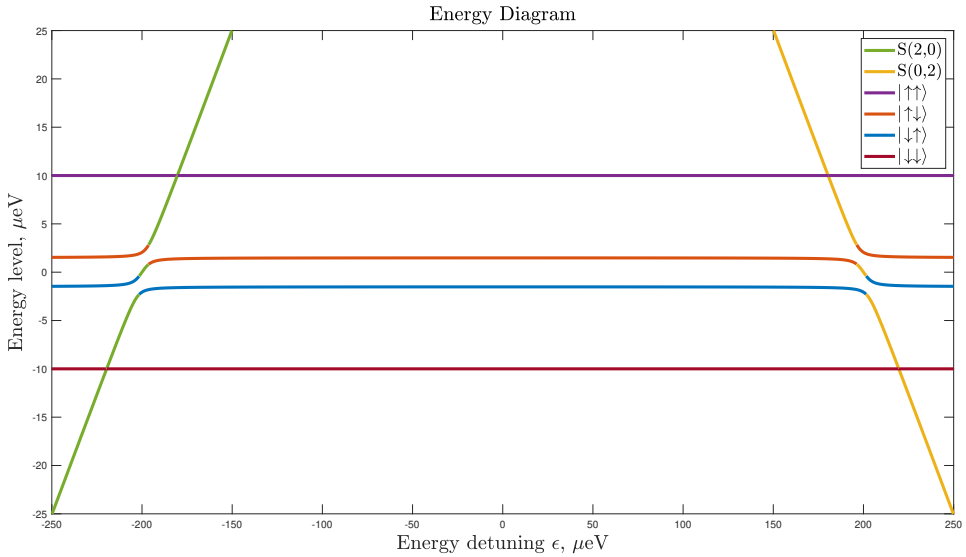

Figure 5.1: Energy diagram of a DQD, derived from the Hubbard Hamiltonian.

Moreover, zooming on one of the two transition zones, e.g. the (0,2) one, the mechanism that rules the two-qubit interaction can be studied (Figure 5.3). In this

detuning region, the resonance frequency of each qubit varies according to the state of the other qubit. This conditional change of the resonance frequency of a qubit is what allows two-qubit gates. Therefore, four frequencies can be defined [11]:

- f_1: the resonance frequency of q_0 when q_1 is in $|\downarrow\rangle$;
- f_2: the resonance frequency of q_0 when q_1 is in $|\uparrow\rangle$;
- f_3: the resonance frequency of q_1 when q_0 is in $|\downarrow\rangle$;
- f_4: the resonance frequency of q_1 when q_0 is in $|\uparrow\rangle$.

The parameter that sums up this phenomenon is the exchange interaction J, computed as $f_2 - f_1$ or $f_4 - f_3$. The four frequencies have been computed on MATLAB from the energy diagram of Figure 5.1 as

- $f_1 = \frac{1}{h}\left(E_{|\downarrow\uparrow\rangle} - E_{|\downarrow\downarrow\rangle}\right)$;
- $f_2 = \frac{1}{h}\left(E_{|\uparrow\uparrow\rangle} - E_{|\uparrow\downarrow\rangle}\right)$;
- $f_3 = \frac{1}{h}\left(E_{|\uparrow\downarrow\rangle} - E_{|\downarrow\downarrow\rangle}\right)$;
- $f_4 = \frac{1}{h}\left(E_{|\uparrow\uparrow\rangle} - E_{|\downarrow\uparrow\rangle}\right)$.

Their behaviour and the exchange interaction J have been compared with the outcome of a similar analysis described in [80] (Figure 5.2). Note that the MATLAB results are numerically different from those of the paper since the input parameters that describe the system have been chosen to be diverse from the reference values for sake of clarity in the MATLAB plots.

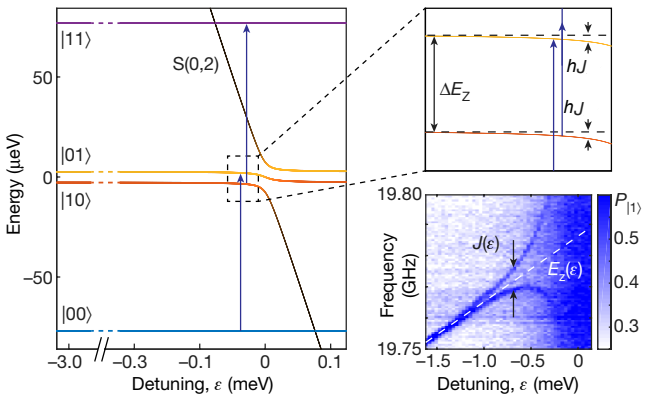

Figure 5.2: Results of the exchange interaction analysis. hJ is computed as the difference between the energy level of $|\uparrow\downarrow\rangle$ and $|\downarrow\uparrow\rangle$ (black dotted line) and their curvature in the exchange region (yellow and red lines). Adapted from [80].

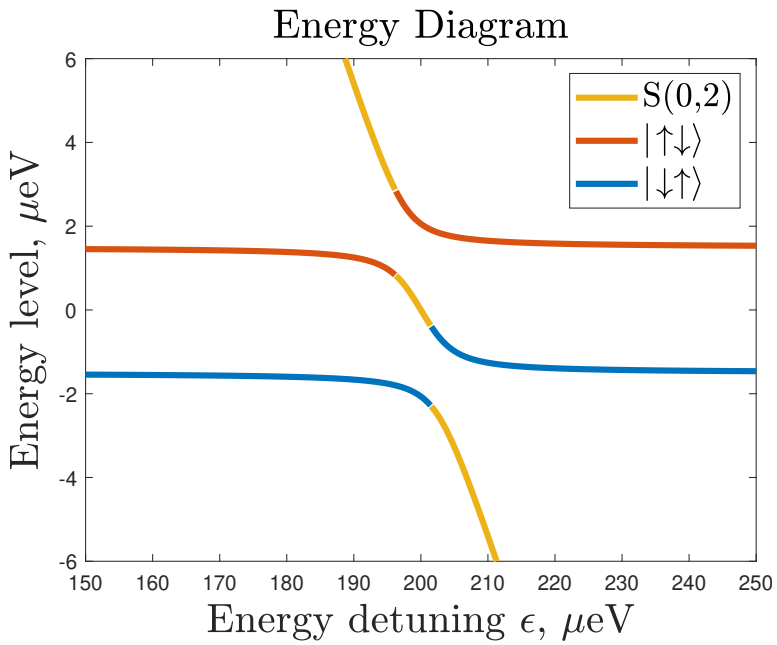

Figure 5.3: Zoom on (0,2) transition region. The $|\uparrow\downarrow\rangle$ and the $|\downarrow\uparrow\rangle$ states bend in the vicinity of the crossing with the S(0,2) state and thus the resonance frequencies change.

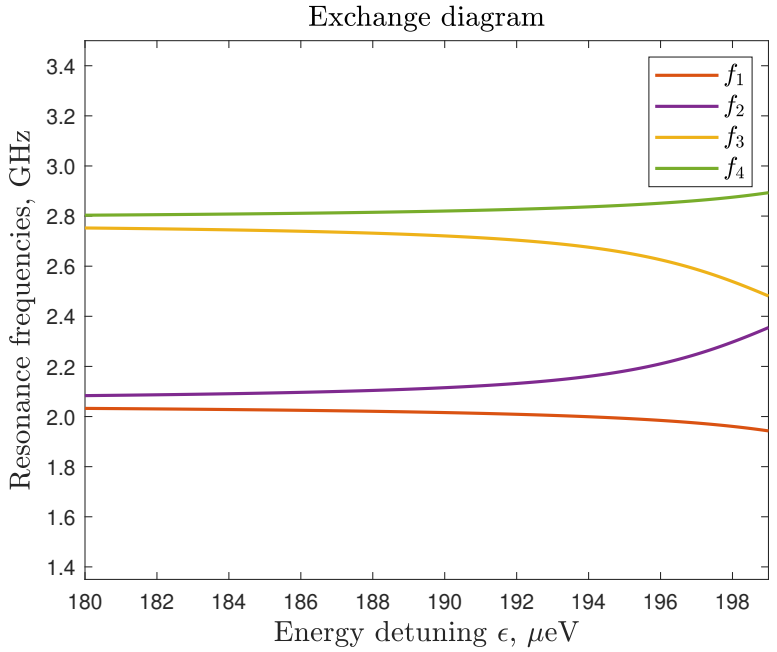

Figure 5.4: Exchange diagram of the system.

The exchange diagram, i.e. the plot of the four frequencies with respect to the detuning between the dots, clearly shows the capability of this type of structure (Figure 5.4). Indeed, one can set the system in the single-qubit gate regime — e.g. $\epsilon < 180$ µeV — where the resonance frequency of each qubit does not depend on the state of the other, or in the two-qubit gate one — e.g. 190 µeV $< \epsilon <$ 200 µeV — where instead the conditional variation of the frequencies is active, by just controlling the value of the detuning. In particular, for a low detuning, the system is far from the (0,2) transition region and the frequencies are fixed to their nominal values ($\sim$ 2.1 GHz and 2.8 GHz), while for values of detuning similar to U (200 µeV), the frequencies start to vary and one can perform two-qubit gates [76]. This is one of the strengths of quantum dot qubits, since, as already explained in Section 3.1.2, the detuning is easily tunable through the application of voltages on the device plunger gates. This functioning is summed up in the $J(\epsilon)$ plot (Figure 5.5). The strength of the exchange interaction can be tuned through t_0 too, since, for higher tunnel couplings, the curvature of the $|\uparrow\downarrow\rangle$ and $|\downarrow\uparrow\rangle$ states increase, thus incrementing the hJ value (Figure 5.2).

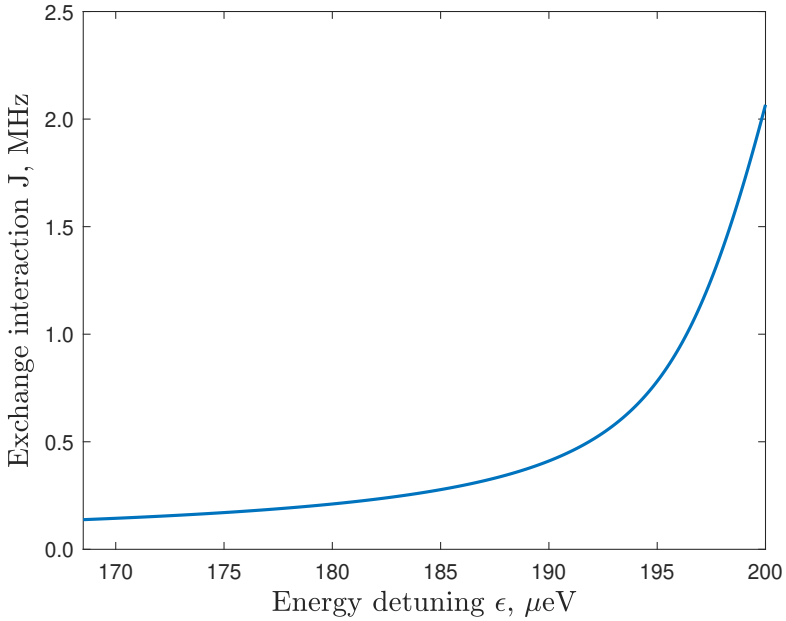

Figure 5.5: Exchange interaction variation with respect to the detuning ϵ.

5.1.2 The Schrieffer–Wolff transformation

Despite the S(2,0) and S(0,2) states have to be considered in the Hamiltonian since their presence strongly influences the structure behaviour, the computational basis must still be $\{|\uparrow\uparrow\rangle, |\uparrow\downarrow\rangle, |\downarrow\uparrow\rangle, |\downarrow\downarrow\rangle\}$. Hence, the Hamiltonian must be transformed through an approximation that allows one to reduce its basis to the computational

one, while keeping the extra states contribute to the system. The Schrieffer–Wolff (SW) transformation perfectly serves this purpose [81]: the idea is that if one assumes that the operating regime of the system is a range of detuning that never gets "too close" to the (1,1)-(0,2) (or (1,1)-(2,0)) transitions, the S(2,0) and S(0,2) states can be neglected. The "too close" is defined by the applicability condition of this transformation, which is $U - \epsilon \gg t_0$; this constraint, if respected, permits the transformation of the matrix of Equation (5.1) into the SW Hamiltonian in the $\{|\uparrow\uparrow\rangle, |\uparrow\downarrow\rangle, |\downarrow\uparrow\rangle, |\downarrow\downarrow\rangle\}$ basis, which is [76, 82]

$$H'^{SW} = \begin{bmatrix} \overline{E}_z & 0 & 0 & 0 \\ 0 & \frac{\Delta E_z}{2} - \alpha(\Delta E_z) & \beta(\Delta E_z) & 0 \\ 0 & \beta(\Delta E_z) & -\frac{\Delta E_z}{2} - \alpha(-\Delta E_z) & 0 \\ 0 & 0 & 0 & -\overline{E}_z \end{bmatrix}, \tag{5.2}$$

where $\alpha(\Delta E_z)$ and $\beta(\Delta E_z)$ are the terms that take into account the S(2,0) and S(0,2) states effect on the system. These parameters are defined as

$$\begin{aligned} \alpha(\Delta E_z) &= \frac{t_0^2}{U - \epsilon - \frac{\Delta E_z}{2}} + \frac{t_0^2}{U + \epsilon - \frac{\Delta E_z}{2}}, \\ \beta(\Delta E_z) &= \frac{\alpha(\Delta E_z) + \alpha(-\Delta E_z)}{2}, \end{aligned} \tag{5.3}$$

and they are approximately equal to $\frac{hJ}{2}$. Hence, they represent the exchange interaction J effect due to the transition regions in a Hamiltonian written on a basis that neglects the S(2,0) and S(0,2) states. It is worth noting that the ΔE_z values used in real quantum devices only slightly influence the α and β parameters: the ΔE_z usually varies in a range between 10^{-8} and 10^{-6} eV, whereas U and the detuning ϵ used in two-qubit gates are always in the meV scale [76].
Now, as in Section 4.1.1, the basis must be changed in order to agree with the NMR standard, which is $\{|00\rangle, |01\rangle, |10\rangle, |11\rangle\}$. The transformation is equivalent to apply Equation (4.11) to both qubits. This is achievable by defining the change of basis matrix as

$$U_C = \begin{bmatrix} 0 & 1 \\ 1 & 0 \end{bmatrix} \otimes \begin{bmatrix} 0 & 1 \\ 1 & 0 \end{bmatrix} = \begin{bmatrix} 0 & 0 & 0 & 1 \\ 0 & 0 & 1 & 0 \\ 0 & 1 & 0 & 0 \\ 1 & 0 & 0 & 0 \end{bmatrix}. \tag{5.4}$$

The result of the transformation is the SW Hamiltonian in the $\{|\downarrow\downarrow\rangle, |\downarrow\uparrow\rangle, |\uparrow\downarrow\rangle, |\uparrow\uparrow\rangle\}$=$\{|00\rangle, |01\rangle, |10\rangle, |11\rangle\}$ basis,

$$H^{SW} = U_C H'^{SW} U_C^\dagger = \begin{bmatrix} -\overline{E}_z & 0 & 0 & 0 \\ 0 & -\frac{\Delta E_z}{2} - \alpha(-\Delta E_z) & \beta(\Delta E_z) & 0 \\ 0 & \beta(\Delta E_z) & \frac{\Delta E_z}{2} - \alpha(\Delta E_z) & 0 \\ 0 & 0 & 0 & \overline{E}_z \end{bmatrix}. \tag{5.5}$$

This is only the static part of the Hamiltonian, which must also describe the interaction between the MW magnetic field used for single-qubit gates and the two spins. The field is again defined as

$$\underline{B}_1 = 2B_1 \cos(\omega_{MW} t - \phi_1)\underline{\hat{x}}, \tag{5.6}$$

since it is applied through a MW antenna inside the device, and thus it affects every qubit in the system. Hence, the MW field is declared in the same way as in Section 4.1.2. Thus, the Hamiltonian becomes

$$H^{SW} = \begin{bmatrix} -\overline{E}_z & \frac{\hbar}{2}\omega_{1_0}\eta & \frac{\hbar}{2}\omega_{1_1}\eta & 0 \\ \frac{\hbar}{2}\omega_{1_0}\eta & -\frac{\Delta E_z}{2} - \alpha(-\Delta E_z) & \beta(\Delta E_z) & \frac{\hbar}{2}\omega_{1_1}\eta \\ \frac{\hbar}{2}\omega_{1_1}\eta & \beta(\Delta E_z) & \frac{\Delta E_z}{2} - \alpha(\Delta E_z) & \frac{\hbar}{2}\omega_{1_0}\eta \\ 0 & \frac{\hbar}{2}\omega_{1_1}\eta & \frac{\hbar}{2}\omega_{1_0}\eta & \overline{E}_z \end{bmatrix}, \tag{5.7}$$

where $\eta = \left(e^{j\omega_{MW}t}e^{-j\phi_1} + e^{-j\omega_{MW}t}e^{j\phi_1}\right)$ and $\omega_{1_i} = -\gamma_i B_1$ is the Rabi frequency of qubit q_i.
In order to remove the time dependence of the Hamiltonian, the system must be brought into a rotating frame. There are different choices for this rotating frame; the one used in this work is [79]

$$\begin{aligned} U_{RF} &= \begin{bmatrix} e^{-j\frac{\omega_{0_1}}{2}t} & 0 \\ 0 & e^{j\frac{\omega_{0_1}}{2}t} \end{bmatrix} \otimes \begin{bmatrix} e^{-j\frac{\omega_{0_0}}{2}t} & 0 \\ 0 & e^{j\frac{\omega_{0_0}}{2}t} \end{bmatrix} \\ &= \begin{bmatrix} e^{-j\overline{\omega}_0 t} & 0 & 0 & 0 \\ 0 & e^{-j\frac{\Delta\omega_0}{2}t} & 0 & 0 \\ 0 & 0 & e^{j\frac{\Delta\omega_0}{2}t} & 0 \\ 0 & 0 & 0 & e^{j\overline{\omega}_0 t} \end{bmatrix}, \end{aligned} \tag{5.8}$$

where $\overline{\omega}_0$ and $\Delta\omega_0$ are the average and the difference of the resonance frequencies ω_{0_1} and ω_{0_0}, respectively, with ω_{0_i} associated with qubit q_i. Applying Equation (4.22) yields

$$\tilde{H}^{SW} = U_{RF} H^{SW} U_{RF}^{\dagger} - j\hbar U_{RF} \frac{dU_{RF}^{\dagger}}{dt}, \tag{5.9}$$

whose two parts are studied separately. The latter is

$$
\begin{aligned}
j\hbar U_{RF}\frac{dU_{RF}^{\dagger}}{dt} &= j\hbar \begin{bmatrix} e^{-j\overline{\omega}_0 t} & 0 & 0 & 0 \\ 0 & e^{-j\frac{\Delta\omega_0}{2}t} & 0 & 0 \\ 0 & 0 & e^{j\frac{\Delta\omega_0}{2}t} & 0 \\ 0 & 0 & 0 & e^{j\overline{\omega}_0 t} \end{bmatrix} \cdot \\
&\quad \cdot \begin{bmatrix} j\overline{\omega}_0 e^{j\overline{\omega}_0 t} & 0 & 0 & 0 \\ 0 & j\frac{\Delta\omega_0}{2}e^{j\frac{\Delta\omega_0}{2}t} & 0 & 0 \\ 0 & 0 & -j\frac{\Delta\omega_0}{2}e^{-j\frac{\Delta\omega_0}{2}t} & 0 \\ 0 & 0 & 0 & -j\overline{\omega}_0 e^{-j\overline{\omega}_0 t} \end{bmatrix} \\
&= \begin{bmatrix} -\overline{E}_z & 0 & 0 & 0 \\ 0 & -\frac{\Delta E_z}{2} & 0 & 0 \\ 0 & 0 & \frac{\Delta E_z}{2} & 0 \\ 0 & 0 & 0 & \overline{E}_z \end{bmatrix},
\end{aligned}
\tag{5.10}
$$

while the former one is

$$
\begin{aligned}
H^{SW}U_{RF}^{\dagger} &= \begin{bmatrix} -\overline{E}_z & \frac{\hbar}{2}\omega_{1_0}\eta & \frac{\hbar}{2}\omega_{1_1}\eta & 0 \\ \frac{\hbar}{2}\omega_{1_0}\eta & -\frac{\Delta E_z}{2} - \alpha\left(-\Delta E_z\right) & \beta\left(\Delta E_z\right) & \frac{\hbar}{2}\omega_{1_1}\eta \\ \frac{\hbar}{2}\omega_{1_1}\eta & \beta\left(\Delta E_z\right) & \frac{\Delta E_z}{2} - \alpha\left(\Delta E_z\right) & \frac{\hbar}{2}\omega_{1_0}\eta \\ 0 & \frac{\hbar}{2}\omega_{1_1}\eta & \frac{\hbar}{2}\omega_{1_0}\eta & \overline{E}_z \end{bmatrix} \cdot \\
&\quad \cdot \begin{bmatrix} e^{j\overline{\omega}_0 t} & 0 & 0 & 0 \\ 0 & e^{j\frac{\Delta\omega_0}{2}t} & 0 & 0 \\ 0 & 0 & e^{-j\frac{\Delta\omega_0}{2}t} & 0 \\ 0 & 0 & 0 & e^{-j\overline{\omega}_0 t} \end{bmatrix} \\
&= \begin{bmatrix} -\overline{E}_z e^{j\overline{\omega}_0 t} & \frac{\hbar}{2}\omega_{1_0}\eta e^{j\frac{\Delta\omega_0}{2}t} & \frac{\hbar}{2}\omega_{1_1}\eta e^{-j\frac{\Delta\omega_0}{2}t} & 0 \\ \frac{\hbar}{2}\omega_{1_0}\eta e^{j\overline{\omega}_0 t} & \left(-\frac{\Delta E_z}{2} - \alpha\left(-\Delta E_z\right)\right)e^{j\frac{\Delta\omega_0}{2}t} & \beta\left(\Delta E_z\right)e^{-j\frac{\Delta\omega_0}{2}t} & \frac{\hbar}{2}\omega_{1_1}\eta e^{-j\overline{\omega}_0 t} \\ \frac{\hbar}{2}\omega_{1_1}\eta e^{j\overline{\omega}_0 t} & \beta\left(\Delta E_z\right)e^{j\frac{\Delta\omega_0}{2}t} & \left(\frac{\Delta E_z}{2} - \alpha\left(\Delta E_z\right)\right)e^{-j\frac{\Delta\omega_0}{2}t} & \frac{\hbar}{2}\omega_{1_0}\eta e^{-j\overline{\omega}_0 t} \\ 0 & \frac{\hbar}{2}\omega_{1_1}\eta e^{j\frac{\Delta\omega_0}{2}t} & \frac{\hbar}{2}\omega_{1_0}\eta e^{-j\frac{\Delta\omega_0}{2}t} & \overline{E}_z e^{-j\overline{\omega}_0 t} \end{bmatrix};
\end{aligned}
\tag{5.11}
$$

$$
\begin{aligned}
U_{RF}H^{SW}U_{RF}^{\dagger} = &\begin{bmatrix} e^{-j\overline{\omega}_0 t} & 0 & 0 & 0 \\ 0 & e^{-j\frac{\Delta\omega_0}{2}t} & 0 & 0 \\ 0 & 0 & e^{j\frac{\Delta\omega_0}{2}t} & 0 \\ 0 & 0 & 0 & e^{j\overline{\omega}_0 t} \end{bmatrix} \begin{bmatrix} -\overline{E}_z e^{j\overline{\omega}_0 t} \\ \frac{\hbar}{2}\omega_{1_0}\eta e^{j\overline{\omega}_0 t} \\ \frac{\hbar}{2}\omega_{1_1}\eta e^{j\overline{\omega}_0 t} \\ 0 \end{bmatrix} \\
&\begin{bmatrix} \frac{\hbar}{2}\omega_{1_0}\eta e^{j\frac{\Delta\omega_0}{2}t} & \frac{\hbar}{2}\omega_{1_1}\eta e^{-j\frac{\Delta\omega_0}{2}t} & 0 \\ \left(-\frac{\Delta E_z}{2} - \alpha\left(-\Delta E_z\right)\right) e^{j\frac{\Delta\omega_0}{2}t} & \beta\left(\Delta E_z\right) e^{-j\frac{\Delta\omega_0}{2}t} & \frac{\hbar}{2}\omega_{1_1}\eta e^{-j\overline{\omega}_0 t} \\ \beta\left(\Delta E_z\right) e^{j\frac{\Delta\omega_0}{2}t} & \left(\frac{\Delta E_z}{2} - \alpha\left(\Delta E_z\right)\right) e^{-j\frac{\Delta\omega_0}{2}t} & \frac{\hbar}{2}\omega_{1_0}\eta e^{-j\overline{\omega}_0 t} \\ \frac{\hbar}{2}\omega_{1_1}\eta e^{j\frac{\Delta\omega_0}{2}t} & \frac{\hbar}{2}\omega_{1_0}\eta e^{-j\frac{\Delta\omega_0}{2}t} & \overline{E}_z e^{-j\overline{\omega}_0 t} \end{bmatrix} \\
= &\begin{bmatrix} -\overline{E}_z & \frac{\hbar}{2}\omega_{1_0}\eta e^{-j\omega_{0_0}t} \\ \frac{\hbar}{2}\omega_{1_0}\eta e^{j\omega_{0_0}t} & -\frac{\Delta E_z}{2} - \alpha\left(-\Delta E_z\right) \\ \frac{\hbar}{2}\omega_{1_1}\eta e^{j\omega_{0_1}t} & \beta\left(\Delta E_z\right) e^{j\Delta\omega_0 t} \\ 0 & \frac{\hbar}{2}\omega_{1_1}\eta e^{j\omega_{0_1}t} \end{bmatrix} \\
&\qquad \begin{bmatrix} \frac{\hbar}{2}\omega_{1_1}\eta e^{-j\omega_{0_1}t} & 0 \\ \beta\left(\Delta E_z\right) e^{-j\Delta\omega_0 t} & \frac{\hbar}{2}\omega_{1_1}\eta e^{-j\omega_{0_1}t} \\ \frac{\Delta E_z}{2} - \alpha\left(\Delta E_z\right) & \frac{\hbar}{2}\omega_{1_0}\eta e^{-j\omega_{0_0}t} \\ \frac{\hbar}{2}\omega_{1_0}\eta e^{j\omega_{0_0}t} & \overline{E}_z \end{bmatrix}.
\end{aligned} \tag{5.12}
$$

The SW Hamiltonian in the rotating frame is thus

$$
\tilde{H}^{SW} = \begin{bmatrix} 0 & \frac{\hbar}{2}\omega_{1_0}\eta e^{-j\omega_{0_0}t} & \frac{\hbar}{2}\omega_{1_1}\eta e^{-j\omega_{0_1}t} & 0 \\ \frac{\hbar}{2}\omega_{1_0}\eta e^{j\omega_{0_0}t} & -\alpha\left(-\Delta E_z\right) & \beta\left(\Delta E_z\right) e^{-j\Delta\omega_0 t} & \frac{\hbar}{2}\omega_{1_1}\eta e^{-j\omega_{0_1}t} \\ \frac{\hbar}{2}\omega_{1_1}\eta e^{j\omega_{0_1}t} & \beta\left(\Delta E_z\right) e^{j\Delta\omega_0 t} & -\alpha\left(\Delta E_z\right) & \frac{\hbar}{2}\omega_{1_0}\eta e^{-j\omega_{0_0}t} \\ 0 & \frac{\hbar}{2}\omega_{1_1}\eta e^{j\omega_{0_1}t} & \frac{\hbar}{2}\omega_{1_0}\eta e^{j\omega_{0_0}t} & 0 \end{bmatrix}. \tag{5.13}
$$

5.1.3 Two-qubit native gate analysis

The Hamiltonian of Equation (5.13) has to be treated separately for the two-qubit gates and the single-qubit ones. In the first case, the MW field is switched off, i.e. $B_1 = 0$, yielding $\omega_{1_i} = 0\ \forall i$. The Hamiltonian becomes

$$
\tilde{H}^{SW} = \begin{bmatrix} 0 & 0 & 0 & 0 \\ 0 & -\alpha\left(-\Delta E_z\right) & \beta\left(\Delta E_z\right) e^{-j\Delta\omega_0 t} & 0 \\ 0 & \beta\left(\Delta E_z\right) e^{j\Delta\omega_0 t} & -\alpha\left(\Delta E_z\right) & 0 \\ 0 & 0 & 0 & 0 \end{bmatrix}, \tag{5.14}
$$

which shows that it still depends on time though the exponentials of the β terms. The idea is to try to approximate this exponentials with either 1 or 0. The argument of the exponential is $\Delta\omega_0 t$, where t, the duration of the two-qubit gate, is usually on the order of tens of ns.

In practice, a two-qubit gate in a DQD device is realized in the following way:

- t_0 is set to the operating value through the barrier gate;
- Plunger gates are used to set the detuning value in the vicinity of U to activate J;
- The detuning is brought back to 0 after a time t.

It is worth noting that the operation is fully electrical, as it only requires the control of the gate voltages. The detuning regulation is called J pulse. This manipulation generates two possible two-qubit native gates depending on the value of ΔE_z with respect to t_0: the $\sqrt{\text{SWAP}}$ and the CPHASE.

Two-qubit native gate analysis: $\sqrt{\text{SWAP}}$

The first approximation, $e^{j\Delta\omega_0 t} \approx 1$, yields

$$\tilde{H}^{SW} = \begin{bmatrix} 0 & 0 & 0 & 0 \\ 0 & -\alpha\left(-\Delta E_z\right) & \beta\left(\Delta E_z\right) & 0 \\ 0 & \beta\left(\Delta E_z\right) & -\alpha\left(\Delta E_z\right) & 0 \\ 0 & 0 & 0 & 0 \end{bmatrix}; \tag{5.15}$$

using MATLAB to apply Equation (4.21) to this Hamiltonian, for $t = \frac{1}{J}\pi \approx \frac{h}{2\beta}\pi$, generates a unitary evolution equal to

$$U = \exp\left(-\frac{j}{\hbar}\tilde{H}^{SW}t\right) = \begin{bmatrix} 1 & 0 & 0 & 0 \\ 0 & 0 & 1 & 0 \\ 0 & 1 & 0 & 0 \\ 0 & 0 & 0 & 1 \end{bmatrix}. \tag{5.16}$$

The physical explanation of this result is the following: in order to have $e^{j\Delta\omega_0 t} \approx 1$, the product $\Delta\omega_0 t$ must be as small as possible. The two terms come from two different main parameters: $\Delta\omega_0$ is practically equal to the difference between the Zeeman splittings ΔE_z up to the $\hbar$ constant, while t is inversely proportional to the J parameter - and thus to β (Section 5.1.2) - which acts like a frequency and is in turn strongly linked to the tunnel coupling t_0 (see Equation (5.3)). Overall:

$$\begin{aligned} &\Delta E_z \downarrow \Longrightarrow \Delta\omega_0 \downarrow \\ &t_0, J \uparrow \Longrightarrow t \downarrow \end{aligned} \tag{5.17}$$

This means that the $U(t)$ evolution in Equation (5.16) is obtained when ht_0 (or hJ) $\gg \Delta E_z$. The condition of a small ΔE_z changes the system energy diagram [76]: the $|\uparrow\downarrow\rangle$ and the $|\downarrow\uparrow\rangle$ states get close and mix together, generating the S(1,1) and T_0(1,1) states described in Section 3.1.3 (Figure 3.10). In these circumstances, the system

basis becomes $\{\mathrm{T}_+(1,1), \mathrm{T}_0(1,1), \mathrm{S}(1,1), \mathrm{T}_-(N_L,N_R)\}$; since the non-zero terms of the Hamiltonian are in the positions (2,2), (2,3), (3,2) and (3,3) in the matrix of Equation (5.15), they only affect $\mathrm{T}_0(1,1)$ and $\mathrm{S}(1,1)$. Setting $t = \frac{1}{J}\pi \approx \frac{h}{2\beta}\pi$, the exchange interaction is applied for an amount of time that yields a phase difference of π between the $\mathrm{S}(1,1)$ and $\mathrm{T}_0(1,1)$ states [83]. Suppose now that the system starts, for $t = 0$, in the $|\uparrow\downarrow\rangle$ state; this can be conveniently rewritten as

$$|\uparrow\downarrow\rangle = \frac{1}{2}\left(|\uparrow\downarrow\rangle - |\downarrow\uparrow\rangle + |\uparrow\downarrow\rangle + |\downarrow\uparrow\rangle\right) = \frac{1}{\sqrt{2}}\left(|\mathrm{S}(1,1)\rangle + |\mathrm{T}_0(1,1)\rangle\right). \tag{5.18}$$

Then, after turning on the exchange interaction for $t = \frac{1}{J}\pi \approx \frac{h}{2\beta}\pi$, a π phase difference is applied:

$$\begin{aligned}\frac{1}{\sqrt{2}}\left(|\mathrm{S}(1,1)\rangle + e^{-j\pi}|\mathrm{T}_0(1,1)\rangle\right) &= \frac{1}{\sqrt{2}}\left(|\mathrm{S}(1,1)\rangle - |\mathrm{T}_0(1,1)\rangle\right) \\ &= \frac{1}{2}\left(|\uparrow\downarrow\rangle - |\downarrow\uparrow\rangle - |\uparrow\downarrow\rangle - |\downarrow\uparrow\rangle\right) \\ &= -|\downarrow\uparrow\rangle\,.\end{aligned} \tag{5.19}$$

The system has thus undergone a SWAP operation, i.e. the states of the qubits have been swapped ($|\uparrow\downarrow\rangle \longrightarrow |\downarrow\uparrow\rangle$). Therefore, halving the duration of the gate, which generates a $\frac{\pi}{2}$ phase difference, a $\sqrt{\mathrm{SWAP}}$ is realized:

$$U = \begin{bmatrix} 1 & 0 & 0 & 0 \\ 0 & \frac{1+j}{2} & \frac{1-j}{2} & 0 \\ 0 & \frac{1-j}{2} & \frac{1+j}{2} & 0 \\ 0 & 0 & 0 & 1 \end{bmatrix}. \tag{5.20}$$

In summary, a device with the $\sqrt{\mathrm{SWAP}}$ as native gate has a small ΔE_z and is very fast in performing two-qubit gates. A realistic value for ΔE_z is 40 neV, which means $\Delta f_0 \approx 10$ MHz, a resonance frequency difference that can be obtained through g-factor variations due to spin-orbit coupling [84]. The tunnel coupling t_0 is usually set to a high value , e.g. 900 MHz, to reduce the gate duration, together with a detuning energy close to U, such as $\epsilon = 0.61$ meV for $U = 0.9$ meV [11]. This values yield a $\sqrt{\mathrm{SWAP}}$ duration of 9 ns [84].

Two-qubit native gate analysis: CPHASE

The second approximation, $e^{j\Delta\omega_0 t} \approx 0$, yields

$$\tilde{H}^{SW} = \begin{bmatrix} 0 & 0 & 0 & 0 \\ 0 & -\alpha\left(-\Delta E_z\right) & 0 & 0 \\ 0 & 0 & -\alpha\left(\Delta E_z\right) & 0 \\ 0 & 0 & 0 & 0 \end{bmatrix}. \tag{5.21}$$

This approximation is obtained when the product $\Delta\omega_0 t$ is large, meaning that ΔE_z must be very high, since the duration of the gate cannot be longer than hundreds of ns — values of 150 ns are reported [38], but the state of the art trend is to try to reduce it [42] — for device performance reasons. Hence, the condition is $\Delta E_z \gg t_0$ (or J), which gives a significant difference between the $|\uparrow\downarrow\rangle$ and the $|\downarrow\uparrow\rangle$ states, which are energetically separated (Figure 5.1). Hence, switching on the exchange interaction for $t = \frac{1}{J}\pi \approx \frac{h}{2\beta}\pi$, a π phase difference is applied to these states, yielding

$$U = \exp\left(-\frac{j}{\hbar}\tilde{H}^{SW}t\right) = \begin{bmatrix} 1 & 0 & 0 & 0 \\ 0 & j & 0 & 0 \\ 0 & 0 & j & 0 \\ 0 & 0 & 0 & 1 \end{bmatrix}. \tag{5.22}$$

This unitary evolution is, together with a single-qubit Z rotation of $-\frac{\pi}{2}$ on both qubits, equal to the CPHASE gate:

$$\text{CPHASE} = U_{native}\, R_{Z_1}\left(-\frac{\pi}{2}\right) R_{Z_0}\left(-\frac{\pi}{2}\right); \tag{5.23}$$

it is worth noting that since the phase difference has been chosen to be π, the CPHASE is equivalent to a CZ gate.
To sum up, the procedure used to perform this native gate is the same as the $\sqrt{\text{SWAP}}$ case; the only difference is that the J pulse lasts twice as long ($t = \frac{1}{J}\pi$). Since the large values of resonance frequency difference are usually attained through the integration of a micromagnet in the structure, which creates a static magnetic field gradient along the qubits direction, the range of ΔE_z values is very extended. In fact, it can go from hundreds of neV [38] to tens of µeV [80]. CPHASE gates generally last longer, therefore the values of t_0 and ϵ are usually smaller, e.g. 400 MHz and 0.3 meV, respectively, which give $t = 150$ ns [84]. Both of these native two-qubit gates, the $\sqrt{\text{SWAP}}$ and the CPHASE, are - again, up to single-qubit rotations [1] - equivalent to the CNOT, the quantum computing universal two-qubit gate:

$$\begin{aligned} \text{CNOT}_{c,t} &= H_t\, R_{Z_t}\left(\frac{\pi}{2}\right) R_{Z_c}\left(-\frac{\pi}{2}\right) \sqrt{\text{SWAP}}\, R_{Z_t}(\pi)\, \sqrt{\text{SWAP}}\, H_t \\ \text{CNOT}_{c,t} &= H_t\, \text{CPHASE}\, H_t, \end{aligned} \tag{5.24}$$

where the subscript c and t refer to the control and target qubits of the CNOT gate, respectively.

5.1.4 Single-qubit gate analysis

For single qubit gates, the exchange interaction is turned off (low detuning and tunnel coupling), and the MW field is applied. This yields

$$\begin{aligned}\alpha\left(\Delta E_z\right) &= \frac{t_0^2}{U-\epsilon-\frac{\Delta E_z}{2}} + \frac{t_0^2}{U+\epsilon-\frac{\Delta E_z}{2}} \approx \frac{2t_0^2}{U} \approx 0,\\ \beta\left(\Delta E_z\right) &= \frac{\alpha\left(\Delta E_z\right)+\alpha\left(-\Delta E_z\right)}{2} \approx 0\end{aligned} \tag{5.25}$$

and $B_1 \neq 0$, and thus the SW Hamiltonian becomes

$$\tilde{H}^{SW} = \frac{\hbar}{2}\begin{bmatrix} 0 & \omega_{1_0}\eta e^{-j\omega_{0_0}t} & \omega_{1_1}\eta e^{-j\omega_{0_1}t} & 0 \\ \omega_{1_0}\eta e^{j\omega_{0_0}t} & 0 & 0 & \omega_{1_1}\eta e^{-j\omega_{0_1}t} \\ \omega_{1_1}\eta e^{j\omega_{0_1}t} & 0 & 0 & \omega_{1_0}\eta e^{-j\omega_{0_0}t} \\ 0 & \omega_{1_1}\eta e^{j\omega_{0_1}t} & \omega_{1_0}\eta e^{j\omega_{0_0}t} & 0 \end{bmatrix}. \tag{5.26}$$

The $\eta e^{\pm j\omega_{0_i}t}$ term, such as in Equation (4.26), generates the following exponentials:

$$\begin{aligned}\eta e^{-j\omega_{0_0}t} &= e^{j(\omega_{MW}-\omega_{0_0})t}e^{-j\phi_1} + e^{-j(\omega_{MW}+\omega_{0_0})t}e^{j\phi_1};\\ \eta e^{-j\omega_{0_1}t} &= e^{j(\omega_{MW}-\omega_{0_1})t}e^{-j\phi_1} + e^{-j(\omega_{MW}+\omega_{0_1})t}e^{j\phi_1};\\ \eta e^{j\omega_{0_0}t} &= e^{j(\omega_{MW}+\omega_{0_0})t}e^{-j\phi_1} + e^{-j(\omega_{MW}-\omega_{0_0})t}e^{j\phi_1};\\ \eta e^{j\omega_{0_1}t} &= e^{j(\omega_{MW}+\omega_{0_0})t}e^{-j\phi_1} + e^{-j(\omega_{MW}-\omega_{0_0})t}e^{j\phi_1}.\end{aligned} \tag{5.27}$$

Now, exponentials with sum arguments can be neglected through the RWA, since ω_{MW} will be equal to the ω_0 of the gate target qubit, therefore $\omega_{MW}+\omega_{0_i}$ is $\sim 2\omega_{0_i}$. The RWA Hamiltonian is

$$\tilde{H}^{SW}_{RWA} = \frac{\hbar}{2}\begin{bmatrix} 0 & \omega_{1_0}e^{j(\omega_{MW}-\omega_{0_0})t}e^{-j\phi_1} & & \\ \omega_{1_0}e^{-j(\omega_{MW}-\omega_{0_0})t}e^{j\phi_1} & 0 & & \\ \omega_{1_1}e^{-j(\omega_{MW}-\omega_{0_1})t}e^{j\phi_1} & 0 & & \\ 0 & \omega_{1_1}e^{-j(\omega_{MW}-\omega_{0_1})t}e^{j\phi_1} & & \\ & & \omega_{1_1}e^{j(\omega_{MW}-\omega_{0_1})t}e^{-j\phi_1} & 0 \\ & & 0 & \omega_{1_1}e^{j(\omega_{MW}-\omega_{0_1})t}e^{-j\phi_1} \\ & & 0 & \omega_{1_0}e^{j(\omega_{MW}-\omega_{0_0})t}e^{-j\phi_1} \\ & & \omega_{1_0}e^{-j(\omega_{MW}-\omega_{0_0})t}e^{j\phi_1} & 0 \end{bmatrix}. \tag{5.28}$$

Now, assuming that the single-qubit gate is applied to q_0 ($\omega_{MW} = \omega_{0_0}$), the matrix becomes

$$\tilde{H}_{RWA}^{SW} = \frac{\hbar}{2}\begin{bmatrix} 0 & \omega_{1_0}e^{-j\phi_1} & & \\ \omega_{1_0}e^{j\phi_1} & 0 & & \\ \omega_{1_1}e^{-j\Delta\omega_0 t}e^{j\phi_1} & 0 & & \\ 0 & \omega_{1_1}e^{-j\Delta\omega_0 t}e^{j\phi_1} & & \\ & & \omega_{1_1}e^{j\Delta\omega_0 t}e^{-j\phi_1} & 0 \\ & & 0 & \omega_{1_1}e^{j\Delta\omega_0 t}e^{-j\phi_1} \\ & & 0 & \omega_{1_0}e^{-j\phi_1} \\ & & \omega_{1_0}e^{j\phi_1} & 0 \end{bmatrix}; \tag{5.29}$$

thus, the Hamiltonian still depends on time through the $e^{\pm j\Delta\omega_0 t}$ terms, which, however, can be neglected using the RWA again. This approximation is quite strong since it depends from the distance between the qubit resonance frequencies $\Delta\omega_0$: single-qubit gates in a DQD need a large $\Delta\omega_0$ to avoid off-resonance effects on non-target qubits. After this approximation, the Hamiltonian loses the time dependence, being

$$\tilde{H}_{RWA}^{SW} = \frac{\hbar}{2}\begin{bmatrix} 0 & \omega_{1_0}e^{-j\phi_1} & 0 & 0 \\ \omega_{1_0}e^{j\phi_1} & 0 & 0 & 0 \\ 0 & 0 & 0 & \omega_{1_0}e^{-j\phi_1} \\ 0 & 0 & \omega_{1_0}e^{j\phi_1} & 0 \end{bmatrix}, \tag{5.30}$$

and the unitary evolution matrix of the system can be easily computed on MATLAB as

$$U(t) = \exp\left(-\frac{j}{\hbar}\tilde{H}_{RWA}^{SW}t\right). \tag{5.31}$$

In practice, single qubit gates are implemented applying the MW field for a time $t = \frac{\theta}{\omega_{1_i}}$, where θ is the desired rotation angle, and with a phase ϕ_1 that decides the rotation axis, as explained in Section 4.2.2.

5.2 MATLAB model verification

5.2.1 The code structure and its validation

The MATLAB model described in Section 4.2.1 is modified in order to handle two-qubit gates. The core of the simulation is still the computation of the unitary evolution of the system, which happens in a dedicated file called *qubits_control.m*. Here, the Hamiltonian, which depends on the gate applied to the qubits, is computed and the $U(t)$ matrix is carried out through Equation (5.31). The native two-qubit gates are implemented through the *native.m* file, which, depending on

the values of t_0 and ΔE_z, understands the device regime and sets the phase difference due to the exchange interaction — $\frac{\pi}{2}$ for the $\sqrt{\text{SWAP}}$ and π for the CPHASE — to drive the *qubits_control.m* file into performing the correct native gate. Moreover, a QASM2.0 interpreter is added to the model to make it compatible with quantum assembly, the standard language for quantum algorithms programming. The result of the simulation is a histogram plot of the states probabilities and the fidelity of the system (Figure 5.6). The latter parameter will be explained in Section 6.2.1.
The approximations for the native two-qubit gate described in Section 5.1.3 are verified comparing the $U(t)$ computed by the MATLAB model and the one calculated by Quantum Toolbox in Python (QuTiP), a Python-based environment able to directly solve the Lindblad master equation, employed as a reference. The verification is performed for a set of values for t_0 and ΔE_z, to check the behaviour of the QuTiP/MATLAB error when these parameters are varied. This analysis is carried out for both native gate scenarios and for single-qubit gates.
The error ε is computed between the unitary evolutions calculated by the two simulations. In particular, it is carried out using the 2-norm of the difference between the matrices:

$$\varepsilon_{\%} = \|U_{MATLAB} - U_{QuTiP}\|_2 \cdot 100. \tag{5.32}$$

5.2.2 The $\sqrt{\text{SWAP}}$ case

The $\sqrt{\text{SWAP}}$ gate is modelled through the $e^{j\Delta\omega_0 t} \approx 1$ approximation, yielding a $t_0 \gg \Delta E_z$ regime. The input parameters for this simulation are derived from experimental data in the state of the art [11]. The values extracted from the reference are the two resonance angular frequencies $\omega_{0_1} = 2\pi f_{0_1} = 2\pi(6.9491$ GHz$) = 43.6625$ Grad/s and $\omega_{0_0} = 2\pi f_{0_0} = 2\pi(6.9601$ GHz$) = 43.7316$ Grad/s, which yield $\Delta\omega_0 = 2\pi\Delta f_0 = 2\pi(11$ MHz$) = 69.115$ Mrad/s, the duration of the two-qubit gate is $t = 9$ ns and the Coulomb charging energies of the dots U, both assumed equal to 0.9 meV. The tunnel coupling and detuning are not reported, and therefore their values are chosen in a reasonable range. t_0 is set to 900 MHz and ϵ to 0.61 meV: this ensures that the gate duration is 9 ns.
The simulations are performed spanning the t_0 and $\Delta\omega_0$ values around the starting experimental data (Figure 5.7). The two range of values are:

- $\Delta\omega_0 = 2\pi\Delta f_0 = 2\pi[6 : 16]$ MHz= $[37.6991 : 100.5310]$ Mrad/s;
- $t_0 = [0.7 : 1.1]$ GHz.

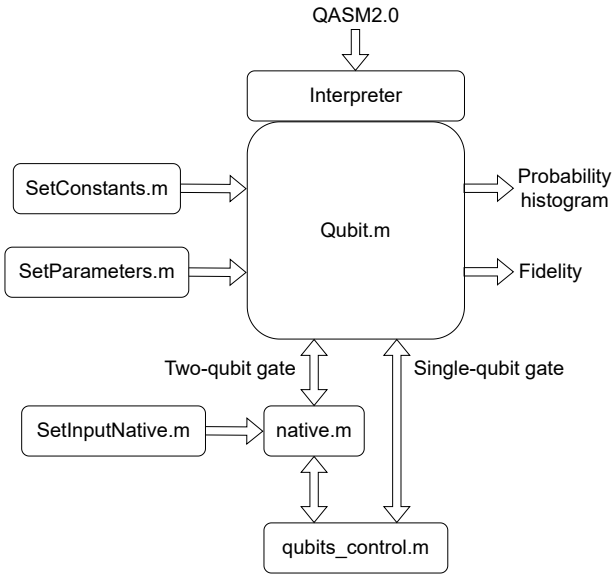

Figure 5.6: DQD model MATLAB code structure.

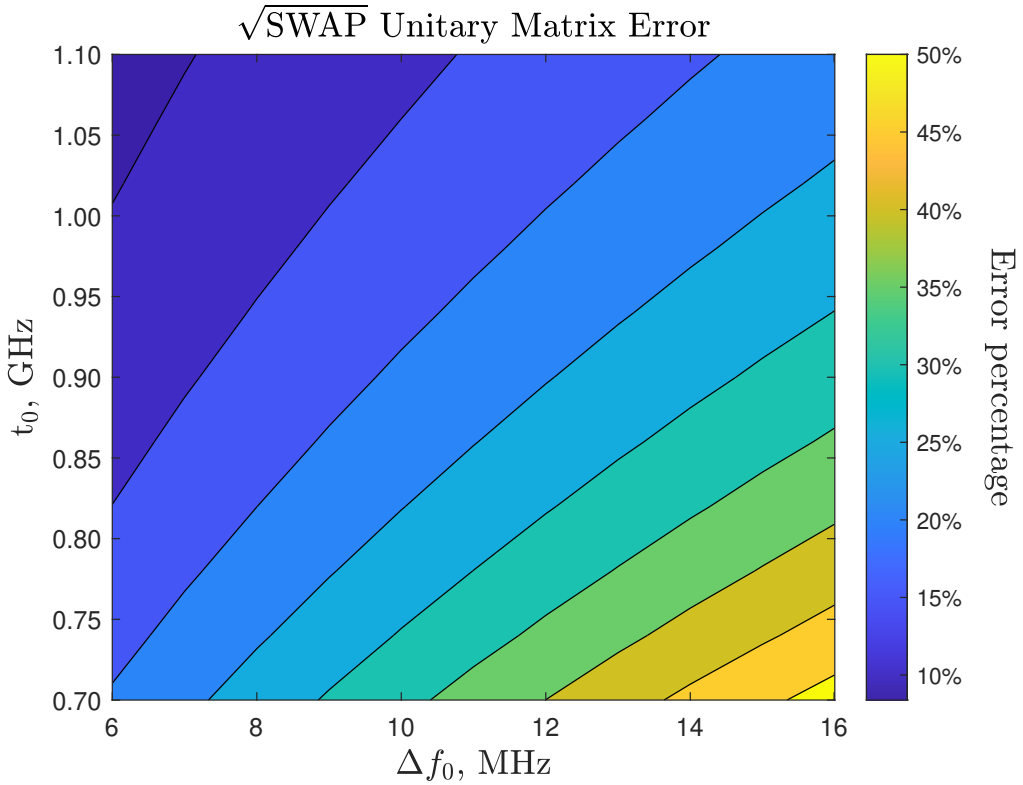

Figure 5.7: MATLAB-QuTiP error in the $\sqrt{\text{SWAP}}$ regime.

The behaviour of the error agrees with the theoretical expectations: it is indeed minimum for low values of Δf_0 and high t_0, since the gate duration t decreases when t_0 increases. These two conditions yield that the $e^{j\Delta\omega_0 t} \approx 1$ approximation is more accurate and thus the error is lower. However, in the center of the plot, where the values derived from the experimental data are represented, the error is $\sim 20\%$, meaning that the MATLAB model is not very accurate in the description of a realistic DQD structure with the $\sqrt{\text{SWAP}}$ as native gate.
The model validity is also tested on single-qubit gates, in particular on a $R_X(\pi)$ gate applied on q_0. The duration of the gate is set through the B_1 value to $t = 500$ ns [11], and the error is computed for the same set of ΔE_z values as the two-qubit gate simulation. On the other hand, the value of t_0 is set to 0, which translates in switching off the barrier gate voltage, since in single-qubit gates the exchange interaction must be negligible.

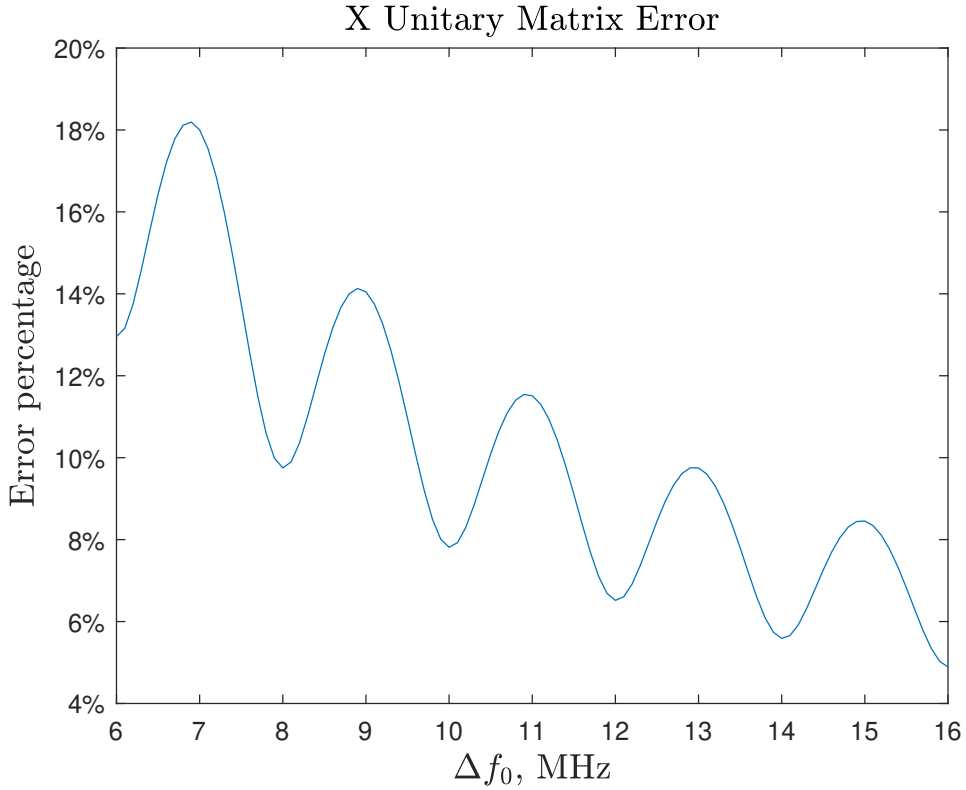

Figure 5.8: MATLAB-QuTiP error for a $R_X(\pi)$ gate on q_0 in the $\sqrt{\text{SWAP}}$ regime.

As expected, the error decreases when the resonance frequencies are more distant, i.e. when the resonance effects are lower. The plot shows oscillations due to the fact that QuTiP exactly integrates the Hamiltonian during the simulation. Indeed, the frequency "period" of this oscillation is 2 MHz, which is the inverse of the period of the integrated Hamiltonian; this value derives from the fact that the

$R_X(\pi)$ gate duration is $t = 500$ ns, therefore: $f_{osc} = \frac{1}{t} = \frac{1}{500 \cdot 10^{-9}} = 2$ MHz. Neglecting this ringing behaviour, the model error for the operating value $\Delta E_z = 11$ MHz is $\sim 10\%$.

5.2.3 The CPHASE case

The same analysis is performed for the other device operating regime, using the same type of simulation (Figure 5.9). The input values are again derived from experimental data [38]: the two resonance angular frequencies are $\omega_{0_1} = 2\pi f_{0_1} = 2\pi(15.64 \text{ GHz}) = 98.2690$ Grad/s and $\omega_{0_0} = 2\pi f_{0_0} = 2\pi(15.43 \text{ GHz}) = 96.9495$ Grad/s, meaning $\Delta\omega_0 = 2\pi\Delta f_0 = 2\pi(210 \text{ MHz}) = 1.3195$ Grad/s. A tunnel coupling $t_0 = 400$ MHz and a detuning $\epsilon = 0.3$ meV yield a gate duration $t = 150$ ns; U is again considered equal to 0.9 meV. The two ranges of values are:

- $\Delta\omega_0 = 2\pi\Delta f_0 = 2\pi[50 : 300]$ MHz$= [0.314 : 1.885]$ Grad/s;
- $t_0 = [300 : 600]$ MHz.

In this regime, the approximation is $e^{j\Delta\omega_0 t} \approx 0$, and the plot shows that the error is indeed minimum for high ΔE_z and low t_0. The error for the operating experimental values is less than 2%: the model describes quite precisely this native gate, since, usually, the practically physical values of ΔE_z for these structures are very high and thus the approximation holds better.
Again, the single-qubit gate error is explored for a $R_X(\pi)$ on q_0, setting the gate duration to $t = 500$ ns [11], $t_0 = 0$ and analyzing the same ΔE_z span as the CPHASE simulation (Figure 5.10). The error plot shows the same ringing behaviour as Figure 5.8, but the single-qubit gate error is much lower ($\sim 0.5\%$). The explanation is straightforward: the CPHASE scenario yield a higher ΔE_z, which allows one to easily neglect off-resonance effects, thus meaning that the model can accurately describe single-qubit gates in this operating conditions.

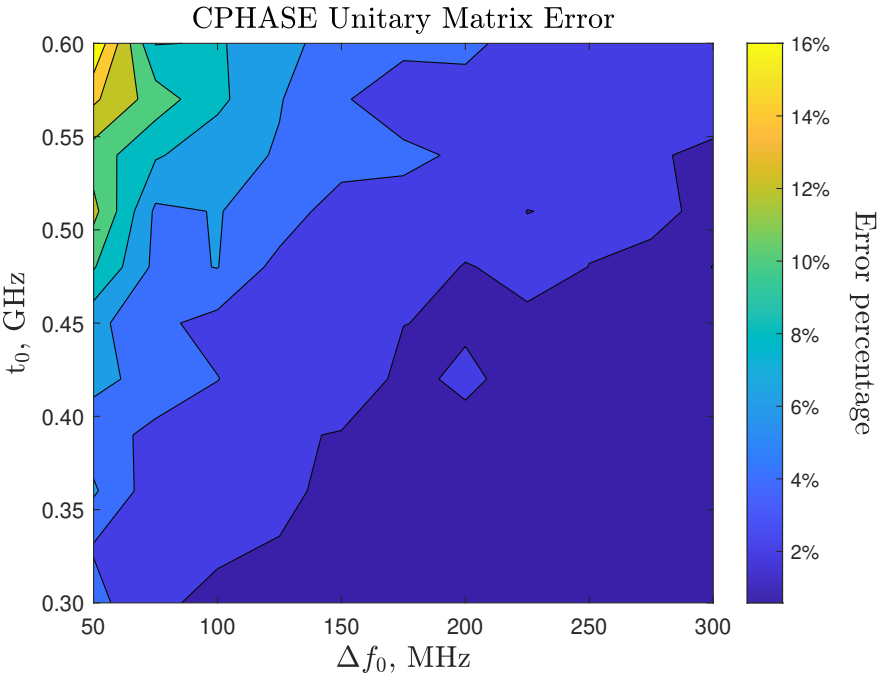

Figure 5.9: MATLAB-QuTiP error in the CPHASE regime.

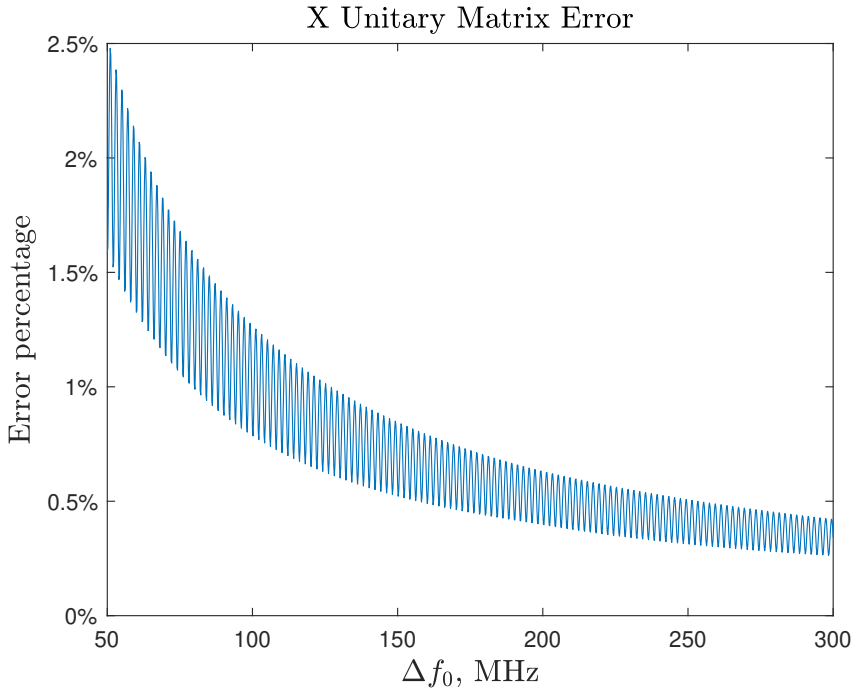

Figure 5.10: MATLAB-QuTiP error for a $R_X(\pi)$ gate on q_0 in the CPHASE regime.

Part III

Model validation

Chapter 6

Noise model implementation and results comparison

The final part of this thesis is devoted to the analysis of the noise algorithm used in the compact model to take into account relaxation and decoherence effects. The fidelity of the noisy model is computed on QuTiP through the simulation of a sequence of $R_x(\frac{\pi}{2})$ gates on each qubit varying the duration of the gate. The t value that maximizes the device fidelity is then used to compare the MATLAB model and the QuTiP results when relevant quantum circuits and algorithms are simulated.

6.1 The noise model

6.1.1 Probability redistribution algorithm

Chapter 5 was dedicated to the creation of an ideal compact model of the quantum device, exploiting some theoretical approximations in order to speed up the simulation time. The non-ideal behaviour of the structure is instead modelled on its own, depending only on the duration of the applied gate and, obviously on the relevant noise parameters. The two noise contributions explored in this thesis are *relaxation* and *decoherence* [13]. The former effect is responsible for the decay of the state vector towards the ground state $|0\rangle$: this means that the quantum system tends to "relax" into the lowest energy state after a certain amount time. Relaxation is usually modelled through the time constant T_1, called relaxation time. On the other hand, decoherence appears when the quantum system is not completely isolated from the environment: this condition generates the loss of the system phase information with time. The time constant related to this mechanism is the decoherence time T_2.

The two non-ideal effects are modelled through a noise algorithm [15] which computes decoherence adding an exponential decay to the off-diagonal terms of the system density matrix, and relaxation through a probability redistribution. The effects on a single-qubit density matrix in the time domain can be written as [16]

$$\begin{bmatrix} (a-a_0)e^{-\frac{t}{T_1}}+a_0 & be^{-\frac{t}{T_2}} \\ b^*e^{-\frac{t}{T_2}} & (a_0-a)e^{-\frac{t}{T_1}}+1-a_0 \end{bmatrix}, \tag{6.1}$$

where a and a_0 are the probabilities of measuring the qubit in $|0\rangle$ for $t = 0$ and $t \to \infty$, respectively. The algorithm tries to efficiently extend this formalism to the multi-qubit case.
The two effects are described separately; the decoherence process is modelled by a matrix, computed as the Kronecker product of the decoherence matrices of each of the n qubit:

$$D = \bigotimes_{i=n-1}^{0} D_i = D_{n-1} \otimes \cdots D_0, \tag{6.2}$$

where

$$D_i = \begin{bmatrix} 1 & e^{-\frac{t}{T_{2_i}}} \\ e^{-\frac{t}{T_{2_i}}} & 1 \end{bmatrix}, \tag{6.3}$$

where T_{2_i} is the decoherence time of the qubit q_i. The whole D matrix is then multiplied element by element to the system density matrix ρ.
On the other hand, the relaxation process is seen as a loss of probability of the three excited states ($|01\rangle$, $|10\rangle$ and $|11\rangle$); this probability is then given to the ground state $|00\rangle$. This phenomenon is described by a relaxation vector calculated as

$$\underline{r} = \bigotimes_{i=n-1}^{0} \begin{bmatrix} 1 \\ e^{-\frac{t}{T_{i_i}}} \end{bmatrix} = \begin{bmatrix} 1 \\ e^{-\frac{t}{T_{i_0}}} \\ . \\ . \\ . \\ \exp\left(-\sum_{i=0}^{n-1} \frac{t}{T_{1_i}}\right) \end{bmatrix} = \begin{bmatrix} r_{0,0} \\ r_{1,1} \\ . \\ . \\ . \\ r_{2^n-1,2^n-1} \end{bmatrix}, \tag{6.4}$$

where T_{1_i} is relaxation time of the qubit q_i. This vector is multiplied by the main diagonal of the density matrix ρ; then, the total probability lost by the excited states due to relaxation is then computed as the sum of each state probability loss:

$$P_{lost_{tot}} = \sum_k P_{lost_k} = \sum_k (1 - r_{k,k})\rho_{k,k}, \tag{6.5}$$

where $\rho_{k,k}$ is the (k,k) element of the density matrix ρ. $P_{lost_{tot}}$ is then summed to the $\rho(1,1)$ element, which represent the probability of the state $|00\rangle$. The probability

lost because of the relaxation phenomenon is thus all stored into the ground state of the system; this last step ensures that the trace of the system density matrix is unitary ($Tr(\rho) = 1$).
This algorithm is tested separately for the relaxation and the decoherence part. The former is verified initializing the system to $|00\rangle$ and applying a $R_X(\pi)$ on q_1 and q_0 individually and leaving the system freely evolve for a certain amount of time to check the relaxation behaviour of the single qubit. Then, the same procedure is applied to both qubits at the same time to see the effect on the whole system. The relaxation times of the qubits are taken from [38]: $T_{1_1} = 20.1$ ms and $T_{1_0} = 20.4$ ms. The probability of the state related to the case under simulation — e.g. when the $R_X(\pi)$ is applied only on q_0, one needs to look at the $|01\rangle$ state — is plotted with respect to the time period of the system free evolution. If, when analyzing single qubits, this probability is equal to $e^{-1} = 36.788\%$ for $t = T_{1_i}$, the relaxation effect is correct. Instead, for the two-qubit analysis, the probability of $|11\rangle$ must be 36.788% for $t = \frac{T_{1_1} T_{1_0}}{T_{1_1} + T_{1_0}} = 10.124$ ms, since the exponential decreases as $-t\left(\frac{1}{T_{1_1}} + \frac{1}{T_{1_0}}\right)$. Indeed, the plots show that the probabilities decay to 36.788% at the correct t instant in all three cases (Figure 6.1).

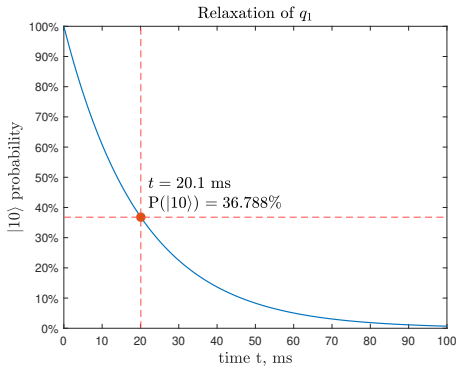

(a) T_{1_1} analysis.

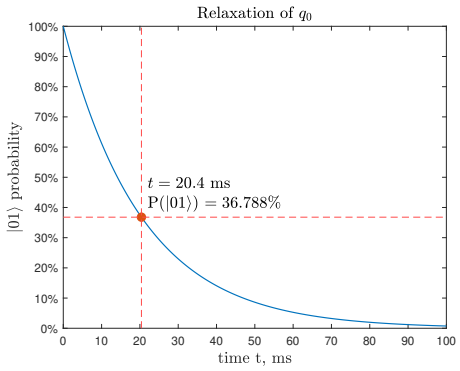

(b) T_{1_0} analysis.

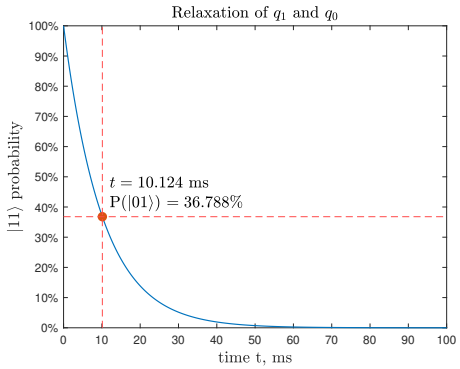

(c) Combined T_{1_1} and T_{1_0} analysis.

Figure 6.1: Relaxation decay for q_1, q_0 and both qubits together.

The procedure employed for the decoherence analysis is similar: starting from $|00\rangle$, a $R_Y(\frac{\pi}{2})$ is performed on q_0 and q_1 separately and then on both of them together. The decoherence matrix used in the algorithm is

$$\begin{bmatrix} 1 & e^{-\frac{t}{T_{2_1}}} \\ e^{-\frac{t}{T_{2_1}}} & 1 \end{bmatrix} \otimes \begin{bmatrix} 1 & e^{-\frac{t}{T_{2_0}}} \\ e^{-\frac{t}{T_{2_0}}} & 1 \end{bmatrix} = \\ = \begin{bmatrix} 1 & e^{-\frac{t}{T_{2_0}}} & e^{-\frac{t}{T_{2_1}}} & e^{-t\left(\frac{1}{T_{2_1}}+\frac{1}{T_{2_0}}\right)} \\ e^{-\frac{t}{T_{2_0}}} & 1 & e^{-t\left(\frac{1}{T_{2_1}}+\frac{1}{T_{2_0}}\right)} & e^{-\frac{t}{T_{2_1}}} \\ e^{-\frac{t}{T_{2_1}}} & e^{-t\left(\frac{1}{T_{2_1}}+\frac{1}{T_{2_0}}\right)} & 1 & e^{-\frac{t}{T_{2_0}}} \\ e^{-t\left(\frac{1}{T_{2_1}}+\frac{1}{T_{2_0}}\right)} & e^{-\frac{t}{T_{2_1}}} & e^{-\frac{t}{T_{2_0}}} & 1 \end{bmatrix}, \tag{6.6}$$

where T_{2_1} and T_{2_0} are the decoherence time constants of q_1 and q_0, respectively. Since this matrix is multiplied element by element to the system density matrix ρ, the terms that one has to inspect after the free evolution are (using MATLAB matrix notation):

- ρ(1,2) for the T_{2_0} constant;
- ρ(1,3) for the T_{2_1} constant;
- ρ(1,4) for the two decoherence effects combined.

However, the initial value of these density matrix elements is not 1; therefore, assuming to analyze T_{2_0}, the value $\rho(1,2) = k$ for $t = 0$ must be taken into account. Indeed, one must verify that $\rho(1,2) = ke^{-1}$ for $t = T_{2_0}$, where k is computed at the start of the simulation, after the application of the single-qubit gate. The ρ values for the three analyses are:

- $k = 0.4814 \Longrightarrow \rho(1,2) = ke^{-1} = 17.711\%$ for $t = T_{2_0}$;
- $k = 0.4799 \Longrightarrow \rho(1,3) = ke^{-1} = 17.655\%$ for $t = T_{2_1}$;
- $k = 0.2218 \Longrightarrow \rho(1,4) = ke^{-1} = 8.16\%$ for $t = \frac{T_{2_1}T_{2_0}}{T_{2_1}+T_{2_0}}$;

The decoherence times used are again taken from [38]: $T_{2_1} = 6.1$ µs and $T_{2_0} = 6.6$ µs, yielding $\frac{T_{2_1}T_{2_0}}{T_{2_1}+T_{2_0}} = 3.17$ µs. The plots depict a correct behaviour of the decoherence decay, meaning that the noise algorithm has been properly implemented in the MATLAB model (Figure 6.2).

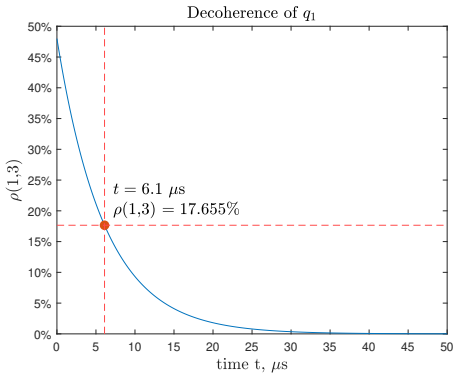

(a) T_{2_1} analysis.

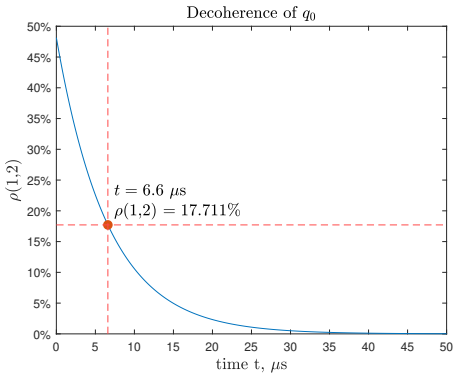

(b) T_{2_0} analysis.

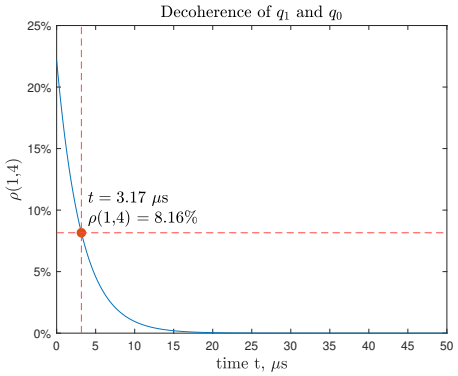

(c) Combined T_{2_1} and T_{2_0} analysis.

Figure 6.2: Decoherence decay for q_1, q_0 and both qubits together.

6.2 Quantum algorithms simulation

6.2.1 Fidelity analysis

The noise model described in Section 6.1.1 is implemented in QuTiP too, in order to have a reference that considers relaxation and decoherence contributions. The fidelity of the system, i.e. the measure of the "closeness" of the noisy model to the ideal quantum system, is thus analyzed in QuTiP. The fidelity is computed as [16]

$$\mathcal{F}(|\psi\rangle, \rho) = \sqrt{\langle\psi| \rho |\psi\rangle}, \tag{6.7}$$

where $|\psi\rangle$ is the ideal state vector, computed multiplying the initial state vector for the ideal unitary matrices of the gate applied to the qubits, and ρ is the density matrix, calculated through the model and the noise algorithm. Therefore, $\mathcal{F}$ is a quantity between 0 and 1 that indicates how close is the quantum system described by the density matrix ρ to the ideal one expressed by the state vector $|\psi\rangle$.
The fidelity is calculated applying a sequence of $R_X(\frac{\pi}{2})$ from the most significant qubit to (q_1) to the least significant one (q_0). The simulation is repeated for a range

of gate durations: $t = [2{:}200]$ ns; ω_1 — and thus B_1 — is changed accordingly to ensure that the rotation angle of single-qubit gate is $\theta = \frac{\pi}{2}$, since $\theta = \omega_1 t$. The resonance angular frequencies are $\omega_{0_1} = 2\pi f_{0_1} = 2\pi(15.64 \text{ GHz}) = 98.2690$ Grad/s and $\omega_{0_0} = 2\pi f_{0_0} = 2\pi(15.43 \text{ GHz}) = 96.9495$ Grad/s, while the relaxation and decoherence time constants are set to $T_{1_1} = 20.1$ ms, $T_{1_0} = 20.4$ ms, $T_{2_1} = 6.1$ µs and $T_{2_0} = 6.6$ µs [38].
The fidelity behaviour shows that the longer the gate is applied, the worse is the performance of the hardware, which however, in the simulated range, keeps a fidelity value > 0.985 (Figure 6.3a). The initial ringing is again due to the exact integration of the Hamiltonian carried out by QuTiP, which, as shown in the zoomed plot, causes an oscillating behaviour with a period of ~ 4.75 ns (Figure 6.3b). This is the period of the integrated Hamiltonian and it is related to the difference between the resonance frequencies of the qubits; in fact, $t_{osc} = \frac{1}{\Delta f_0} = \frac{1}{210 \text{ MHz}} \approx 4.78$ ns. Moreover, the effects of the duration of the single-qubit gate can be divided into two behaviours:

- Short MW pulses: the Fourier spectrum is broad and the off-resonance is thus pronounced but relaxation and decoherence are weak;

- Long MW pulses: a narrow Fourier spectrum yields lower off-resonance effects but larger relaxation and decoherence.

This justifies the substantial oscillations at the start of the fidelity plot, where the duration is small and thus the off-resonance is dominant.

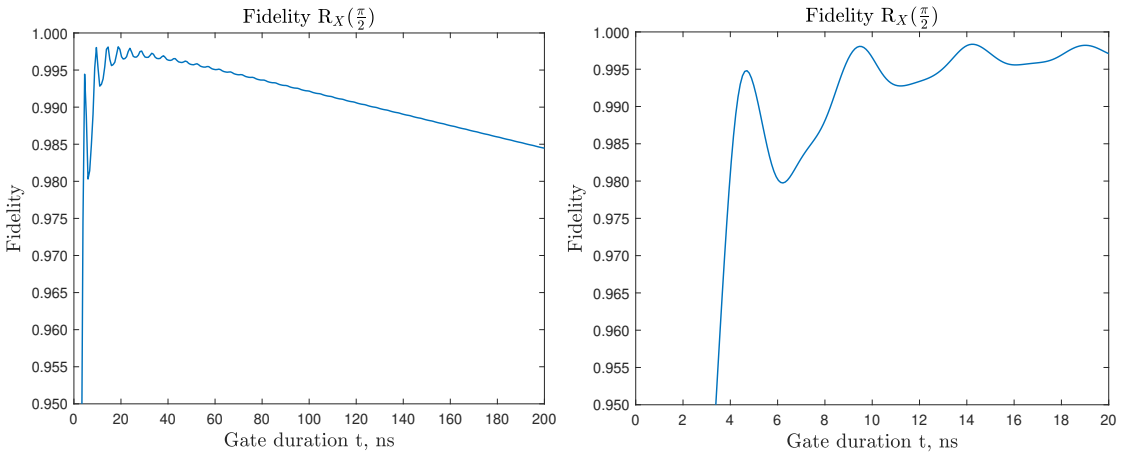

(a) Fidelity behaviour.

(b) Zoom on the initial ringing.

Figure 6.3: QuTiP fidelity of a sequence of $R_X(\frac{\pi}{2})$ gate on each qubit.

6.2.2 Ideal and noisy results

The MATLAB model has been also tested with some relevant quantum circuits and algorithms; its results have been compared to the QuTiP simulations. The system has been examined in the CPHASE regime, since, according to Section 5.2.3, it is where the error between the MATLAB approximations and the QuTiP exact Hamiltonian integration is lower. Therefore, the resonance angular frequencies are again set to $\omega_{0_1} = 2\pi f_{0_1} = 2\pi(15.64 \text{ GHz}) = 98.2690$ Grad/s and $\omega_{0_0} = 2\pi f_{0_0} = 2\pi(15.43 \text{ GHz}) = 96.9495$ Grad/s, yielding a $\Delta\omega_0 = 2\pi\Delta f_0 = 2\pi(210$ MHZ$) = 1.3195$ Grad/s. while the relaxation and decoherence time constants are $T_{1_1} = 20.1$ ms, $T_{1_0} = 20.4$ ms, $T_{2_1} = 6.1$ µs and $T_{2_0} = 6.6$ µs [38]. As in Section 5.2.3, the native two qubit gate is performed with $t_0 = 400$ MHz and $\epsilon = 0.3$ meV, with a U equal to 0.9 meV: the two-qubit native gate duration is thus 150 ns. On the other hand, the simulations have been ran with two different single-qubit gate time values, where the reference gate is a $R_X(\frac{\pi}{2})$:

- $t = 14.2$ ns, which means $B_1 = -\frac{\omega_1}{\gamma} = \frac{\pi}{2\gamma t} \approx 632.70$ µT: this t value maximizes the device fidelity, as shown in Figure 6.3b;
- $t = 250$ ns, which means $B_1 \approx 35.975$ µT: this is extracted from experimental data in literature [38].

The distance between the density matrix computed by the MATLAB model and the one calculated by QuTiP is measured through the Kullback-Leibler (KL) divergence [85, 86]. The probability of each state is derived from the diagonal of the density matrix and the KL divergence is computed as

$$D_{KL} = \sum_{i=0}^{2^n-1} P(|e_i\rangle) \log_2 \left(\frac{P(|e_i\rangle)}{Q(|e_i\rangle)} \right), \tag{6.8}$$

where n is the number of qubits, $|e_i\rangle$ are the orthonormal eigenstates of the σ_z operator ($|0\cdots0\rangle, \cdots, |1\cdots0\rangle$) and

$$\begin{aligned} P(|e_i\rangle) &= \rho_{\text{MATLAB}}(i,i) \\ Q(|e_i\rangle) &= \rho_{\text{QuTiP}}(i,i). \end{aligned} \tag{6.9}$$

If the probabilities coincide, D_{KL} is equal to 0, meaning that the smaller the KL divergence is, the closer the probabilities are.

The Bell state

The first simulation is run on the circuit that generates the Bell state $\frac{1}{\sqrt{2}}(|00\rangle + |11\rangle)$ from $|q_1 q_0\rangle = |00\rangle$, which is:

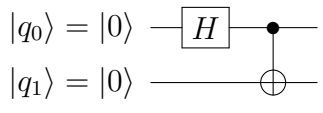

The results between the two models are very similar for $t = 250$ ns (Figure 6.4), with $D_{KL} = 0.0254$ and $t = 14.2$ ns (Figure 6.5), where $D_{KL} = 0.1679$. The significant discrepancies between the two simulations are the probabilities of the states $|01\rangle$ and $|10\rangle$; this is caused by the fact that, when $t = 250$ ns, decoherence effects become relevant, whereas a single-qubit gate duration of 14.2 ns is too fast to see the non-idealities.

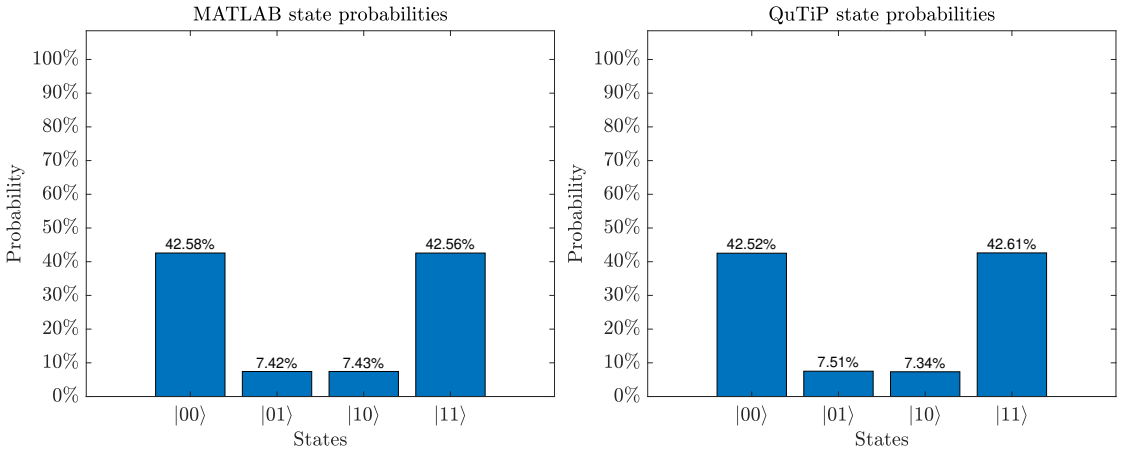

(a) MATLAB model results. (b) QuTiP results.

Figure 6.4: Probability comparison for a Bell state for $t = 250$ ns.

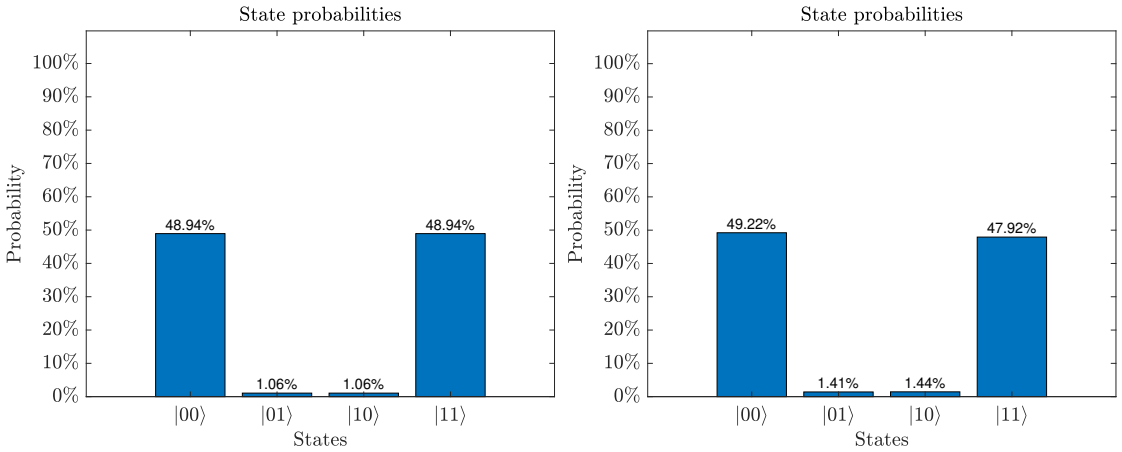

(a) MATLAB model results. (b) QuTiP results.

Figure 6.5: Probability comparison for a Bell state for $t = 14.2$ ns.

However, these results do not show a crucial difference between the MATLAB and QuTiP model in the $t = 14.2$ ns case. As mentioned in Section 6.2.1, short MW pulses generate large off-resonance effects; this mathematically translates into

the fact that the RWA used on the single-qubit Hamiltonian in Equation (5.30) is not sufficiently valid. Indeed, the 2-norm of the difference of the MATLAB and QuTiP density matrices gives an error of 27.61% due to off-resonance effects. The $t = 250$ ns simulation is not affected by this error ($\sim$0.58%); this has already been demonstrated in Section 5.2.3 (Figure 5.10).

SWAP gate

The next simulation models the implementation of a SWAP gate between the $|0\rangle$ and $|+\rangle = \frac{1}{\sqrt{2}}(|0\rangle + |1\rangle)$ states. The circuit is:

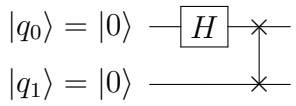

The SWAP is realized through three CNOT gates in the following way [87]:

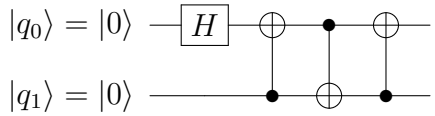

The results for $t = 250$ ns (Figure 6.6) give $D_{KL} = 0.0562$ and show that the state probabilities almost coincide. As in the Bell state simulation, the decoherence and relaxation affect the two systems in the same way since the noise algorithm is identical in the two models. When $t = 14.2$ ns (Figure 6.7), $D_{KL} = 0.0339$ and thus the probability distribution are almost the same, but the overall system density matrices of the two models are separated by an error of 5.18% due to the off-resonance effects.
The test is repeated on the same gate modifying the input states and realizing a SWAP between $|0\rangle$ and $|1\rangle$:

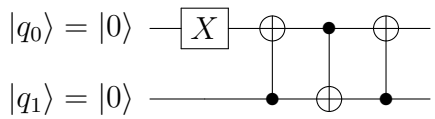

This circuit gives the usual similar results for $t = 250$ ns (Figure 6.8), with $D_{KL} = 0.0732$, whereas the $t = 14.2$ ns case (Figure 6.9) shows a higher error with respect to the precedent SWAP implementation, yielding $D_{KL} = 0.6209$ and an error between the models of 14.3312%. Both SWAP tests for $t = 250$ ns suffer from a more evident decoherence with respect to the Bell case, since the circuit clearly lasts longer and the noise effects begin to appear.

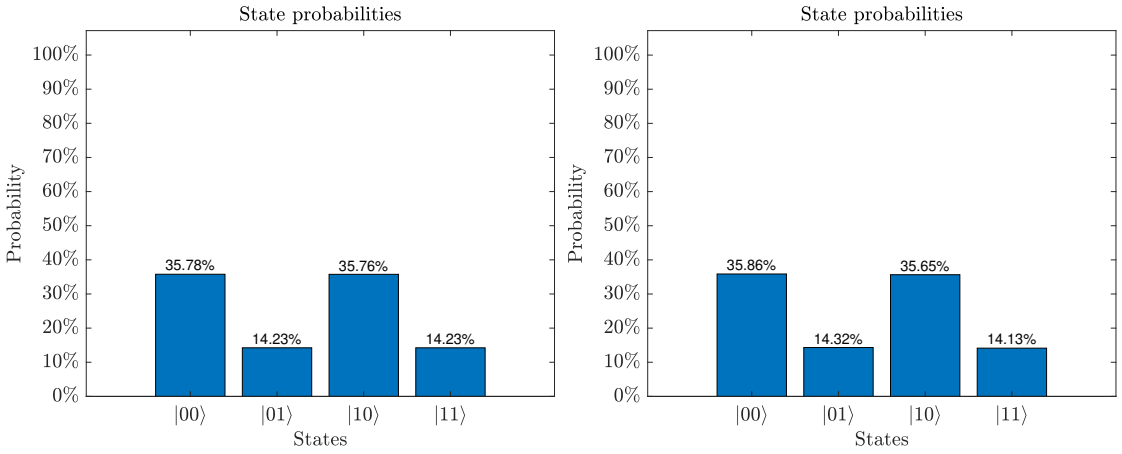

(a) MATLAB model results. (b) QuTiP results.

Figure 6.6: Probability comparison for a SWAP gate between the $|0\rangle$ and $|+\rangle$ states for $t = 250$ ns.

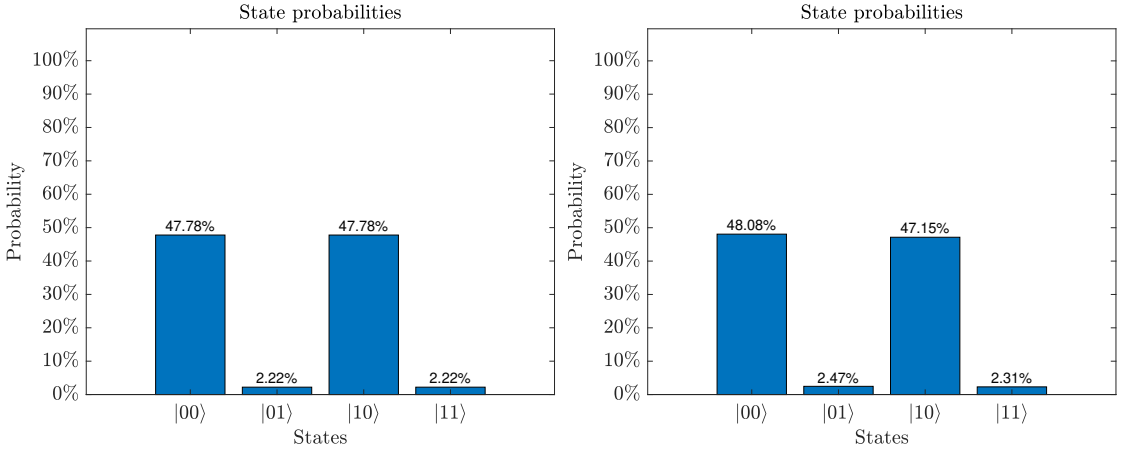

(a) MATLAB model results. (b) QuTiP results.

Figure 6.7: Probability comparison for a SWAP gate between the $|0\rangle$ and $|+\rangle$ states for $t = 14.2$ ns.

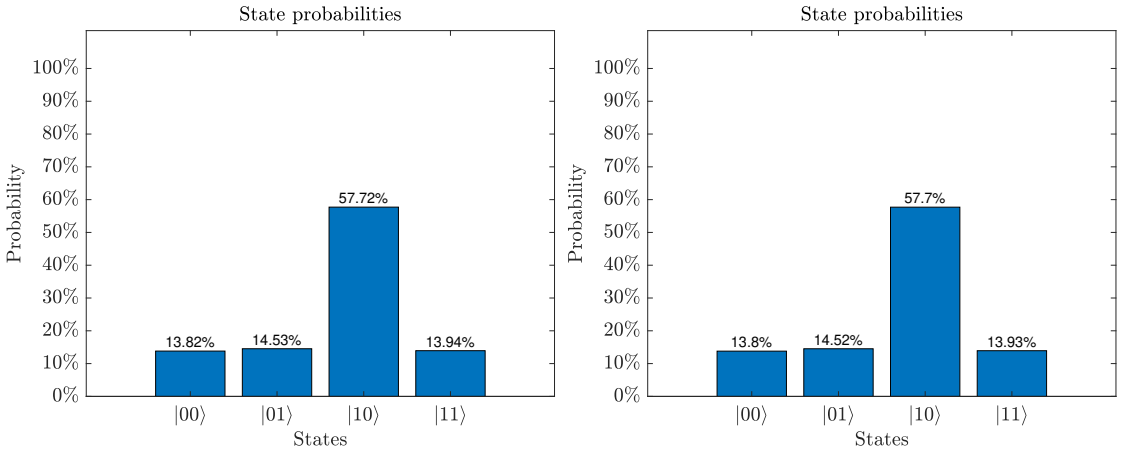

(a) MATLAB model results. (b) QuTiP results.

Figure 6.8: Probability comparison for a SWAP gate between the $|0\rangle$ and $|1\rangle$ states for $t = 250$ ns.

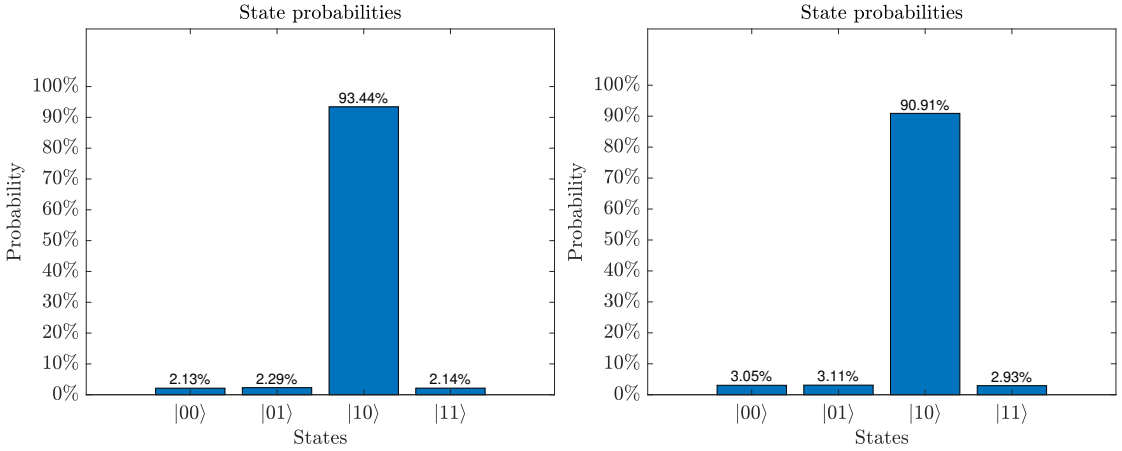

(a) MATLAB model results. (b) QuTiP results.

Figure 6.9: Probability comparison for a SWAP gate between the $|0\rangle$ and $|1\rangle$ states for $t = 14.2$ ns.

Deutsch's algorithm

Supposing there is a function f defined on the alphabet [0, 1], with output in the same alphabet, i.e. $f : [0, 1] \to [0, 1]$; there are then four possible scenarios:

- $f(0) = f(1) = 0$;
- $f(0) = f(1) = 1$;

- $f(0) = 0$ and $f(1) = 1$;
- $f(0) = 1$ and $f(1) = 0$.

The first two functions are called *constant* functions, whereas the last two are *balanced* functions. Given f, the Deutsch's algorithm [88] is able to tell if the function is constant or balanced without computing its output for both inputs. The first step of a quantum algorithm is usually the application of the Hadamard gate on every qubit to send them into a superposition of states. If the input is a superposition of n equally probable states, the function will be simultaneously computed for each state. This is not of help since the output is a superposition of states too, and all states have still the same outcome probability. However, quantum parallelism is still a very useful tool in quantum algorithm, since an appropriate manipulation of the complex probability amplitudes can, in some cases, increase the probability of the desired outcome exploiting the superposition of states. In the Deutsch's algorithm, this operation is the use of the oracle U_f, which corresponds the following gate, where $f(x)$ is the value of the function for the input x:

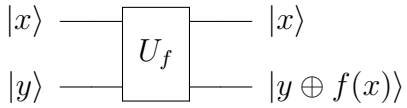

The full circuit that implements this algorithm is:

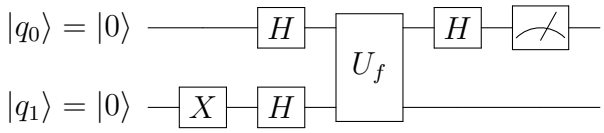

Note that U_f is only evaluated once in the algorithm, while classical algorithms would have called f twice to check both inputs. The output of the algorithm is measured on q_0, which is:

- $|0\rangle$ if f is constant;
- $|1\rangle$ if f is balanced.

The simulation has been run with a balanced f, i.e. $f(x) = x$, therefore the oracle is equivalent to a CNOT gate ($y \oplus f(x) = y \oplus x$) and the circuit is [89]:

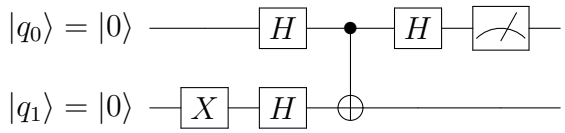

The algorithm is executed correctly since the most probable final state of q_0 is $|1\rangle$, as expected for the balanced f. For $t = 250$ ns (Figure 6.10), the D_{KL} is 0.0473 and the MATLAB/QuTiP error is minimal, but the results are quite degraded by decoherence since the algorithm is quite long. For $t = 14.2$ ns (Figure 6.11), the error is evidently larger, as $D_{KL} = 7.4771$ and an error of 30%, meaning that the off-resonance effects are very strong in this simulation.

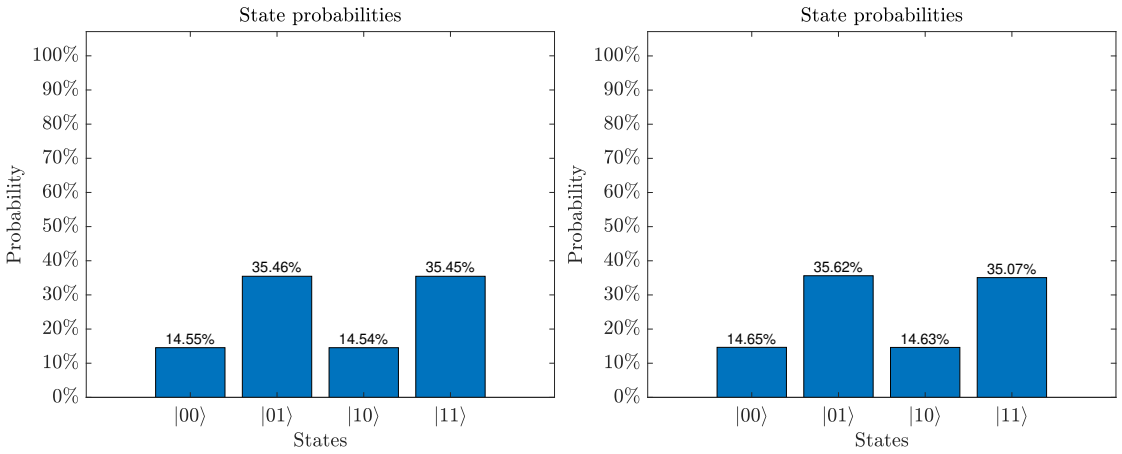

(a) MATLAB model results. (b) QuTiP results.

Figure 6.10: Probability comparison for the Deutsch's algorithm with balanced f for $t = 250$ ns.

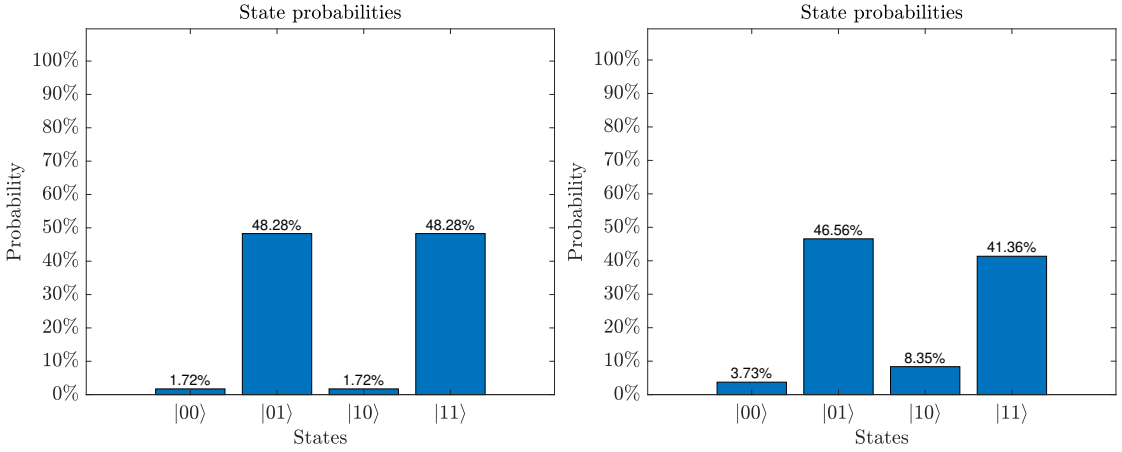

(a) MATLAB model results. (b) QuTiP results.

Figure 6.11: Probability comparison for the Deutsch's algorithm with balanced f for $t = 14.2$ ns.

Grover's algorithm

Suppose a large list of N unsorted items is given. Among all items there is one particular element that possess a special property: this is called the *winner* ω. Using classical computation, one would have to check on average $\frac{N}{2}$ items to find the winner (N items in the worst case). The Grover's search algorithm [90] takes roughly $\sqrt{N}$ steps. The first building block of the circuit is the set of Hadamard gates on each qubit to ensure superposition of states and combined evaluation. The quantum parallelism is exploited by the oracle U_ω, which adds a negative phase to the winner state:

$$U_\omega |x\rangle = \begin{cases} |x\rangle & \text{for} \quad |x\rangle \neq \omega \\ -|x\rangle & \text{for} \quad |x\rangle = \omega \end{cases} . \tag{6.10}$$

The oracle will be a diagonal matrix where only the term that corresponds to the winner state has a negative phase. For two qubits and $\omega = |11\rangle$, it will be

$$U_\omega = U_{CZ} = \begin{bmatrix} 1 & 0 & 0 & 0 \\ 0 & 1 & 0 & 0 \\ 0 & 0 & 1 & 0 \\ 0 & 0 & 0 & -1 \end{bmatrix} . \tag{6.11}$$

The amplitude amplification of the winner state ω is performed by the *diffuser* U_S [91]. The general Grover algorithm is then:

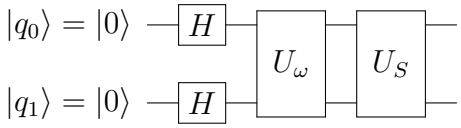

The output $|q_1 q_0\rangle$ is the winner state ω. The simulation has been run for $\omega = |11\rangle$, therefore the circuit is [92]:

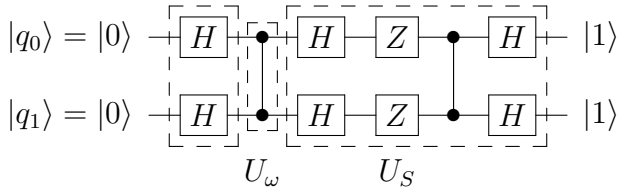

The most probable is indeed $|11\rangle$, despite the relaxation and decoherence effects are now clearly visible in the $t = 250$ ns simulation (Figure 6.12), since the algorithm performs more gates than the previous circuits and thus the device manipulation time is longer. However, the error between the two models is still very low, with a $D_{KL} = 0.0669$. On the other hand, the test with $t = 14.2$ ns carries out a better result in terms of $|11\rangle$ probability (Figure 6.13), since the non-ideal effects are weak. However, the discrepancy between the models is quite large, giving $D_{KL} = 1.2241$ and an error of 19.0532%.

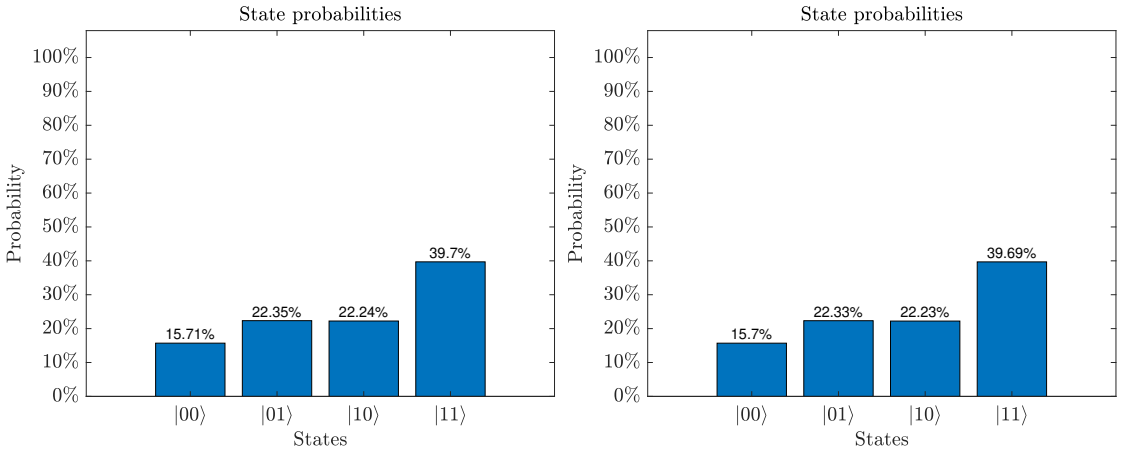

(a) MATLAB model results. (b) QuTiP results.

Figure 6.12: Probability comparison for the Grover's algorithm with $\omega = |11\rangle$ for $t = 250$ ns.

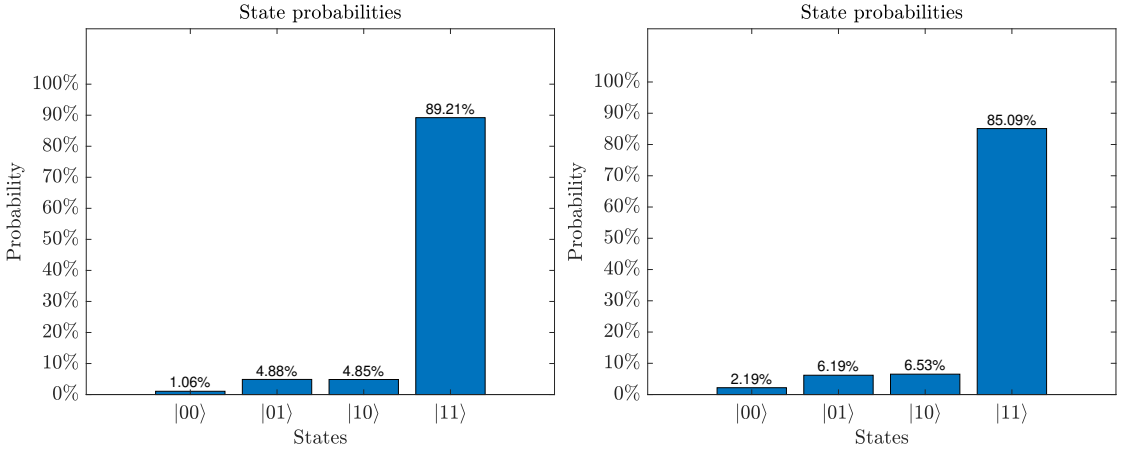

(a) MATLAB model results. (b) QuTiP results.

Figure 6.13: Probability comparison for the Grover's algorithm with $\omega = |11\rangle$ for $t = 14.2$ ns.

Chapter 7

Conclusions

The goal of this thesis was to realize a compact model able to simulate a semiconductor double quantum dot device, looking for a compromise between accuracy and computational complexity. The core of the work has been the construction of the compact model itself, starting from the characteristic Hamiltonian of the quantum system and using different types of approximations. The DQD device has been initially described by the six-state Hubbard model, whose basis has been reduced to the computational one through the Schrieffer-Wolff transformation. The resulting two-qubit spin Hamiltonian was observed to be similar to the NMR implementation up to a change of basis. For this reason, the model derivation has been shaped following the inheritance of the compatible NMR formalism. This also permitted to obtain a time-independent Hamiltonian of the system, which in turn allowed a simpler evaluation of the qubits dynamics. The results of the model have been compared to a reference simulator, QuTiP, capable of solving the Lindblad master equation, and the model approximations have been verified in different operating cases. Indeed, the two native gate regimes of a DQD device have been tested an the MATLAB/QuTiP error has been analyzed for two-qubit and single-qubit gates.
The model has proved to be well performing in the simulation where the native gate was the CPHASE, whereas the error was slightly but notably higher in the $\sqrt{\text{SWAP}}$ case. The main source of error in the simulations was the off-resonance effect when performing single-qubit gates. In fact, the RWA employed on the Hamiltonian to remove the time-dependent terms related to the non-target qubit was quite strong and worked properly only when the qubits resonance frequencies were sufficiently distant and the single-qubit gates were long enough. However, the state of the art hardwares tend to utilize the CPHASE gate more often than the $\sqrt{\text{SWAP}}$ one and the single-qubit gates are usually the longest type of gate in spin-qubit devices, therefore the model correctly works in the most common scenario.
Then, an efficient noise model developed in [15] to describe the relaxation and decoherence phenomena in spin qubit systems has been implemented in the MATLAB compact model. The noise algorithm proved to be correctly achieving its purpose

and its effect were evidently clear in the longer circuit simulations. On the other hand, for smaller gate times, the off-resonance effects became relevant and the the MATLAB/QuTiP error was notably degraded.
The most relevant advantage of the compact model has been its simulation time. Indeed, the QuTiP simulations were very long and computationally demanding, taking even hours for the most precise simulations (~ 1200 data points). Instead, the MATLAB model has always been very performing in this aspect, taking at most seconds for the same set of simulations. Therefore, from the simulation time point of view, the compact model has achieved its goal of outperforming a formal exact simulation, still producing reliable results.
Overall, the compact model approach has demonstrated to be capable of handling quite accurately a quantum circuit simulation. However, owing to the versatility of the compact model, there are different types of enhancement applicable. The most crucial one is the comparison with a real hardware: there are indeed some already available frameworks that permit to execute quantum circuits on existing semiconductor quantum computers, such as the Quantum Inspire by the QuTech group at TU Delft [38], through a cloud access. Testing the compact model through a physical device simulation is a very useful tool to evaluate the capabilities of the model and, in particular, to compare the modelled noise to the device real noise. This comparison would also permit to include in the compact model additional noise sources, such as the temperature and the interaction with the magnetic field. In this context, it is important to mention the modelling of the state readout operation, which is one of the most crucial and problematic parts of semiconductor quantum computers. Indeed, this operation is a fundamental piece of the device functioning, and directly influences the outcome of a real hardware, since it is always performed after the manipulation. The readout introduces a huge amount of noise and has to be performed in a very precise manner in order to yield a correct outcome. Hence, in order to compare the model to a real hardware, one has to take into account the readout operation and its strong non-ideality.
Another idea comes from the natural aim of a device simulation: being able to inspect the performance of the device when varying the technological steps used to realize it or its materials opens the possibility of device engineering. In order to perform this type of simulation, one has to implement a low-level model, which calculates the device physical parameters, such as g-factor, valley splitting — and, more in general, the system energy levels distribution — and nuclear noise, from the definition of the structure itself (i.e. the dimensions of the layers). This can be done through the help of low-level simulators, whose results can be used to see the behaviour — e.g. through a fitting — of the device relevant parameters for different structure realizations. These results can be then implemented in the compact model, which will take the structure technological parameters and perform an extra step to compute the required system parameters. The outcome of the model simulation will then be dependent on how the device has been practically realized,

allowing performance optimizations.
Furthermore, as of now, the model is only able to handle a double quantum dot structure and thus a maximum of two qubits. This matter can be solved from the model programming point of view, expanding the analysis to the case of n qubits by finding a general expression for the Hubbard model, able to describe n quantum dots and their interaction. This proves to be useful in the simulation of more complex structures involving more than two qubits and complex quantum circuits.
Since the model is based on the spin-$\frac{1}{2}$ encoding, it is straightforward that a future improvement might be the implementation of different encodings, such as the singlet-triplet, the exchange-only and the charge one. This would obviously require the study of their manipulation techniques, which usually depend on the encoding. Hence, the system theoretical analysis must be carried out again, but, since the spin-$\frac{1}{2}$ qubits incorporate the most relevant features of the spin quantum dots device, one could probably make use of the work performed in this thesis and adapt it to the case under study.
The route towards practically employable quantum computing must inevitably pass through quantum device engineering. Even if the prototype model developed in this thesis is still not able to allow a performance analysis based on low-level parameters, it might still be a starting point towards the enhancement of semiconductor quantum devices.

Bibliography

[1] Daniel Loss and David P. DiVincenzo. Quantum computation with quantum dots. *Phys. Rev. A*, 57:120–126, Jan 1998.

[2] NW Hendrickx, WIL Lawrie, L Petit, A Sammak, G Scappucci, and M Veldhorst. A single-hole spin qubit. *Nature communications*, 11(1):1–6, Jul 2020.

[3] Bruce E Kane. A silicon-based nuclear spin quantum computer. *Nature*, 393(6681):133–137, May 1998.

[4] Justin Weber, W Koehl, Joel Varley, Anderson Janotti, Bob Buckley, Chris Walle, and David Awschalom. Quantum computing with defects. *Proceedings of the National Academy of Sciences of the United States of America*, 107:8513–8, May 2010.

[5] Nico W Hendrickx, William IL Lawrie, Maximilian Russ, Floor van Riggelen, Sander L de Snoo, Raymond N Schouten, Amir Sammak, Giordano Scappucci, and Menno Veldhorst. A four-qubit germanium quantum processor. *Nature*, 591(7851):580–585, Mar 2021.

[6] Shannon Pasca Harvey. *Developing Singlet-Triplet Qubits in Gallium Arsenide as a Platform for Quantum Computing*. PhD thesis, Harvard University, 2019.

[7] JR Weber, WF Koehl, JB Varley, A Janotti, BB Buckley, CG Van de Walle, and DD Awschalom. Defects in SiC for quantum computing. *Journal of Applied Physics*, 109(10):102417, May 2011.

[8] Guido Burkard, Thaddeus D Ladd, John M Nichol, Andrew Pan, and Jason R Petta. Semiconductor spin qubits. *arXiv preprint arXiv:2112.08863*, 2021.

[9] M Veldhorst, HGJ Eenink, Chih-Hwan Yang, and Andrew S Dzurak. Silicon CMOS architecture for a spin-based quantum computer. *Nature communications*, 8(1):1–8, 2017.

[10] Erika Kawakami, Thibaut Jullien, Pasquale Scarlino, Daniel R Ward, Donald E Savage, Max G Lagally, Viatcheslav V Dobrovitski, Mark Friesen, Susan N Coppersmith, Mark A Eriksson, et al. Gate fidelity and coherence of an electron

spin in an Si/SiGe quantum dot with micromagnet. *Proceedings of the National Academy of Sciences*, 113(42):11738–11743, 2016.

[11] Luca Petit, HGJ Eenink, M Russ, WIL Lawrie, NW Hendrickx, SGJ Philips, JS Clarke, LMK Vandersypen, and M Veldhorst. Universal quantum logic in hot silicon qubits. *Nature*, 580(7803):355–359, 2020.

[12] Anasua Chatterjee, Paul Stevenson, Silvano De Franceschi, Andrea Morello, Nathalie P de Leon, and Ferdinand Kuemmeth. Semiconductor qubits in practice. *Nature Reviews Physics*, 3(3):157–177, 2021.

[13] Jan Fischer, Mircea Trif, WA Coish, and Daniel Loss. Spin interactions, relaxation and decoherence in quantum dots. *Solid state communications*, 149(35-36):1443–1450, 2009.

[14] Daniel Manzano. A short introduction to the Lindblad master equation. *Aip Advances*, 10(2):025106, 2020.

[15] Mario Simoni, Giovanni Amedeo Cirillo, Giovanna Turvani, Mariagrazia Graziano, and Maurizio Zamboni. Towards compact modeling of noisy quantum computers: A molecular-spin-qubit case of study. *ACM Journal on Emerging Technologies in Computing Systems (JETC)*, 18(1):1–26, 2021.

[16] Michael A. Nielsen and Isaac L. Chuang. *Quantum Computation and Quantum Information: 10th Anniversary Edition*. Cambridge University Press, 2010.

[17] Giovanni Ghione. *Semiconductor devices for high-speed optoelectronics*, volume 116. Cambridge University Press Cambridge, 2009.

[18] Prasanta Misra. *Physics of condensed matter*. Academic Press, 2011.

[19] Floris A. Zwanenburg, Andrew S. Dzurak, Andrea Morello, Michelle Y. Simmons, Lloyd C. L. Hollenberg, Gerhard Klimeck, Sven Rogge, Susan N. Coppersmith, and Mark A. Eriksson. Silicon quantum electronics. *Rev. Mod. Phys.*, 85:961–1019, Jul 2013.

[20] Marius Grundmann. *Physics of semiconductors*, volume 11. Springer, 2010.

[21] Haiyan Zheng, Yongjun Li, Huibiao Liu, Xiaodong Yin, and Yuliang Li. Construction of heterostructure materials toward functionality. *Chem. Soc. Rev.*, 40:4506–4524, May 2011.

[22] Paul Harrison and Alex Valavanis. *Quantum wells, wires and dots: theoretical and computational physics of semiconductor nanostructures*. John Wiley & Sons, 2016.

[23] Eric G Barbagiovanni, David J Lockwood, Peter J Simpson, and Lyudmila V Goncharova. Quantum confinement in Si and Ge nanostructures: Theory and experiment. *Applied Physics Reviews*, 1(1):011302, Jan 2014.

[24] Dieter Bimberg, Marius Grundmann, and Nikolai N Ledentsov. *Quantum dot heterostructures*. John Wiley & Sons, 1999.

[25] John King Gamble, Patrick Harvey-Collard, N Tobias Jacobson, Andrew D Baczewski, Erik Nielsen, Leon Maurer, Inès Montaño, Martin Rudolph, MS Carroll, CH Yang, et al. Valley splitting of single-electron Si MOS quantum dots. *Applied Physics Letters*, 109(25):253101, Oct 2016.

[26] CH Yang, A Rossi, R Ruskov, NS Lai, FA Mohiyaddin, S Lee, C Tahan, Gerhard Klimeck, A Morello, and AS Dzurak. Spin-valley lifetimes in a silicon quantum dot with tunable valley splitting. *Nature communications*, 4(1):1–8, Jun 2013.

[27] Xin Zhang, Rui-Zi Hu, Hai-Ou Li, Fang-Ming Jing, Yuan Zhou, Rong-Long Ma, Ming Ni, Gang Luo, Gang Cao, Gui-Lei Wang, et al. Giant anisotropy of spin relaxation and spin-valley mixing in a silicon quantum dot. *Physical Review Letters*, 124(25):257701, Jun 2020.

[28] Matthew G Borselli, Richard S Ross, Andrey A Kiselev, Edward T Croke, Kevin S Holabird, Peter W Deelman, Leslie D Warren, Ivan Alvarado-Rodriguez, Ivan Milosavljevic, Fiona C Ku, et al. Measurement of valley splitting in high-symmetry Si/SiGe quantum dots. *Applied Physics Letters*, 98(12):123118, Mar 2011.

[29] Mark Friesen, Sucismita Chutia, Charles Tahan, and SN Coppersmith. Valley splitting theory of Si Ge/Si/SiGe quantum wells. *Physical Review B*, 75(11):115318, Mar 2007.

[30] JR Prance, Zhan Shi, CB Simmons, DE Savage, MG Lagally, LR Schreiber, LMK Vandersypen, Mark Friesen, Robert Joynt, SN Coppersmith, et al. Single-shot measurement of triplet-singlet relaxation in a Si/SiGe double quantum dot. *Physical review letters*, 108(4):046808, Jan 2012.

[31] Arne Hollmann, Tom Struck, Veit Langrock, Andreas Schmidbauer, Floyd Schauer, Tim Leonhardt, Kentarou Sawano, Helge Riemann, Nikolay V Abrosimov, Dominique Bougeard, et al. Large, tunable valley splitting and single-spin relaxation mechanisms in a Si/Si_xGe_{1-x} quantum dot. *Physical review applied*, 13(3):034068, Mar 2020.

[32] HL Störmer, R Dingle, AC Gossard, W Wiegmann, and MD Sturge. Two-dimensional electron gas at a semiconductor-semiconductor interface. *Solid state communications*, 29(10):705–709, Mar 1979.

[33] Lieven MK Vandersypen and Mark A Eriksson. Quantum computing with semiconductor spins. *Physics Today*, 72:8–38, 2019.

[34] Wee Han Lim Andre Saraiva, Arne Laucht Chih Hwan Yang, Christopher C. Escott, and Andrew S. Dzurak. Materials for silicon quantum dots and their impact on electron spin qubits. *Advanced Functional Materials*, page 2105488, Jul 2021.

[35] Marc A Kastner. The single-electron transistor. *Reviews of modern physics*, 64(3):849, Jul 1992.

[36] JM Elzerman, R Hanson, JS Greidanus, LH Willems Van Beveren, S De Franceschi, LMK Vandersypen, S Tarucha, and LP Kouwenhoven. Few-electron quantum dot circuit with integrated charge read out. *Physical Review B*, 67(16):161308, Apr 2003.

[37] Leo P Kouwenhoven, Charles M Marcus, Paul L McEuen, Seigo Tarucha, Robert M Westervelt, and Ned S Wingreen. Electron transport in quantum dots. In *Mesoscopic electron transport*, pages 105–214. Springer, 1997.

[38] Thorsten Last, Nodar Samkharadze, Pieter Eendebak, Richard Versluis, Xiao Xue, Amir Sammak, Delphine Brousse, Kelvin Loh, Henk Polinder, Giordano Scappucci, et al. Quantum inspire: QuTech's platform for co-development and collaboration in quantum computing. In *Novel patterning technologies for semiconductors, MEMS/NEMS and MOEMS 2020*, volume 11324, page 113240J. International Society for Optics and Photonics, Mar 2020.

[39] HGJ Eenink. *Hot qubits in silicon for quantum computation*. PhD thesis, Delft University of Technology, 2021.

[40] E. B. Al, E. Kasapoglu, H. Sari, and I. Sökmen. Zeeman splitting, Zeeman transitions and optical absorption of an electron confined in spherical quantum dots under the magnetic field. *Philosophical Magazine*, 101(1):117–128, 2021.

[41] Mohammad Mostafanejad. Basics of the spin hamiltonian formalism. *International Journal of Quantum Chemistry*, 114(22):1495–1512, 2014.

[42] Xin Zhang, Hai-Ou Li, Gang Cao, Ming Xiao, Guang-Can Guo, and Guo-Ping Guo. Semiconductor quantum computation. *National Science Review*, 6(1):32–54, 12 2018.

[43] Jun Yoneda, Kenta Takeda, Tomohiro Otsuka, Takashi Nakajima, Matthieu R Delbecq, Giles Allison, Takumu Honda, Tetsuo Kodera, Shunri Oda, Yusuke Hoshi, et al. A quantum-dot spin qubit with coherence limited by charge noise and fidelity higher than 99.9%. *Nature nanotechnology*, 13(2):102–106, 2018.

[44] Gang Cao, Hai-Ou Li, Tao Tu, Li Wang, Cheng Zhou, Ming Xiao, Guang-Can Guo, Hong-Wen Jiang, and Guo-Ping Guo. Ultrafast universal quantum control of a quantum-dot charge qubit using landau–zener–stückelberg interference. *Nature Communications*, 4(1):1–7, 2013.

[45] Zhan Shi, CB Simmons, JR Prance, John King Gamble, Teck Seng Koh, Yun-Pil Shim, Xuedong Hu, DE Savage, MG Lagally, MA Eriksson, et al. Fast hybrid silicon double-quantum-dot qubit. *Physical review letters*, 108(14):140503, 2012.

[46] Teck Seng Koh, John King Gamble, Mark Friesen, MA Eriksson, and SN Coppersmith. Pulse-gated quantum-dot hybrid qubit. *Physical review letters*, 109(25):250503, 2012.

[47] Dohun Kim, Zhan Shi, CB Simmons, DR Ward, JR Prance, Teck Seng Koh, John King Gamble, DE Savage, MG Lagally, Mark Friesen, et al. Quantum control and process tomography of a semiconductor quantum dot hybrid qubit. *Nature*, 511(7507):70–74, 2014.

[48] Hugh Burrows, Maria Azenha, and Carlos Monteiro. *Catalysis from Theory to Application. An Integrated Course.* 05 2008.

[49] Rusko Ruskov, Menno Veldhorst, Andrew S Dzurak, and Charles Tahan. Electron g-factor of valley states in realistic silicon quantum dots. *Physical Review B*, 98(24):245424, 2018.

[50] R Neumann and LR Schreiber. Simulation of micro-magnet stray-field dynamics for spin qubit manipulation. *Journal of Applied Physics*, 117(19):193903, 2015.

[51] HW Liu, T Fujisawa, Y Ono, H Inokawa, A Fujiwara, Kei Takashina, and Y Hirayama. Pauli-spin-blockade transport through a silicon double quantum dot. *Physical Review B*, 77(7):073310, 2008.

[52] C Ellenberger, T Ihn, C Yannouleas, U Landman, K Ensslin, D Driscoll, and AC Gossard. Excitation spectrum of two correlated electrons in a lateral quantum dot with negligible Zeeman splitting. *Physical review letters*, 96(12):126806, 2006.

[53] Clement H Wong, MA Eriksson, SN Coppersmith, and Mark Friesen. High-fidelity singlet-triplet s- t- qubits in inhomogeneous magnetic fields. *Physical Review B*, 92(4):045403, 2015.

[54] Xian Wu, Daniel R Ward, JR Prance, Dohun Kim, John King Gamble, RT Mohr, Zhan Shi, DE Savage, MG Lagally, Mark Friesen, et al. Two-axis control of a singlet–triplet qubit with an integrated micromagnet. *Proceedings of the National Academy of Sciences*, 111(33):11938–11942, 2014.

[55] Filip K Malinowski, Frederico Martins, Peter D Nissen, Edwin Barnes, Łukasz Cywiński, Mark S Rudner, Saeed Fallahi, Geoffrey C Gardner, Michael J Manfra, Charles M Marcus, et al. Notch filtering the nuclear environment of a spin qubit. *Nature nanotechnology*, 12(1):16–20, 2017.

[56] JM Elzerman, R Hanson, LH Willems van Beveren, B Witkamp, LMK Vandersypen, and Leo P Kouwenhoven. Single-shot read-out of an individual electron spin in a quantum dot. *nature*, 430(6998):431–435, 2004.

[57] D Kotekar-Patil, A Corna, R Maurand, A Crippa, A Orlov, S Barraud, L Hutin, M Vinet, X Jehl, S De Franceschi, et al. Pauli spin blockade in CMOS double quantum dot devices. *physica status solidi (b)*, 254(3):1600581, 2017.

[58] Andrea Corna, Léo Bourdet, Romain Maurand, Alessandro Crippa, Dharmraj Kotekar-Patil, Heorhii Bohuslavskyi, Romain Laviéville, Louis Hutin, Sylvain Barraud, Xavier Jehl, et al. Electrically driven electron spin resonance mediated by spin–valley–orbit coupling in a silicon quantum dot. *npj quantum information*, 4(1):1–7, 2018.

[59] Emmanuel I Rashba. Theory of electric dipole spin resonance in quantum dots: Mean field theory with gaussian fluctuations and beyond. *Physical Review B*, 78(19):195302, 2008.

[60] Guido Burkard, Daniel Loss, and David P DiVincenzo. Coupled quantum dots as quantum gates. *Physical Review B*, 59(3):2070, 1999.

[61] HGJ Eenink, L Petit, WIL Lawrie, JS Clarke, LMK Vandersypen, and M Veldhorst. Tunable coupling and isolation of single electrons in silicon metal-oxide-semiconductor quantum dots. *Nano letters*, 19(12):8653–8657, 2019.

[62] Claude Cohen-Tannoudji, Bernard Diu, and Frank Laloe. Quantum mechanics, volume 1. *Quantum Mechanics*, 1:898, 1986.

[63] JM Brown, RJ Buenker, A Carrington, C Di Lauro, RN Dixon, RW Field, JT Hougen, W Hüttner, K Kuchitsu, M Mehring, et al. Remarks on the signs of g factors in atomic and molecular Zeeman spectroscopy, 2000.

[64] MJ Snelling, GP Flinn, AS Plaut, RT Harley, AC Tropper, R Eccleston, and CC Phillips. Magnetic g factor of electrons in GaAs/$Al_xGa_{1-x}As$ quantum wells. *Physical Review B*, 44(20):11345, 1991.

[65] Ali Ahmed and Mustafa Ahmed. *Dynamical decoupling using NMR for quantum computing*. PhD thesis, 2013.

[66] Clèment Godfrin. *Quantum information processing using a molecular magnet single nuclear spin qudit*. PhD thesis, Université Grenoble Alpes (ComUE), 2017.

[67] Hendrik Bluhm, Thomas Brückel, Markus Morgenstern, Gero Plessen, and Christoph Stampfer. *Electrons in solids*. de Gruyter, 2019.

[68] Bruce Shore. The theory of coherent atomic excitation, 1991.

[69] Ivan Oliveira, Roberto Sarthour Jr, Tito Bonagamba, Eduardo Azevedo, and Jair CC Freitas. *NMR quantum information processing*. Elsevier, 2011.

[70] Mikio Nakahara and Tetsuo Ohmi. *Quantum Computing From Linear Algebra to Physical Realizations*. CRC Press, 1 edition, 2008.

[71] David C McKay, Christopher J Wood, Sarah Sheldon, Jerry M Chow, and Jay M Gambetta. Efficient Z gates for quantum computing. *Physical Review A*, 96(2):022330, 2017.

[72] Giovanni Amedeo Cirillo, Giovanna Turvani, Mario Simoni, and Mariagrazia Graziano. Advances in molecular quantum computing: From technological modeling to circuit design. In *2020 IEEE Computer Society Annual Symposium on VLSI (ISVLSI)*, pages 132–137. IEEE, 2020.

[73] J Robert Johansson, Paul D Nation, and Franco Nori. QuTiP: An open-source Python framework for the dynamics of open quantum systems. *Computer Physics Communications*, 183(8):1760–1772, 2012.

[74] Andrew W Cross, Lev S Bishop, John A Smolin, and Jay M Gambetta. Open quantum assembly language. *arXiv preprint arXiv:1707.03429*, 2017.

[75] Menno Veldhorst, CH Yang, JCC Hwang, W Huang, JP Dehollain, JT Muhonen, S Simmons, A Laucht, FE Hudson, Kohei M Itoh, et al. A two-qubit logic gate in silicon. *Nature*, 526(7573):410–414, 2015.

[76] Tristan Meunier, VE Calado, and LMK Vandersypen. Efficient controlled-phase gate for single-spin qubits in quantum dots. *Physical Review B*, 83(12):121403, 2011.

[77] Maximilian Russ, David M Zajac, Anthony J Sigillito, Felix Borjans, Jacob M Taylor, Jason R Petta, and Guido Burkard. High-fidelity quantum gates in Si/SiGe double quantum dots. *Physical Review B*, 97(8):085421, 2018.

[78] Utkan Güngördü and JP Kestner. Pulse sequence designed for robust c-phase gates in simos and Si/SiGe double quantum dots. *Physical Review B*, 98(16):165301, 2018.

[79] Ahmad Jamalzada. *Simulating dynamics of two electron spins in a Si-based double quantum dot*. PhD thesis, Leiden University, 2019.

[80] TF Watson, SGJ Philips, Erika Kawakami, DR Ward, Pasquale Scarlino, Menno Veldhorst, DE Savage, MG Lagally, Mark Friesen, SN Coppersmith, et al. A programmable two-qubit quantum processor in silicon. *Nature*, 555(7698):633–637, 2018.

[81] Seung-Sup B Lee, Jan von Delft, and Andreas Weichselbaum. Generalized schrieffer-wolff transformation of multiflavor hubbard models. *Physical Review B*, 96(24):245106, 2017.

[82] Chia-Hsien Huang, Chih-Hwan Yang, Chien-Chang Chen, Andrew S Dzurak, and Hsi-Sheng Goan. High-fidelity and robust two-qubit gates for quantum-dot spin qubits in silicon. *Physical Review A*, 99(4):042310, 2019.

[83] Carola Meyer. Quantum computing with semiconductor quantum dots. 2009.

[84] L Petit, M Russ, HGJ Eenink, WIL Lawrie, JS Clarke, LMK Vandersypen, and M Veldhorst. High-fidelity two-qubit gates in silicon above one Kelvin. *arXiv preprint arXiv:2007.09034*, 2020.

[85] Solomon Kullback and Richard A Leibler. On information and sufficiency. *The annals of mathematical statistics*, 22(1):79–86, 1951.

[86] Shin Nishio, Yulu Pan, Takahiko Satoh, Hideharu Amano, and Rodney Van Meter. Extracting success from IBM's 20-qubit machines using error-aware compilation. *ACM Journal on Emerging Technologies in Computing Systems (JETC)*, 16(3):1–25, 2020.

[87] S Balakrishnan. Various constructions of qudit SWAP gate. *Physics Research International*, 2014, 2014.

[88] David Collins, KW Kim, and WC Holton. Deutsch-Jozsa algorithm as a test of quantum computation. *Physical Review A*, 58(3):R1633, 1998.

[89] Abraham Asfaw, Luciano Bello, Yael Ben-Haim, Sergey Bravyi, Lauren Capelluto, Almudena Carrera Vazquez, Jack Ceroni, Jay Gambetta, Shelly Garion, Leron Gil, et al. Learn quantum computation using qiskit. *URL: https://qiskit.org/textbook/ch-algorithms/deutsch-jozsa.html*, 2020.

[90] Lov K Grover. A fast quantum mechanical algorithm for database search. In *Proceedings of the twenty-eighth annual ACM symposium on Theory of computing*, pages 212–219, 1996.

[91] Bikram Khanal, Pablo Rivas, and J Orduz. Quantum machine learning: A case study of Grover's algorithm. In *Proceedings of the 19th International Conference on Scientific Computing (CSC 2021), Las Vegas, NV, USA*, pages 15–17, 2021.

[92] Abraham Asfaw, Luciano Bello, Yael Ben-Haim, Sergey Bravyi, Lauren Capelluto, Almudena Carrera Vazquez, Jack Ceroni, Jay Gambetta, Shelly Garion, Leron Gil, et al. Learn quantum computation using qiskit. *URL: https://qiskit.org/textbook/ch-algorithms/grover.html*, 2020.